Non-Contrast Perfusion Ultrasound Imaging for Evaluating Transarterial Chemoembolization

By

Jaime Tierney

Dissertation

Submitted to the Faculty of the

Graduate School of Vanderbilt University

in partial fulfillment of the requirements

for the degree of

DOCTOR OF PHILOSOPHY

in

Biomedical Engineering

August 9, 2019

Nashville, Tennessee

Approved:

Brett C. Byram, Ph.D.

Daniel B. Brown, M.D.

Charles F. Caskey, Ph.D.

Michael I. Miga, Ph.D.

Don M. Wilkes, Ph.D.

To my husband, Matt, and to my parents, Mike and Johnna. Thank you for your unconditional support and encouragement.

ACKNOWLEDGMENTS

I would like to thank Dr. Byram for believing in me and providing me with the resources I needed to complete this dissertation. I am extremely grateful and lucky to have had his support and guidance throughout this process.

I would like to thank the other members of my committee: Dr. Brown, Dr. Caskey, Dr. Miga, and Dr. Wilkes. This work would not have been possible without their insight and willingness to collaborate.

I thank the members of the BEAM lab for their help, advice, and camaraderie. A special thanks to Kristy Walsh and Kazuyuki Dei who have been there for me since day one.

I would also like to thank and acknowledge the staff of the Vanderbilt University ACCRE computing resource and our funding sources: NIH grants 1R35HL135790-01 and S10OD016216-01 and NSF award IIS-1750994.

TABLE OF CONTENTS

LIST OF TABLES

LIST OF FIGURES

Chapter 1

Background and Significance

1.1 Fundamentals of Ultrasound Imaging

Ultrasound is widely used clinically for characterizing soft tissue structures and measuring blood flow in the human body. Compared to other modalities, ultrasound is noninvasive, affordable, portable, and can provide real-time 2D or 3D cross-sectional information. This section will cover the fundamental principles of conventional anatomical brightness-mode (B-mode) imaging and Doppler ultrasound blood flow imaging.

1.1.1 Conventional B-mode

Ultrasound imaging generally works by transmitting a high frequency sound wave generated by a piezoelectric transducer into a medium [1, 2]. The same transducer then receives the subsequent backscattered echoes that return from interaction of the sound wave with structures within the medium [1, 2].

Transducers typically have multiple elements through which signals are transmitted and received [1, 2]. Focusing of the transmitted and received waves is achieved by applying time delays to each element's signal [2]. For conventional ultrasound imaging, a single radio frequency (RF) amplitude-line (A-line) of the image is acquired at a time by focusing the transmitted wave at a single lateral location and depth [2]. For each A-line, echo signals are received by each element or channel. These receive channel signals are delayed and then summed to generate a single RF line, which is shown as the blue line in Figure 1.1a. The envelope of the RF line is the A-line, which is shown as the red line in Figure 1.1a. Subsequent A-lines are acquired by sweeping the lateral transmit focus across the field of view. Concatenation of each A-line produces an amplitude image that has an axial (fast-

time or depth) and lateral dimension, as shown in Figure 1.1b. The RF amplitude image will have a large dynamic range, making it difficult to differentiate structures [1]. This image is therefore compressed to generate a B-mode image, as shown in Figure 1.1c.

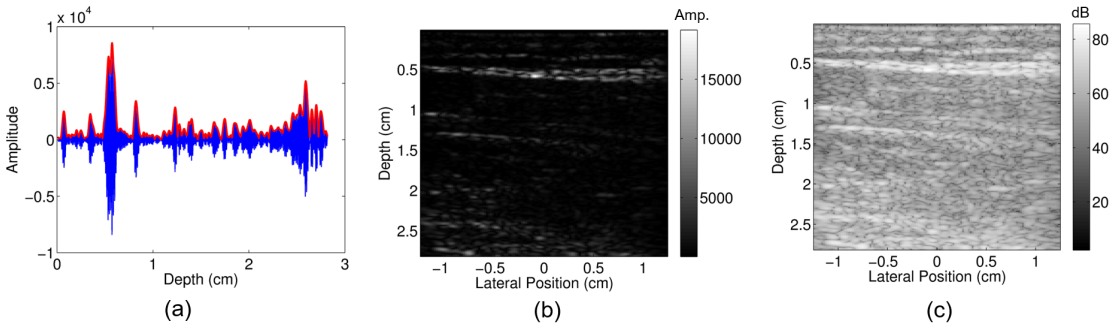

Figure 1.1: (a) Example RF line (blue) and corresponding A-line (red). (b) Example RF amplitude image. (c) Example B-mode image.

The overall process of focusing using time delays and summation is called beamforming. A very generic method for beamforming is described here, but there are several variations that will become relevant later in this dissertation.

1.1.2 Doppler Ultrasound Theory

Conventional Doppler sequencing shares the same fundamentals as conventional A-line and B-mode imaging. The difference is that Doppler imaging involves the acquisition of multiple A-lines at a single lateral location, resulting in a third dimension that will be referred to as slow-time. A-lines concatenated through slow-time are called a motion-mode (M-mode) image. An example M-mode image is shown in Figure 1.2. When only flowing blood is in the field of view, motion detected in received signals in the slow-time dimension will be related to the velocity of the flowing blood. This relationship is partly understood by the effect by which the name Doppler ultrasound originates from.

The well-known Doppler effect, discovered by Christian Doppler, an Austrian physicist, in 1842, describes the phenomenon of an observed frequency seemingly changing with respect to a moving source [3]. In reality, the transmitted frequency from the source is

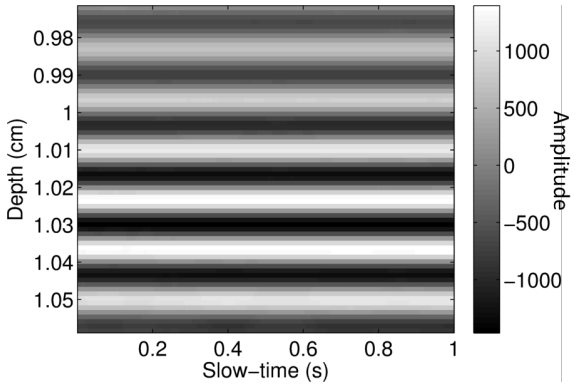

Figure 1.2: Example M-mode image.

not changing, but as the source moves towards or away from an observer, the observed or received frequency seems to increase or decrease, respectively. The difference between the transmitted and received frequencies is known as the Doppler frequency, or shift, and is related to the speed of the transmitted wave and the difference in velocity of the source and observer, as described in Equation 1.1,

$$f_d = f_r - f_0 = -\frac{v_{0r}}{c} f_0 \tag{1.1}$$

where f_d is the Doppler frequency or shift, f_r is the received or observed frequency, f_0 is the transmitted frequency, v_{0r} is the difference between the velocity of the transmitter and receiver, and c is the speed of the transmitted wave [3]. Relating this to measuring blood velocity with ultrasound, f_0 would be the transmitted ultrasound frequency, f_r would be the received frequency from moving blood scatterers, v_{0r} would be the negative axial velocity of the blood scatterers if the transducer is stationary, and c would be the speed of sound.

Measuring the true Doppler effect with ultrasound equates to measuring a difference in pulse time duration between the transmitted and received signals [1]. This difference caused by the Doppler shift is small and difficult to detect with pulsed systems due to depth-dependent attenuation and noise, which can cause shifts larger than that caused by the Doppler effect [1]. Therefore, instead of measuring differences in pulse time durations between transmitted and received signals, most Doppler ultrasound techniques measure

differences in receive time delays between received signals from several transmitted pulse emissions [1]. Regardless, the relationship between Doppler frequency and velocity with these techniques equates to a similar relationship to that shown in Equation 1.1,

$$f_d = f_{r1} - f_{r2} = \frac{2v_z}{c} f_0 \tag{1.2}$$

where f_{r1} and f_{r2} are received ultrasound frequencies from two different pulse emissions, v_z is the axial velocity of the scatterers, and c is the speed of sound [1]. A factor of 2 is included here to account for the time it takes to travel away from the transducer and back between received signals. Assuming only blood scatterers are moving in the field of view of the ultrasound beam, v_z is equal to the axial velocity of the blood. Equqation 1.2 can be rewritten to include the true velocity of blood, v_b, as follows,

$$f_d = f_{r1} - f_{r2} = \frac{2|v_b|cos(\theta)}{c} f_0 \tag{1.3}$$

where θ is the beam-to-flow angle. A simple diagram of the transducer and blood flow coordinate system is shown in Figure 1.3.

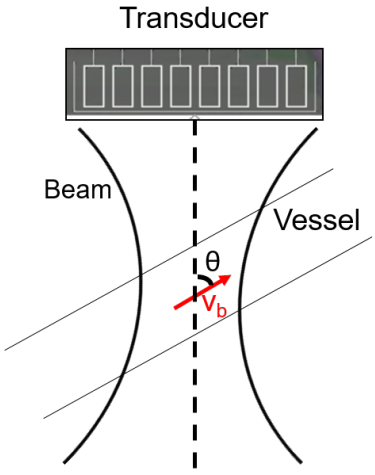

Figure 1.3: Diagram of blood velocity detection coordinate system with ultrasound.

1.1.3 Overview of Velocity Estimation Techniques

Doppler ultrasound comprises several different blood velocity estimation techniques, including continuous and pulsed wave (CW and PW), color, and power Doppler systems. All of these systems work by estimating the Doppler frequency and using it to compute velocity using the relationship described in Equation 1.3. They differ in dimensionality and intended application.

CW and PW systems provide one dimensional velocity estimates along a single line or at a single lateral and axial location, respectively [1]. CW systems compute the so called true Doppler frequency as the difference between continuously transmitted and received frequencies along a single line while PW systems compute the Doppler frequency as the time shift between received frequencies at a single depth or small window of depths [1]. Both CW and PW systems work well for measuring higher velocity blood flow at specific locations and have been shown to be useful for cardiac applications [1, 4].

Color Doppler systems overcome the limited field of view in CW and PW systems by providing 2-dimensional velocity and directional information [1]. Color Doppler systems use similar technology as PW systems to measure changes in received signals except at multiple axial and lateral locations to provide average velocity measurements at each pixel. Specifically, these systems use phase or time shift estimation techniques to measure axial displacements between consecutive received slow-time signals and corresponding axial velocities [1, 5, 6, 7]. Because these systems measure axial velocity, they are best at measuring high velocity blood flowing towards or away from the transducer or at small angles relative to the beam. They also are able to show directional information in the form of different colors. However, this causes color Doppler systems to be limited by direction and speed of flow.

Power Doppler is a more recent addition to the suite of velocity estimation techniques and overcomes directional limitations by computing the energy of signals through slow-time [1, 8, 9]. Doppler frequencies and corresponding velocities are observed by looking

at the power spectra through slow-time at a given pixel. However, the technique does not measure velocities from received signals like the CW, PW, or color Doppler systems. Instead it computes the amount of blood within a given pixel by taking the sum of squared values through slow-time, as shown in Equation 1.4,

$$P = \sum_{t=1}^{N} s(t)^2 \tag{1.4}$$

where N is the number of slow-time points and $s(t)$ is the signal amplitude at time t [10]. Because this technique reflects amount or volume of blood, it is particularly useful when imaging slower flow at larger angles relative to the beam [1, 10, 11, 12]. Power Doppler imaging is therefore the focus of this dissertation which aims to measure perfusion, or the slowest flow in the smallest vessels.

1.2 Tissue Clutter Filtering for Doppler Ultrasound

The above techniques rely on the changes in received signals to reflect changes in blood flow. However, for in vivo applications, the signal from tissue has been variably reported in the literature as being as low as 10-100 times and up to 100dB larger than the signal from blood [1, 13, 14, 15, 16, 17]. Therefore, for any of the above techniques to work, the signal from tissue must be filtered prior to estimating blood velocity or power.

Apart from the tissue signal being stronger than the blood signal, tissue is also assumed to be stationary or moving at lower frequencies or velocities than most blood flow. Therefore, high pass filters are used to attenuate tissue signal, as depicted in Figure 1.4. Conventional high pass filters have been investigated extensively for the purpose of suppressing tissue clutter in Doppler ultrasound imaging [18, 19, 20, 21, 13, 15]. Among the most commonly used are infinite and finite impulse response (IIR and FIR) filters and polynomial regression filters [13, 15, 16]. Each of these can be optimized in terms of frequency response parameters by choosing appropriate filter orders and frequency cutoffs [13]. Ad-

ditionally, instead of choosing a single cutoff for an entire image, adaptive selection of frequency cutoffs through depth has been proposed as a way to improve velocity detection [15, 22]. In order to achieve optimal tissue clutter filtering, sufficient slow-time sampling is needed, which causes a trade-off to be made between optimal filtering and frame rate for conventional Doppler sequencing [13].

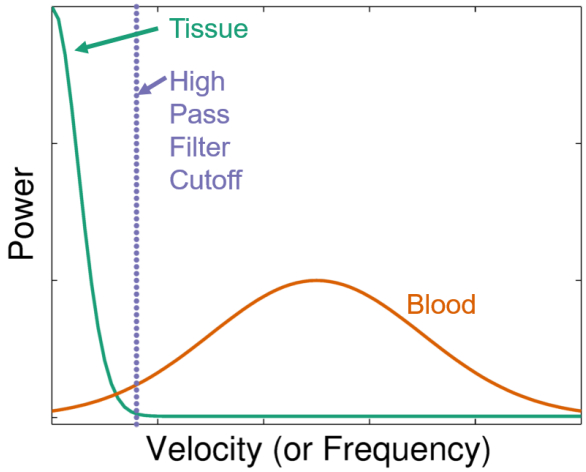

Figure 1.4: Schematic of ultrasound signal components and tissue clutter filtering.

1.3 Transarterial Chemoembolization (TACE)

There are several clinical applications for which non-contrast ultrasound perfusion imaging would be beneficial. Contrast agents are limited by time and dose in the blood stream and can make procedures more expensive and invasive. Additionally, contrast agents can cause misleading artifacts for certain applications. Evaluation of transarterial chemoembolization (TACE) treatment of liver tumors is one application for which non-contrast perfusion ultrasound imaging would be invaluable. Because of the severity of liver cancer, effective and timely evaluation of treatments like TACE are crucial for improving patient outcomes.

Liver cancer remains the 5th and 9th leading cause of cancer-related deaths globally among men and women, respectively [23]. Most affected patients ($>$70%) are not eligible for curative surgical treatment due to the severity of the disease upon diagnosis [24]. TACE

is a palliative treatment option for hepatic malignancies that do not qualify for curative transplant or resection [24, 25, 26, 27]. TACE is also used as a down-staging or bridging tool to qualify or maintain qualification for curative treatment, respectively [24, 27]. The minimally invasive procedure simultaneously delivers high doses of chemotherapy and embolizing agents to the blood supply of a tumor to provide targeted treatment and occlude the arterial supply [24, 25, 26]. TACE is variably effective, with reported response rates between 62-76% [28, 29]. Low response rates can be in part due to a lack of real-time assessment of treatment adequacy. Intra-procedural monitoring could identify the need for additional embolization during TACE and limit the number of repeat treatments.

Contrast-enhanced computed tomography (CE-CT) and magnetic resonance imaging (CE-MRI) are currently used to evaluate TACE treatment response [30, 27]. Both modalities depict contrast agents in the blood stream as hyper-enhancement [30]. Therefore, because TACE intends to substantially reduce tumor blood perfusion, complete response is indicated by absence of enhancement in the tumor, and residual tumor manifests as hyper-enhancement in follow-up images. Both are effective evaluation tools, but follow-up imaging is not performed until at least 4-6 weeks after treatment to allow time for treatment-related imaging artifacts to subside [30, 27]. These artifacts include hyper-enhancement in CE-CT and CE-MRI due to treatment-induced inflammation [31, 32]. Also, one of the substances typically used for delivering chemotherapy in conventional TACE, lipiodol, mimics hyper-enhancement in CE-CT [31, 27]. Contrast-enhanced ultrasound (CE-US) has been proposed as a solution for earlier treatment evaluation (during or 1-2 weeks post-treatment) because it is less affected by these artifacts in addition to being more affordable and accessible [33, 32, 27]. However, trapped air bubbles and drug-eluting beads (DEB) used in DEB-TACE can cause misleading hyper-enhancement in CE-US which can last up to 2 weeks post-treatment and interfere with perfusion visualization and quantification [33, 27]. Additionally, all CE imaging is limited by time and dose of contrast agents in the blood stream, making any real-time treatment evaluation difficult.

Compared to CE-US, because conventional non-contrast Doppler ultrasound imaging measures the signal from moving red blood cells directly as opposed to contrast agents, it is less susceptible to misleading enhancements from the TACE treatment. For this reason, non-contrast ultrasound is a potential solution for treatment assessment during or immediately after treatment. Having immediate and reliable treatment evaluation could potentially increase treatment response rates by allowing for repeat treatments to occur during the same session, which would also be both cost and time effective for the patient and interventional radiologist. Additionally, without contrast, imaging is not constrained by time and dose of contrast agents in the blood stream, allowing for unlimited scanning time and intra-procedural imaging. However, conventional power Doppler ultrasound techniques without contrast agents have been shown to be limited by attenuation and tissue clutter for perfusion imaging applications in the past [34, 35, 14, 36], as discussed in more detail in the following section.

1.4 Challenges with Non-Contrast Ultrasound Perfusion Imaging

Although power Doppler is superior to other Doppler techniques for measuring slow flow, it has significant limitations when it comes to measuring perfusion (i.e., the slowest flow in the smallest vessels). A few of the main limitations are presented in this section.

1.4.1 Spectral Broadening of the Tissue Clutter Signal

In a realistic setting, the tissue signal will not be well separated from the blood signal, as was shown in Figure 1.4, due primarily to sonographer hand motion and patient physiological motion [14]. This motion will cause tissue to move at greater velocities than blood, causing a spectral broadening of the tissue clutter signal, as shown in Figure 1.5. These velocities can be similar to or even higher than those from slow flow, resulting in the tissue clutter signal overlapping with, and overpowering, the signal from lower velocity blood flow. Conventional Doppler methods are therefore limited to blood velocities higher than

those of tissue clutter. This scenario is depicted in Figure 1.5 where the low blood velocity signal (red dotted line) is below the high pass filter cutoff and would therefore be attenuated upon application of the high pass filter.

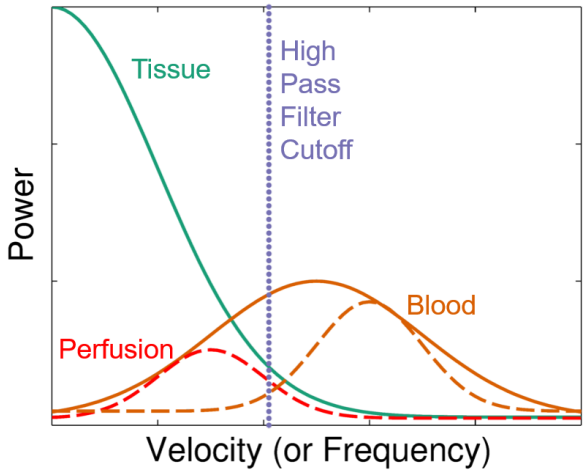

Figure 1.5: Schematic depicting spectral broadening of the tissue clutter signal and the resulting overlap of tissue and perfusion signals. Non-perfusion blood signal is shown as the dotted orange curve.

Considering only patient physiological and sonographer hand motion as the primary sources of tissue clutter, Heimdal et al. estimated theoretical lower bounds on blood velocity estimates at different imaging frequencies with conventional Doppler imaging [14]. Based on this work, it has been long claimed that ultrasound without contrast agents is limited to blood velocities greater than 5mm/s for clinical center frequencies less than 8MHz [14, 36], as shown in Figure 1.6. This limitation eliminates sensitivity to small vessels such as capillaries, venules, and 17-32μm diameter arterioles, which have average velocities of 0.33mm/s, 3.3mm/s and 2-4mm/s, respectively [14, 37]. Perfusion imaging is therefore seemingly impossible with conventional ultrasound methods because perfusion constitutes the slowest blood flow in the capillaries or smallest vasculature.

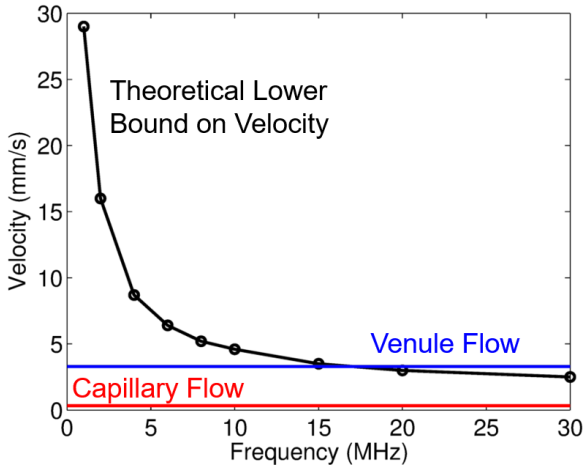

Figure 1.6: Theoretical lower bound on velocity estimation with ultrasound for different imaging frequencies is shown in black. Average venule and capillary flow are shown in blue and red, respectively.

1.4.2 Ensemble Length and Frame Rate

In addition to the spectral broadening problem, Doppler techniques involve a tradeoff between accuracy of velocity estimates and frame rate [10]. Specifically for slow flow, the minimum detectable velocity is inversely proportional to the number of slow-time points or ensemble length N,

$$v_{min} = \frac{c f_{prf}}{2N f_0} \tag{1.5}$$

where c is the speed of sound, f_{prf} if the pulse repetition frequency (PRF), and f_0 is the center frequency of the transmitted ultrasound pulse [1]. Increasing N will allow for lower velocities to be detected. Additionally, larger ensemble lengths increase the sensitivity of the power Doppler estimate, as shown in Equation 1.4 [10]. Furthermore, as mentioned in section 1.2, larger ensembles ensure sufficient sampling for high-pass filtering. However, because conventional Doppler sequencing acquires multiple A-lines through slow time for a single lateral location at a time, large ensembles lower the frame rate, diminishing real-time capabilities.

1.5 Potential Solutions for Imaging Perfusion with Non-Contrast Ultrasound

Because of the discussed limitations, it has been assumed that perfusion imaging with conventional ultrasound techniques is impossible without using contrast agents [14, 36]. This notion has been expressed in studies as recent as 2014 [36]. However, there have been significant advancements in recent years that have overcome some of these limitations, making slow flow imaging more attainable with non-contrast ultrasound. This section will discuss these potential solutions as well as some of the remaining challenges.

1.5.1 Adaptive Pre-Filter Phase Shift

In an attempt to better separate the tissue clutter and blood signals prior to high-pass filtering, Bjaerum and Torp expanded upon a method introduced by Thomas and Hall that involves adaptively modulating the tissue clutter bandwidth at each depth to be centered around DC before applying a conventional high pass filter [15, 19]. The basic idea behind the method is shown in Figure 1.7.

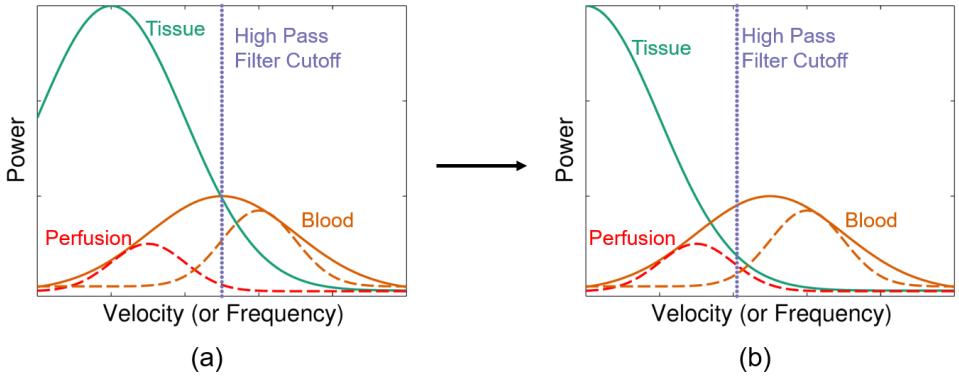

Figure 1.7: Schematic describing adaptive pre-filter phase shift. (a) Tissue signal has non-zero mean velocity. (b) Phase shift modulates the tissue signal to be about DC, allowing for more blood signal to be conserved.

As mentioned in section 1.4.2, when trying to maintain real-time frame rates with conventional Doppler acquisitions, ensemble lengths need to be relatively short. Because of this, the tissue motion can result in a non-zero mean Doppler frequency or velocity, causing

even more overlap with the signal from blood, as shown in Figure 1.7(a). By shifting the mean frequency of the tissue signal to DC, more blood signal can be resolved, as shown in Figure 1.7(b).

However, due to the spectral broadening of the tissue clutter signal caused by sonographer hand motion and patient physiological motion, even if the tissue clutter signal is modulated to be centered about DC, the bandwidth of the clutter still makes it impossible to separate the perfusion blood signal from the tissue clutter signal, as shown in Figure 1.7(b).

1.5.2 Plane Wave and Plane Wave Synthetic Focusing

Plane wave and plane wave synthetic focusing techniques are alternative beamforming methods that have, for the most part, solved the ensemble length and frame rate trade off problem [38, 39]. A plane wave sequence differs from a conventional focused sequence in that it acquires an entire image at once instead of each line at a time, allowing for much higher frame rates and longer ensemble lengths to be achieved simultaneously. It works by applying no delays on transmit, thereby transmitting an unfocused wave into the medium. The received channel signals are then delayed and focused using parallel receive beamforming before summing across the aperture [38, 39]. Parallel receive beamforming applies delays for each lateral location or beam to the same 2D receive data set, resulting in a 3D receive data set: axial (depth) by channel by beam (lateral position). Summing occurs along the channel dimension to generate a conventional 2D RF amplitude or B-mode image as described in section 1.1.1. However, because no focusing is used on transmit, the resulting image will have lower spatial resolution and signal-to-noise ratio (SNR) than with conventional techniques [38]. To regain resolution and SNR, transmit focusing can be synthetically achieved by acquiring and then summing multiple angled plane wave low resolution images [39]. Depending on the application, typically only a few angles are needed to achieve resolution and SNR that are comparable to focused images [10, 39]. Therefore, frame rates and ensemble lengths are still much higher and longer than with conventional

sequencing.

These methods have allowed for the implementation of more effective high pass filtering and more accurate velocity estimation, including improved power Doppler sensitivity for slow-flow applications [10, 38, 39]. Additionally, with these longer acquisition sequences, the Doppler frequency shift of tissue clutter discussed in the previous section becomes less of a problem since tissue does not typically move uniformly over long periods of time and will therefore already be centered about DC. However, similar to the pre-filter phase shift, plane wave and plane wave synthetic focusing do not solve the spectral broadening problem of the tissue clutter signal. Therefore, even though they can allow for a perfectly optimized and sufficiently sampled conventional high pass filter, these methods will be unable to preserve the slowest flow.

1.5.3 Coherent Flow Power Doppler

In addition to plane wave and plane wave synthetic focusing, coherent flow power Doppler (CFPD) has been proposed as an alternative beamforming method for improving imaging of slow flow in small vessels [40, 41]. CFPD uses short-lag spatial coherence (SLSC) receive beamforming in combination with power Doppler processing [40]. SLSC beamforming differs from conventional delay and sum beamforming (described in section 1.1.1) in how it generates a single line from the channel data. In conventional delay and sum, the channel signals are summed to generate a single A-line. In SLSC beamforming, an average normalized covariance is computed across the aperture to generate a single SLSC line [40, 42]. Specifically, at a given depth, the average normalized covariance is computed for pairs of channel signals $s_i(n)$ separated by lag m as follows,

$$R(m) = \frac{1}{N-m} \sum_{i=1}^{N-m} \frac{\sum_{n=n_1}^{n_2} s_i(n) s_{i+m}(n)}{\sqrt{\sum_{n=n_1}^{n_2} s_i^2(n) \sum_{n=n_1}^{n_2} s_{i+m}^2(n)}} \tag{1.6}$$

where N is the total number of channel signals. This is computed for lags up to M. Nor-

malized covariance estimates for each lag are then averaged to generate a SLSC pixel value as follows,

$$V_{slsc} = \frac{1}{M} \sum_{m=1}^{M} R(m) \tag{1.7}$$

V_{slsc} is computed at every depth to generate a single SLSC line. SLSC lines are then concatenated the same way A-lines are in conventional delay and sum beamforming to generate an SLSC image. Apart from using SLSC beamforming, CFPD differs from conventional power Doppler imaging only in that it performs tissue clutter filtering on delayed channel data prior to computing the SLSC line. In conventional power Doppler, tissue clutter filtering is performed on the fully beamformed data. Additionally, since SLSC is a receive beamforming technique, SLSC and CFPD are compatible with any type of transmit beamforming, including plane wave synthetic focusing [40, 41].

SLSC and CFPD data are sensitive to spatially coherent structures and therefore work by suppressing incoherent noise and clutter. Compared to conventional power Doppler, CFPD has been shown to improve blood-to-background SNR by up to 30dB in relatively large vessels (2mm diameter) with relatively fast flow (30mm/s) [40]. It was also shown to improve smaller vessel detection (down to 0.5mm diameter) with slower flow (10mm/s) by up to 12.5dB [41]. However, although CFPD is able to suppress spatial clutter and noise, it does not suppress clutter in the slow-time domain. Therefore, as with plane wave and plane wave synthetic focusing, spectral broadening of the tissue clutter signal will still limit estimation of the slowest flow.

1.5.4 Eigen-Based Clutter Filtering

As explained in Section 1.4.1, the tissue clutter signal spectral broadening problem is encountered in the frequency domain of the slow-time dimension (i.e., along the ensemble). Several eigen-based filtering techniques have been proposed as solutions to this problem

because they operate in a different domain and incorporate statistical information about the clutter and blood signals [43, 44, 45, 46]. These methods use principle or independent component analysis (PCA or ICA) to take advantage of the temporally and spatially coherent nature of tissue compared to the temporally and spatially incoherent nature of blood flow. For example, Gallippi and Trahey proposed a time-domain blind source separation (BSS) technique that used ICA with polynomial regression to adaptively filter out tissue clutter in the slow-time dimension [44]. Although shown to be effective, these methods require sufficient temporal sampling which is often not achievable with conventional beamforming, which typically has only 8-16 slow-time samples [46]. More recently, Demene et al. addressed this problem by proposing a PCA-based singular value decomposition (SVD) algorithm using plane wave synthetic focusing imaging to achieve sufficient temporal sampling [17]. Moreover, with sufficient temporal sampling and therefore reasonably similar spatio-temporal statistics, two-dimensional as well as higher order decompositions are able to be performed [17, 47, 48]. Other methods have expanded upon this SVD filter approach by making it more adaptive to different spatial regions within the image [49, 45]. All of these methods have improved slow flow measurements with ultrasound. However, tissue motion can still cause an overlap in the eigen-domain [44, 48], and therefore imaging of the slowest flow or perfusion remains challenging.

1.5.5 Statistical Approaches

Statistical approaches have also been explored as a way to make blood perfusion imaging with non-contrast ultrasound more efficient [50, 51, 52, 53]. These techniques use ideal discriminator (ID) methods to classify ultrasound signals through slow-time as either containing perfusion or not [52, 53]. Using this binary classification scheme, areas under receiver operator characteristic (ROC) curves can be used to quantify efficiency of the method at correctly classifying perfusion. These methods relies on full knowledge of the covariance matrices for different flow conditions, which is possible only with controlled

phantom or simulation experiments [53]. Therefore, although these methods have helped explain perfusion characteristics with ultrasound, they are not necessarily clinically applicable and thus not the focus of this dissertation.

Chapter 2

Developing an Adaptive Clutter Demodulation Scheme: Preliminary Studies

This work was originally published in [54]: Tierney, Jaime, et al. "Adaptive Clutter Demodulation for Non-Contrast Ultrasound Perfusion Imaging." *IEEE Transactions on Medical Imaging* 36.9 (2017): 1979-1991.

2.1 Introduction

In order to address the tissue clutter bandwidth limitation, we developed an adaptive frequency and amplitude demodulation scheme. This section will present a theoretical model that was derived to describe the method. Additionally, the practical implementation of the method will be explained. Finally, results from initial phantom experiments with intentional hand motion as well as no motion will be used to illustrate and validate the methodology.

2.2 Adaptive Tissue Clutter Demodulation Theory

2.2.1 Tissue Clutter and Blood Flow Models

A model for tissue vibration and blood flow has been previously derived by Heimdal and Torp [14]. For the purposes of this paper, we consider a simple realization of their classic model relevant to a single resolution cell. Assuming only stationary tissue is present in the field of view, the resulting signal at a given spatial location and slow-time point, t, could be represented as the sum of the complex amplitudes of the tissue scatterers,

$$s_{tissue} = \sum_{m=0}^{M-1} A_m \tag{2.1}$$

where A_m is the complex amplitude of a single scatterer and M is the total number of tissue scatterers. Since the scatterers are stationary over time, this signal is constant in the time domain and thus a delta function at DC in the frequency domain.

Similarly, if only blood were present, the resulting signal at time t could be represented as the sum of complex amplitudes modulated by the velocity term of each scatterer since each blood scatterer is moving at some variable speed,

$$s_{blood}(t) = \sum_{n=0}^{N-1} A_n e^{j\omega_n(t)t} \tag{2.2}$$

where A_n and $\omega_n(t) = \frac{2v_n(t)cos(\theta_n)\omega_0}{c}$ are the amplitude and angular frequency of a single blood scatterer, respectively, and N is the total number of blood scatterers. In the angular frequency equation, c is the speed of sound, $v_n(t)$ is the velocity of a single scatterer at time t, θ_n is the beam-to-flow angle of a single scatterer, and ω_0 is the angular transmit frequency. Since blood scatterers will be moving at some distribution of velocities, this signal would be broad-band and centered about the mean frequency or velocity of the blood scatterers in the frequency domain.

When both stationary tissue and flowing blood are present simultaneously, the signals in (2.1) and (2.2) are summed. To complete the model, a thermal noise component is also included in the sum,

$$s(t) = s_{tissue} + s_{blood}(t) + n(t) \tag{2.3}$$

Conceptually, for this case, the tissue and flowing blood are well separated in the frequency domain. Tissue clutter is therefore easily removed with conventional techniques.

When sonographer hand motion and patient physiological motion are present, the signal will include an additional velocity term that describes the resulting axial motion of both the

tissue and blood scatterers,

$$s(t) = (s_{tissue} + s_{blood}(t)) \times e^{j\omega_{physio+sono}(t)t} + n(t) \tag{2.4}$$

where $\omega_{physio+sono}$ is the angular frequency produced by patient physiological and sonographer hand motion. This motion causes a phase modulation that contributes to the spectral broadening of the tissue clutter bandwidth and causes an overlap between the tissue clutter and blood flow signals in the frequency domain. This spectral broadening makes conventional high pass filtering of the tissue clutter signal difficult when trying to image lower velocity blood flow.

2.2.2 Adaptive Tissue Clutter Demodulation Model

We propose a method that aims to estimate and correct for the patient physiological and sonographer hand motion in order to remove the added velocity term in (2.4),

$$s_{phaseDemod}(t) = ((s_{tissue} + s_{blood}(t)) \times e^{j\omega_{physio+sono}(t)t} + n(t)) \times e^{-j\hat{\omega}_{physio+sono}(t)t} \tag{2.5}$$

where $\hat{\omega}_{physio+sono}$ is an estimate of the angular frequency produced by patient physiological and sonographer hand motion. By correcting for this motion at each depth through slow-time, we are adaptively demodulating the tissue clutter bandwidth, and we assume the error induced by the demodulated noise is insignificant. In doing so, we are ideally left with (2.3), which, again, can easily be addressed with conventional filters.

However, due to non-axial tissue motion and inherent scanner variability, there will also be an amplitude modulation that will further contribute to the spectral broadening of the tissue clutter signal [14]. Amplitude modulation from tissue motion could result from residual axial motion as well as lateral and elevational motion. This amplitude modulation

can be simply described by a time dependence of the amplitude term in (2.1),

$$s_{tissue}(t) = \sum_{m=0}^{M-1} A_m(t) \tag{2.6}$$

To correct for this time dependence of the tissue amplitude, the signal at each time point can be normalized to the amplitude of the envelope or magnitude of the signal at that time point. Additionally, to preserve the power of the original signal, each term can then be multiplied by the power of the envelope of the signal. These operations are summarized in the following equation,

$$f_{norm}(t) = \frac{\sqrt{\frac{\sum_{l=1}^{L} |s_{tissue}(l)|^2}{L}}}{|s_{tissue}(t)|} \tag{2.7}$$

where L is the total number of slow-time points. By applying this correction to the tissue only signal, we remove the time dependence and are ideally left with (2.1),

$$s_{tissue}(t) \times f_{norm}(t) = s_{tissue} \tag{2.8}$$

However, this operation becomes more complicated when applied to (2.5) since $f_{norm}(t)$ will reflect amplitude modulation of both tissue and blood and will subsequently also demodulate the blood signal amplitude. Similar to the tissue signal, the blood signal will also exhibit a time dependence of the amplitude term,

$$s_{blood}(t) = \sum_{n=0}^{N-1} A_n(t) e^{j\omega_n(t)t} \tag{2.9}$$

Incorporating the amplitude modulated tissue and blood signals into (2.5), $f_{norm}(t)$ of the phase demodulated signal becomes

$$f_{norm}(t) = \frac{\sqrt{\frac{\sum_{l=1}^{L} |s_{phaseDemod}(l)|^2}{L}}}{|s_{phaseDemod}(t)|} \tag{2.10}$$

By applying (2.10) to the phase demodulated signal, we are left with a phase and amplitude demodulated signal,

$$s_{phase+ampDemod} = s_{phaseDemod}(t) \times f_{norm}(t) \tag{2.11}$$

This normalization demodulates all of the signal amplitude, including the blood, which causes the signal to become constant through slow-time.

To avoid demodulating the blood signal amplitude, we can take advantage of the difference in temporal coherence length between tissue and blood. The blood signal has a shorter coherence length so it is possible to apply a median filter to $f_{norm}(t)$ that is large enough to not incorporate changes in blood amplitude while still small enough to capture significant tissue amplitude modulation. In doing so, we can approximate (2.7) from (2.10),

$$\begin{aligned} f_{norm}(t) &= R\{\frac{\sqrt{\frac{\sum_{l=1}^{L}|s_{phaseDemod}(l)|^2}{L}}}{|s_{phaseDemod}|}, k\} \\ &\approx \frac{\sqrt{\frac{\sum_{l=1}^{L}|s_{tissue}(l)|^2}{L}}}{|s_{tissue}(t)|} \end{aligned} \tag{2.12}$$

where $R\{x,k\}$ represents the median filter operation on signal x of size k samples. Substituting the median filtered $f_{norm}(t)$ for (2.10) in (2.11), tissue amplitude modulation can be removed while blood amplitude modulation is preserved,

$$\begin{aligned} s_{phase+ampDemod}(t) &= (s_{tissue}(t) + s_{blood}(t) + n(t)) \\ &\quad \times f_{norm}(t) \\ &\approx s_{tissue} + s_{blood}(t) + n(t) \end{aligned} \tag{2.13}$$

We are then left with (2.3), which, again, can easily be addressed with conventional filters.

2.3 Adaptive Tissue Clutter Demodulation Implementation

To implement the described phase demodulation, we first use a standard 2D autocorrelation method to compute relative displacements between temporally adjacent beamformed RF lines [6]. Then, similar to approaches used in phase aberration estimation [55, 56], absolute displacements relative to the first RF line can be reconstructed by solving the following system of equations in a least square error sense,

$$\begin{bmatrix} 0 \\ d_{01} \\ d_{10} \\ d_{12} \\ \vdots \\ d_{L-1L-2} \end{bmatrix} = \begin{bmatrix} 1 & 0 & 0 & \cdots & 0 \\ -1 & 1 & 0 & \cdots & 0 \\ 1 & -1 & 0 & \cdots & 0 \\ 0 & -1 & 1 & \cdots & 0 \\ \vdots & \vdots & \vdots & \ddots & \vdots \\ 0 & 0 & 0 & \cdots & 1 \end{bmatrix} \begin{bmatrix} D_0 = 0 \\ D_1 \\ D_2 \\ D_3 \\ \vdots \\ D_{L-1} \end{bmatrix} \tag{2.14}$$

where d_{mn} represents the relative displacement estimate between time steps m and n (we assume that $d_{mn} = -d_{nm}$, which is not true for all motion estimators), D_l represents absolute displacement at slow-time point l, and L represents the number of samples through slow-time. Since we are using a lag of 1, this computation is the same as taking a cumulative sum of the relative displacements through slow-time.

A shape-preserving piecewise cubic interpolation can then be used to interpolate each RF line through depth from the computed absolute displacement to zero displacement, which is equivalent to adaptively demodulating the slow-time signal based on the tissue motion. For this method to work, we assume that the tissue is sufficiently bright relative to the blood signal so that only tissue displacement is measured by the 2D autocorrelation [57].

As described in the previous section, to minimize tissue signal amplitude variation through slow-time while still preserving the power of the signal, each interpolated RF signal through slow-time is normalized to the amplitude of the envelope of the signal divided

by the amplitude of the power of the envelope of the signal. This normalization function is described in (2.10) and is applied to the RF signal through slow-time. In comparison to (2.11), because the normalization is applied to the real part of the signal, this phase and amplitude demodulated signal is not constant through slow-time and does not fully demodulate the blood signal. Before this correction is applied, the normalization function is median filtered through slow-time as in (2.12) to avoid blood signal amplitude demodulation, as described in the previous section.

It is worth noting that, for simplicity, a narrow-band model was used to describe the theory. However, in practice, because we perform corrections in the time domain, the implementation is wide-band. Specifically, despite our narrow-band description, which suggests different adaptive modulation signals for each frequency, in practice, we estimate a single average displacement and amplitude fluctuation and assume they apply equally well to all frequencies.

2.4 Proof of Concept Experiments

Two proof-of-concept experiments were performed to confirm proper development of the method. First, to validate the full adaptive tissue clutter demodulation scheme at suppressing the bandwidth of the tissue clutter signal, an intentional hand motion experiment was performed using a quality assurance phantom (CIRS Model 040GSE, Norfold, Virginia). Because the phantom was stationary, sonographer hand motion was the only source contributing to the bandwidth of the tissue clutter signal. Additionally, to demonstrate the need for the described amplitude demodulation and to confirm its functionality, a no motion phantom experiment was performed. For this experiment, inherent scanner variability was the only contributing source of phase and amplitude modulation.

2.4.1 Data Acquisition and Beamforming

Channel data from a plane wave transmit sequence were acquired using a Verasonics Vantage Ultrasound System (Verasonics, Inc., Kirkland, WA) and L12-5 linear array probe with a 7.8MHz center frequency. Data were acquired at a PRF of 1000Hz to an end depth of 3cm. The center line of each plane wave acquisition was beamformed using parallel receive beamforming to generate an M-mode image. A Hann apodization and aperture growth with an F/# of 2 were implemented during receive beamforming. RF data were up-sampled through depth by a factor of 2 and band-pass filtered. All beamforming and signal processing were done in MATLAB R2014a (The MathWorks, Inc., Natick, MA).

2.4.2 Intentional Hand Motion Phantom Experiment

A single subject acquired channel data of the phantom for 3s. During the scan, the subject intentionally moved their hand to create exaggerated tissue clutter motion. The data were beamformed and then processed using the adaptive tissue clutter phase and amplitude demodulation scheme described in Sections 2.2 and 2.3. No median filtering was used during the amplitude demodulation.

To qualitatively demonstrate the absolute displacement computation described in Equation 2.14, example absolute displacement profiles through slow-time are shown in Figure 2.1 superimposed on top of the intentional hand motion M-mode image. This result confirmed that the displacement estimation scheme accurately measures total displacements through slow-time for an extreme case.

To illustrate adaptive demodulation, examples of hand motion M-mode data sets before and after adaptive demodulation are shown in Figures 2.2a and 2.2b, respectively. These images show how adaptive demodulation successfully removes tissue clutter motion through slow-time. For the same examples, average spectra before and after adaptive demodulation are shown in Figure 2.2c. This result confirms that the method suppresses the

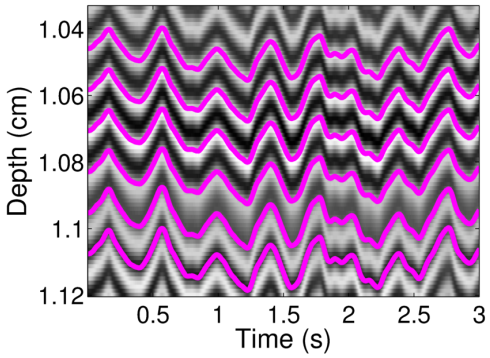

Figure 2.1: Displacement profiles in pink superimposed on top of corresponding RF lines through slow-time are shown for several depths.

bandwidth of the tissue clutter signal, as expected.

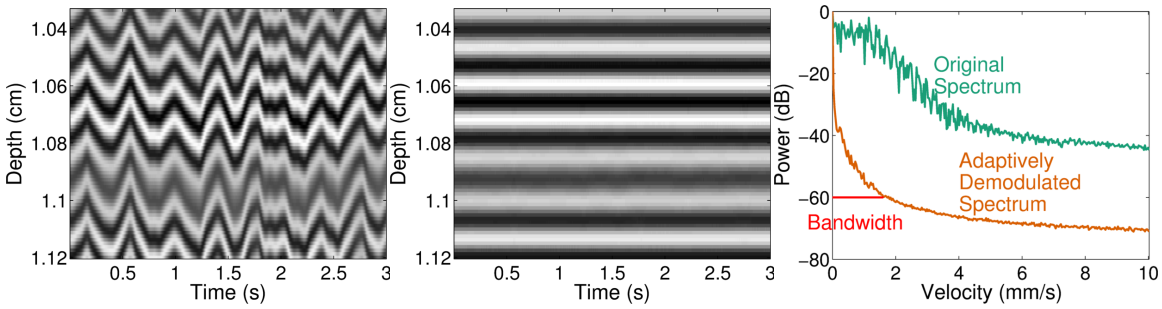

(a) Before AD (b) After AD (c) Example Spectra

Figure 2.2: (a) Example M-mode data before adaptive demodulation. (b) Example M-mode data after adaptive demodulation. (c) The average spectra through slow-time before and after adaptive demodulation are shown in teal and orange, respectively. Example half-width bandwidth estimate at -60dB is shown in red.

2.4.3 No Motion Phantom Experiment

For the no motion phantom experiment, a ring stand and probe holder were used to ensure that no sonographer hand motion, patient physiological motion, or blood flow were present. Channel data were acquired for 3s.

Amplitude through slow-time is qualitatively compared between raw RF data, phase demodulated RF data, and phase and amplitude demodulated (with and without median filtering) RF data for two example depths in Figure 2.3. A 35 sample median filter was

used for the median filtered case. Additionally, the power of each signal was computed and compared to ensure that the amplitude demodulation preserves signal power as expected.

Because no added motion is present, this result shows that amplitude modulation can result from inherent scanner variation. For the two example depths (from the same data set) shown in Figure 2.3, large variable trends in amplitude modulation are present in the baseline data. Amplitude decreases through slow-time in Figure 2.3a while it increases through slow-time in Figure 2.3b. For both example depths, phase demodulation is able to correct for this larger bias, while amplitude demodulation is able to correct for additional smaller variations in amplitude, as seen in both Figures 2.3a and 2.3b. Additionally, both phase and amplitude demodulation preserve the power of the baseline signal as seen in the power estimates shown next to corresponding labels.

The results from this experiment demonstrate the need for an amplitude demodulation step to more completely suppress the tissue clutter bandwidth. However, as discussed in Section 2.2, the proposed method will also likely suppress the blood signal without median filtering. Further exploration of median filtering of the normalization function is therefore included in the following research design and methods.

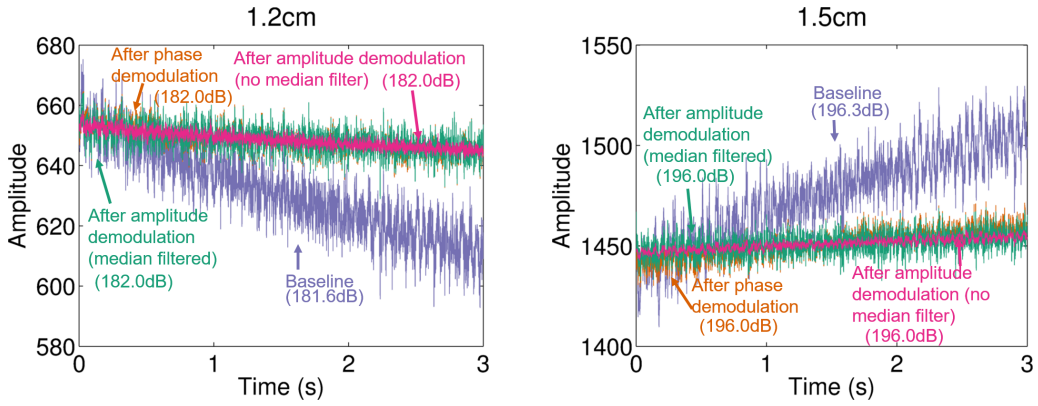

Figure 2.3: Amplitude through slow-time is shown for two example depths from the same data set. For each depth, amplitude is shown for the raw RF data (purple), phase demodulated RF data (orange), and phase & amplitude demodulated RF data with (teal) and without (pink) median filtering. Individual power estimates in dB for each line are shown next to corresponding labels.

Chapter 3

Evaluation of Adaptive Clutter Demodulation for Non-Contrast Ultrasound Perfusion Imaging

This work was originally published in [54]: Tierney, Jaime, et al. "Adaptive Clutter Demodulation for Non-Contrast Ultrasound Perfusion Imaging." *IEEE Transactions on Medical Imaging* 36.9 (2017): 1979-1991.

3.1 Introduction

Preliminary study results presented in Chapter 2 suggest that adaptive tissue clutter demodulation has the potential to be an effective solution to the spectral broadening problem described in Section 1.4.1. Additionally, because it has been implemented using plane wave sequencing, it also addresses the frame rate and ensemble length limitations. By overcoming both of these problems, we demonstrate in this chapter how the proposed technique has the potential to allow for detection of blood flow well below assumed fundamental limits [14]. We accomplish this through sonographer hand motion phantom, *in vivo*, and controlled simulation experiments, as described in more detail in the following sections.

3.2 Experiments

3.2.1 Data Acquisition and Beamforming

Channel data from plane wave transmit sequences were acquired using a Verasonics Vantage Ultrasound System (Verasonics, Inc., Kirkland, WA), L12-5 linear array probe, and C5-2 curvilinear array probe. Data were acquired at center frequencies of 7.8MHz and 3.1MHz to end depths of 3cm and 8cm with the L12-5 and C5-2 probes, respectively.

Three different plane wave acquisition methods were used and will be referred to as follows: single plane wave (SPW), plane wave synthetic focusing (PWSF), and multiple plane wave (MPW). For the SPW method, 0° plane waves were acquired at a PRF of 1kHz. For the PWSF case, plane waves angled between -8° to 8° spaced by 2° were acquired at a PRF of 9kHz. All 9 angles were used to generate a single frame using the method by Montaldo et al., resulting in a final PRF of 1kHz [39]. For the MPW case, 0° plane waves were acquired at a PRF of 9kHz and 9 consecutive plane waves were summed together after beamforming to generate a single frame, again resulting in a final PRF of 1kHz.

All data sets were beamformed with a Hann apodization on receive, and aperture growth with an F/# of 2 was implemented during beamforming. To obtain a final sampling frequency greater than or equal to 50MHz, RF data were upsampled through depth by an integer number of samples (i.e. by 2 and 4 to achieve 62.5MHz and 50MHz sampling frequencies for the data acquired with the L12-5 and C5-2 probes, respectively). Before further processing, a FIR band-pass filter was applied to the beamformed RF data.

All beamforming and signal processing for all studies were done in MATLAB R2014a (The MathWorks, Inc., Natick, MA).

3.2.2 Sonographer Hand Motion Phantom Experiment

Six volunteers were recruited for three separate trials to acquire channel data using a quality assurance phantom (CIRS Model 040GSE, Norfolk, Virginia) for 3s using a transmit voltage of 30.7V. For the first trial, the L12-5 probe and PWSF acquisition method were used. The 0° plane wave acquisitions from this sequence were used to generate SPW data. For the second trial, the L12-5 probe and MPW acquisition method were used. Since the PWSF and MPW methods theoretically improve SNR, trials 1 and 2 were performed to assess signal-to-noise ratio (SNR) limitations of the standard SPW method that is used for all other studies in this paper. Additionally, since the PWSF method focuses on transmit while the SPW and MPW methods do not, the effects of transmit beamforming induced spectral

broadening were also examined. The third trial used the C5-2 probe and SPW acquisition method. This trial provided an assessment of the algorithm at a lower imaging frequency (3.1MHz), compared to the standard 7.8MHz imaging frequency used for the rest of the studies. For all three trials, the phantom was stationary, so that sonographer hand motion was the only variable causing clutter motion in the acquired data. All four imaging cases are summarized in Table 3.1 and labeled as cases 1 through 4.

For each imaging case, the center line of each plane wave acquisition was beamformed to generate an M-mode image. The adaptive clutter demodulation scheme (described in Sections 2.2 and 2.3) was performed on each M-mode image. A median filter of 35 samples (35ms) was used for the amplitude demodulation. Using the same cutoffs as the first band-pass filter, an additional FIR band-pass filter was applied to the RF data through depth. For each subject, full-width bandwidths were computed on averaged power spectra at -60dB before and after adaptive demodulation. The bandwidths were then averaged across subjects. Figure 2.2 shows an example half-width bandwidth estimate of the adaptively demodulated average spectrum at -60dB. Additionally, full-width bandwidths were computed relative to the thermal noise floor. For this metric, the mean was subtracted from each signal prior to estimating its power spectrum. For both bandwidth metrics, corresponding velocity estimates in mm/s were computed using $v = \frac{f*c*1000}{2*f_0}$, where f is slow-time frequency in Hz, c is the speed of sound in m/s, and f_0 is the center frequency in Hz.

Additionally, to compare the individual effects of the phase and amplitude demodulation steps, bandwidth values were also computed for data with phase demodulation only and with amplitude demodulation only (using a median filter of 35 samples) for the SPW case from trial 1 (imaging case 2). Furthermore, phase and amplitude demodulation with two additional median filters of size 71 and 141 samples (71ms and 141ms) as well as phase and amplitude demodulation with no median filtering were compared for this case to assess the effects of median filtering on the tissue clutter bandwidth.

3.2.3 *In Vivo* Experiments

Two experiments were performed to assess *in vivo* feasibility: an arterial occlusion (reactive hyperemia) experiment and a muscle contraction (exercise hyperemia) experiment. Informed written consent in accordance with Vanderbilt University's institutional review board (IRB) was given by two subjects prior to the start of the studies. The first subject was a healthy 35 year old male, and the second subject was a healthy 44 year old male. For both studies, data were acquired at a transmit voltage of 16.1V using the L12-5 probe and SPW method.

For the arterial occlusion experiment, ultrasound data were acquired of the first subject's left gastrocnemius muscle. To prevent the muscle from being compressed against the scanning bed, the subject's left calf was raised slightly and his left foot was secured while lying supine. To ensure continual contact of the probe, hand-held assistance was used in combination with a stationary holder to hold the probe beneath the gastrocnemius muscle. Just above the subject's left knee, a thigh blood pressure cuff (Model CC22, Hokanson, Bellevue, WA) was placed and inflated within 1s to 300mmHg using a rapid cuff inflator (Model E20, Hokanson, Bellevue, WA). To induce arterial occlusion in the calf, the cuff was kept inflated for 5min [58, 59, 60]. Data were acquired for 30s after the 5 minute occlusion. The cuff was rapidly released about 4s into the scan. This imaging case is summarized in Table 3.1 and labeled as case 5.

For the muscle contraction experiment, ultrasound data were acquired of the second subject's left tibialis anterior muscle. While lying supine, the subject's left calf was slightly raised and his left foot was secured in a custom-built foot device [61]. A volunteer held the probe on the tibialis anterior muscle and data were acquired for 30s. About 8s into the scan the subject was instructed to dorsiflex his left foot to contract and induce subsequent perfusion in the tibialis anterior muscle. After 5s the subject relaxed his foot. This imaging case is summarized in Table 3.1 and labeled as case 6.

For both *in vivo* studies, for every 50ms time point, data were broken up into 2s time

frames, and each time point was processed separately. Using parallel receive beamforming, full images were formed from each plane wave transmit.

Adaptive clutter demodulation was applied to each *in vivo* time point using the methods described in Sections 2.2 and 2.3. A median filter of 35 samples (35ms) was used for the amplitude demodulation. Using the same cutoffs as the first band-pass filter, an additional FIR band-pass filter was applied to the RF data through depth. Four fourth order Butterworth filtering cases were compared: a 20Hz high pass applied to adaptively demodulated (i.e., both phase and amplitude demodulated) RF data (proposed filter case), a 20Hz high pass applied to phase demodulated RF data (proposed filter case with no amplitude demodulation), a 20Hz high pass applied to normal RF data, and a 50Hz high pass applied to normal RF data. An additional 80Hz high pass case was compared for a single time point of the occlusion data. For each method and signal through slow-time, a mirror reflection of the first 20 points was added to the beginning of the signal before filtering and removed after filtering. Power Doppler images were generated by computing power at each pixel using $P = 20log_{10}(\sqrt{\frac{\sum_{l=1}^{L} s^2(l)}{L}})$, where L is the number of slow-time points and $s(l)$ is the slow-time signal at time l. A 1mm by 1mm spatial median filter and a 7ms slow-time median filter were applied to each power Doppler image prior to log scaling.

For each filtering case and time point, the relative change in power from the last time point was measured at each pixel within a muscle region of interest (ROI). Due to large motion artifacts during the cuff release and contraction of the muscle, time points with 5th percentile normalized cross correlation values below 0.995 were not included when measuring the dynamic ranges of the relative median power. For each *in vivo* study, power Doppler images were scaled to dynamic ranges that qualitatively highlight differences between the filtering methods while maintaining similar noise floors.

Adaptive demodulation with no median filtering and with median filters of size 71 and 141 samples (71ms and 141ms) were also compared for a single time point for each *in vivo* case to further assess the effects of amplitude demodulation.

Table 3.1: Imaging cases are summarized by field of view (FOV), tissue clutter source, probe, acquisition method, and transmit voltage.

Case	FOV	Motion Clutter Source	Probe (Frequency)	Acq. Method	Transmit Voltage (V)
1	Phantom	Hand	L12-5 (7.8MHz)	PWSF	30.7
2	Phantom	Hand	L12-5 (7.8MHz)	SPW	30.7
3	Phantom	Hand	L12-5 (7.8MHz)	MPW	30.7
4	Phantom	Hand	C5-2 (3.1MHz)	SPW	30.7
5	*in vivo*	Patient & Hand	L12-5 (7.8MHz)	SPW	16.1
6	*in vivo*	Patient & Hand	L12-5 (7.8MHz)	SPW	16.1

3.2.4 SNR Comparison

The phantom and *in vivo* studies could potentially result in different SNRs due to different transmit voltages used for the acquisitions. Additionally, the PWSF and MPW methods will likely result in increased SNR. To quantify potential differences in SNR and its effect on the proposed algorithm, we computed SNR in each case using $SNR = \frac{\rho}{(1-\rho)}$, where ρ is the slow-time RF A-line to A-line normalized cross correlation value [62]. Kernel sizes of 5 and 1.25 wavelengths were used for the normalized cross correlation estimates for the *in vivo* contraction study and all other studies, respectively. The RF-lines were upsampled to a sampling frequency of 156MHz to improve the quality of the estimate. A sliding window of 1 sample was used to estimate ρ for every pair of RF lines over the first 2s of data from the *in vivo* and phantom acquisitions. We performed a Fisher transformation, and then averaged the estimates of ρ. We then estimated the SNR after performing the inverse transformation.

3.2.5 Simulation Experiment

Using similar methods as Li et al. [41], a simple simulation experiment was performed to confirm that the proposed technique can preserve slow blood flow in a controlled setting. Field II was used to simulate plane wave channel data of a single vessel using the same parameters as the L12-5 SPW acquisitions (7.8MHz frequency, 3cm end depth, PRF=1kHz) [63]. A single 0.5mm diameter vessel of blood scatterers was centered at a depth of 2cm at 60° to the beam within a 1.5 by 3cm area of tissue scatterers. To simulate tissue clutter, displacements estimated from one of the hand motion data sets were used to displace the tissue and blood scatterers. One second of data were simulated with blood scatterers moving under laminar flow with maximum velocities of 0.5mm/s, 1mm/s, and 2mm/s. However, because the flow was parabolic, the velocity of most of the simulated blood scatterers was lower than the respective maximum. Tissue and blood scatterers were both generated with a scattering density of 17 scatterers per resolution cell. The simulated signal from blood was scaled to be 40dB lower than the tissue. Thermal noise was added at 0dB relative to the blood signal.

Simulated channel data were then beamformed and processed the same way as for the *in vivo* studies. A fourth order 1Hz high pass Butterworth filter was applied to two different cases: adaptively demodulated RF data (using a 35 sample median filter for the amplitude demodulation) and normal RF data. Several additional filter cutoffs were compared for the 1mm/s case. Power Doppler images were generated and scaled the same way as for the *in vivo* data.

3.3 Results

The following sections present the results from the phantom, *in vivo*, SNR, and simulation experiments. Section 3.3.1 includes the sonographer hand motion phantom experiment results. The *in vivo* results are then shown in Section 3.3.2 followed by the SNR results in

Section 3.3.3. Finally, the simulation experiment results are presented in Section 3.3.4.

3.3.1 Sonographer Hand Motion Phantom Results

For the data acquired with the L12-5 probe (7.8MHz imaging frequency, imaging cases 1-3), adaptive demodulation resulted in average bandwidth estimates below 20Hz at -60dB for all three acquisition methods, allowing for velocities below 1mm/s to potentially be detected, as seen in Figure 3.1a and Table 3.2. Table 3.3 shows that, for these imaging cases, subsequent blood flow processing would need to provide a gain of at least 25dB above the noise floor to allow for detection of velocities below 1mm/s.

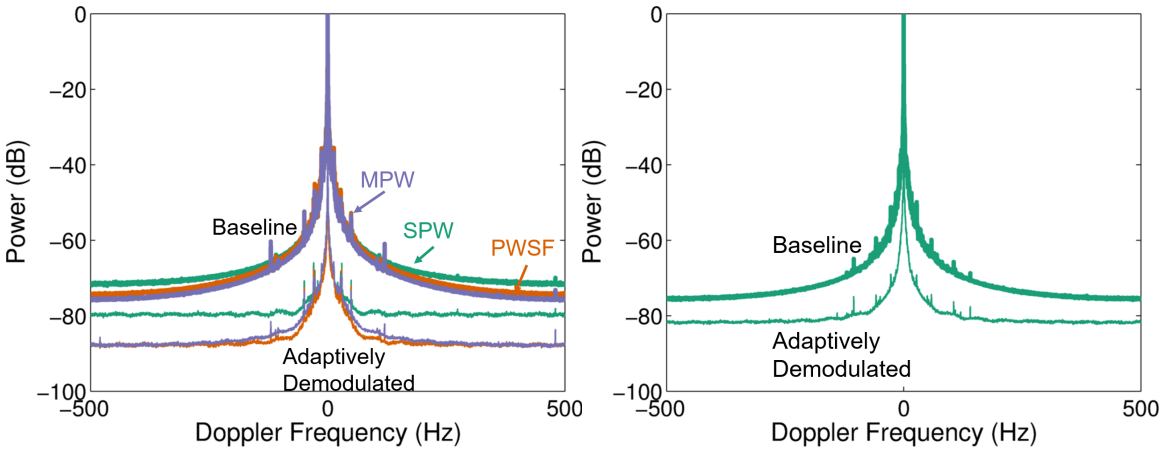

Figure 3.1: Spectra averaged through depth and across subjects are shown for (a) three beamforming methods, SPW (teal), PWSF (orange), and MPW (purple), before (thick) and after (thin) adaptive demodulation for the data acquired with the L12-5 probe (7.8MHz imaging frequency, imaging cases 1-3) and (b) the SPW beamforming method before (thick) and after (thin) adaptive demodulation for the data acquired with the C5-2 probe (3.1MHz imaging frequency, imaging case 4). A 35 sample median filter was used for the adaptive demodulation for both cases.

For the data acquired with the C5-2 probe (3.1MHz frequency, imaging case 4), adaptive demodulation resulted in an average bandwidth of 22.0Hz at -60dB, allowing for velocities below 2.71mm/s to potentially be detected, as shown in Figure 3.1b and Table 3.2. Table 3.3 shows that, for this imaging case, subsequent blood flow processing would need

Table 3.2: Bandwidths (BWs) averaged across subjects and corresponding velocities at -60dB before and after adaptive demodulation for the sonographer hand motion experiment (imaging cases 1-4). Standard error of the mean is shown in parenthesis for each measurement.

Imaging Case	BW Before (Hz)	Velocity Before (mm/s)	BW After (Hz)	Velocity After (mm/s)
1 (PWSF, 7.8MHz)	168 ($\pm$ 25.0)	8.26 ($\pm$ 1.23)	5.11 ($\pm$ 1.28)	0.25 ($\pm$ 0.06)
2 (SPW, 7.8MHz)	175 ($\pm$ 25.7)	8.60 ($\pm$ 1.26)	10.5 ($\pm$ 6.49)	0.52 ($\pm$ 0.32)
3 (MPW, 7.8MHz)	177 ($\pm$ 32.0)	8.74 ($\pm$ 1.58)	10.6 ($\pm$ 4.12)	0.52 ($\pm$ 0.20)
4 (SPW, 3.1MHz)	135 ($\pm$ 15.2)	16.6 ($\pm$ 1.87)	22.0 ($\pm$ 6.62)	2.71 ($\pm$ 0.82)

to provide a gain of at least 25dB above the noise floor to allow for detection of velocities below 2mm/s.

Figure 3.2 and Table 3.4 show the results for the individual effects of phase and amplitude demodulation as well as the effects of median filtering with the amplitude demodulation on the tissue clutter bandwidth for the L12-5 SPW method (7.8MHz imaging frequency, imaging case 2). These results show that with only amplitude demodulation (no phase demodulation), minimal suppression of the bandwidth is seen (175Hz suppressed to 168Hz). Phase demodulation alone suppresses the bandwidth pretty well. At -60dB, phase demodulation (no amplitude demodulation) resulted in a full-width bandwidth of 35.8Hz (1.76mm/s). The combination of phase and amplitude demodulation further improved the bandwidth suppression, with smaller median filter sizes resulting in increased suppression. Phase and amplitude demodulation with no median filtering decreased the bandwidth to 4.78Hz (0.24mm/s), while phase and amplitude demodulation with 35 sample median filtering decreased the bandwidth to 10.5Hz (0.52mm/s). Although no median filtering produced the best results in terms of tissue clutter bandwidth suppression, it would also suppress the blood signal in a realistic application, as described in Sections 2.2 and 2.3.

Table 3.3: Bandwidths (BWs) relative to the noise floor averaged across subjects and corresponding velocities before and after adaptive demodulation for the sonographer hand motion experiment (imaging cases 1-4). The first column indicates dB above the noise floor. Standard error of the mean is shown in parenthesis for each measurement.

dB	Imaging Case	BW Before (Hz)	Velocity Before (mm/s)	BW After (Hz)	Velocity After (mm/s)
3	1 (PWSF, 7.8MHz)	477 (± 7.55)	23.5 (± 0.37)	227 (± 9.00)	11.2 (± 0.44)
3	2 (SPW, 7.8MHz)	413 (± 14.7)	20.3 (± 0.73)	168 (± 9.27)	8.29 (± 0.46)
3	3 (MPW, 7.8MHz)	567 (± 17.9)	28.0 (± 0.88)	647 (± 48.2)	31.9 (± 2.38)
3	4 (SPW, 3.1MHz)	403 (± 12.2)	49.7 (± 1.51)	255 (± 2.31)	31.4 (± 0.28)
25	1 (PWSF, 7.8MHz)	67.6 (± 4.17)	3.33 (± 0.21)	15.4 (± 3.63)	0.76 (± 0.18)
25	2 (SPW, 7.8MHz)	50.2 (± 2.79)	2.48 (± 0.14)	2.50 (± 0.31)	0.12 (± 0.02)
25	3 (MPW, 7.8MHz)	83.3 (± 7.54)	4.10 (± 0.37)	17.4 (± 1.87)	0.86 (± 0.09)
25	4 (SPW, 3.1MHz)	46.9 (± 1.66)	5.78 (± 0.20)	8.83 (± 0.64)	1.09 (± 0.08)

3.3.2 *In Vivo* Results

Figures 3.3a and 3.4a show that the proposed filter case resulted in a larger dynamic range within the muscle compared to the case with no amplitude demodulation and the two conventional filters for both *in vivo* studies. For the occlusion study, dynamic ranges between the highest and lowest blood flow time points were 4.73dB, 1.79dB, 2.1dB and 0.15dB for the proposed, proposed with no amplitude demodulation, 20Hz conventional, and 50Hz conventional filters, respectively. For the contraction study, dynamic ranges between the highest and lowest blood flow time points were 4.80dB, 0.91dB, 1.95dB and 0.16dB for the proposed, the proposed with no amplitude demodulation, 20Hz conventional, and 50Hz conventional filters, respectively.

Figures 3.3b and 3.4b further support these results qualitatively. Compared to the case

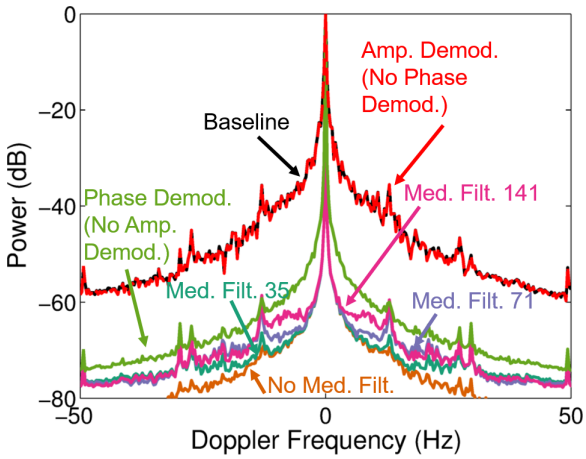

Figure 3.2: Spectra averaged through depth across subjects are shown for the data acquired with the L12-5 probe and SPW acquisition method (7.8MHz imaging frequency, imaging case 2) for different steps of the adaptive demodulation scheme. The frequency axis is cropped to highlight differences at -60dB. Spectra are shown for baseline (black), after amplitude demodulation (red), after phase demodulation (green), and after phase & amplitude demodulation with median filter sizes of 141 (pink), 71 (purple), 35 (teal), and no median filter (orange).

with no amplitude demodulation and the conventional filter cases, the proposed filter case shows larger differences between the time points during occlusion and before contraction (2s and 5s, respectively) and the time points after occlusion and contraction (8, 22, and 30s for the occlusion case and 7 and 26s for the contraction case). Additionally, the case with no amplitude demodulation and the conventional filter cases show structure that is strongly correlated to structure seen in the B-mode images, whereas the proposed filter cases exhibit more independent structure, especially within the muscle ROI (between 0.5 and 1cm depths).

Time points between 4.55s and 6.95s were excluded when determining the axis in Figure 3.3a and the scaling of the images in Figure 3.3b. Time points between 7.7s and 15.65s were excluded when determining the axis in Figure 3.4a and the scaling of the images in Figure 3.4b. Excluded time points had 5th percentile normalized cross correlation values below 0.995.

Figure 3.5 shows power Doppler images for different amplitude demodulation meth-

Table 3.4: Average bandwidths (BWs) and corresponding velocities at -60dB after adaptive demodulation with amplitude demodulation, phase demodulation, phase & amplitude demodulation with varying median filter sizes, and phase & amplitude demodulation with no median filtering for data acquired with the L12-5 probe and SPW acquisition method (7.8MHz imaging frequency, imaging case 2). Standard error of the mean is shown in parenthesis for each measurement.

Demod. Method	BW After (Hz)	Velocity After (mm/s)
Amp	168 ($\pm$ 25.2)	8.29 ($\pm$ 1.24)
Phase	35.8 ($\pm$ 7.35)	1.76 ($\pm$ 0.36)
Phase & Amp. (No Med. Filt.)	4.78 ($\pm$ 1.08)	0.24 ($\pm$ 0.05)
Phase & Amp. (Med. Filt. 35)	10.5 ($\pm$ 6.49)	0.52 ($\pm$ 0.32)
Phase & Amp. (Med. Filt. 71)	14.6 ($\pm$ 7.12)	0.72 ($\pm$ 0.35)
Phase & Amp. (Med. Filt. 141)	28.0 ($\pm$ 7.53)	1.38 ($\pm$ 0.37)

ods. Images are shown for the 22s and 17s time points of the arterial occlusion and muscle contraction studies, respectively, at which we expect to see increased perfusion within the muscle. Increasing the size of the median filter used during amplitude demodulation increases the amount of B-mode structure seen in the power Doppler image, with the most B-mode structure seen when no amplitude demodulation is employed. Decreasing the size of the median filter appears to suppress the blood signal, but not completely. These trends support the results from the hand motion study which showed increased suppression of the tissue clutter with decreased median filter sizes used for the amplitude demodulation. These results also suggest that amplitude demodulation is able to suppress tissue clutter while still preserving blood flow.

Figure 3.6 shows larger views of the B-mode and power Doppler images before and after adaptive demodulation for the 22s time point of the *in vivo* occlusion scan. The normal B-Mode, normal power Doppler, and adaptively demodulated power Doppler images are the same as seen in Figure 3.3b for the 22s time point B-mode, 20Hz high pass, and

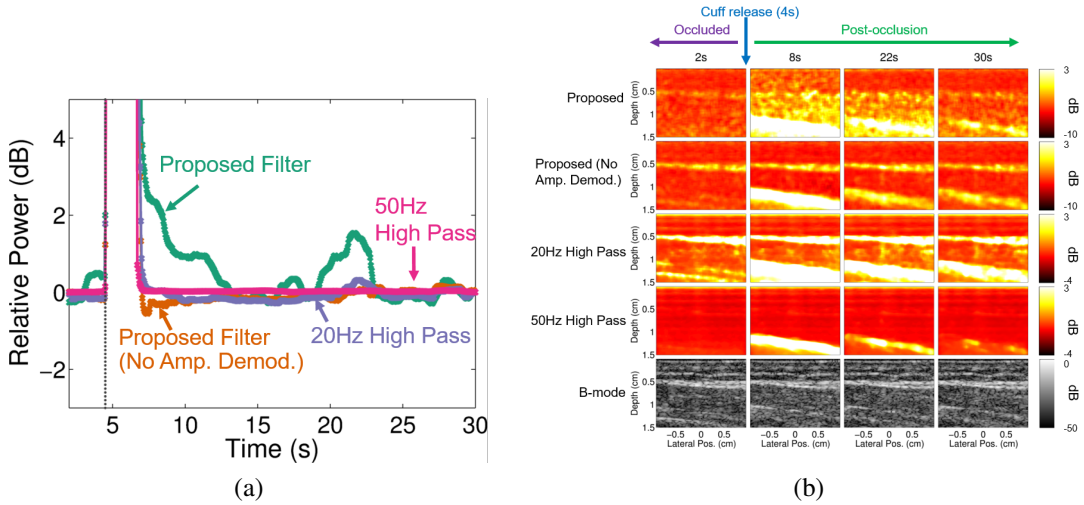

(a) (b)

Figure 3.3: (a) Median relative power with respect to the last *in vivo* arterial occlusion time point (for each filtering method) is plotted for every 50ms for each filtering case: proposed filter (teal), proposed filter with no amplitude demodulation (orange), 20Hz high pass (purple), and 50Hz high pass (pink). The time point at which the cuff was released is marked by the dark gray vertical dotted line (at about 4s). (b) Power Doppler and corresponding B-mode images (bottom row) are shown for 2, 8, 22, and 30 second time points of the *in vivo* arterial occlusion scan for each filtering case: proposed filter (first row), proposed filter with no amplitude demodulation (second row), 20Hz high pass (third row), and 50Hz high pass (fourth row).

proposed rows, respectively. The adaptively demodulated B-mode image is included in Figure 3.6 to show that the proposed phase and amplitude demodulation preserves B-mode structure. It also reveals new, independent power Doppler structure. This result therefore provides further evidence that power Doppler with adaptive demodulation suppresses tissue clutter while conserving blood signal compared to the conventional case, which has structure strongly correlated to the B-mode image. This observation is also supported quantitatively with normalized cross correlation values of 0.4743 and -0.0096 between the adaptively demodulated B-mode image and the conventional and adaptively demodulated power Doppler images, respectively.

Figure 3.7 shows power Doppler images with various dynamic ranges for the 22s time point of the occlusion scan for the proposed filter and conventional filter with different frequency cutoffs. Regardless of cutoff value, the conventional filter cases fail to resolve

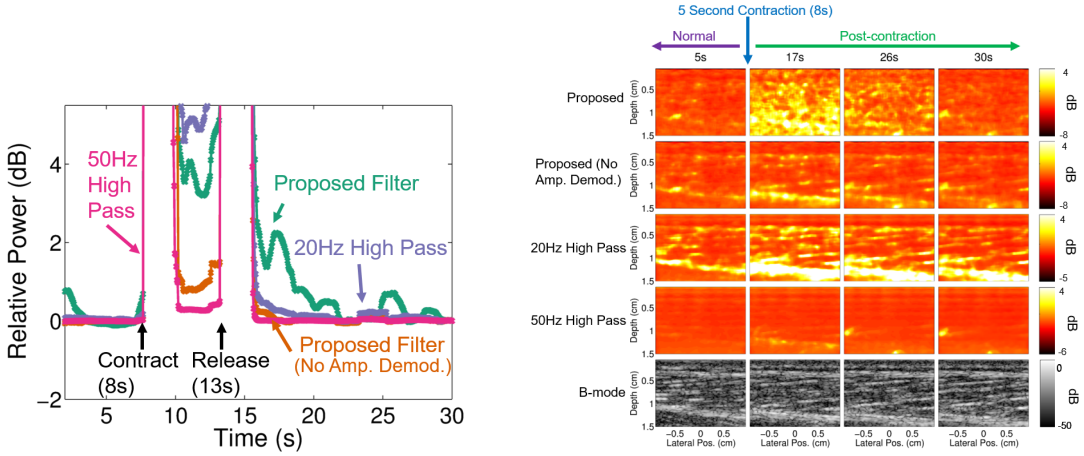

(a) (b)

Figure 3.4: (a) Median relative power with respect to the last *in vivo* muscle contraction time point (for each filtering method) is plotted for every 50ms for each filtering case: proposed filter (teal), proposed filter with no amplitude demodulation (orange), 20Hz high pass (purple), and 50Hz high pass (pink). The time points at which the muscle contracted and released are marked with arrows (at about 8s and 13s, respectively). (b) Power Doppler and corresponding B-mode images (bottom row) are shown for 5, 17, 26, and 30 second time points of the *in vivo* muscle contraction scan for each filtering case: proposed filter (first row), proposed filter with no amplitude demodulation (second row), 20Hz high pass (third row), and 50Hz high pass (fourth row).

any of the independent structure within the muscle that is seen in the proposed filter case.

3.3.3 SNR Results

SNR values for the hand motion data acquisitions were computed to be 37.7dB, 45.3dB, and 46.4dB, for the SPW, PWSF, and MPW sequences, respectively. For the *in vivo* data, SNR was computed to be 36.8dB and 40.9dB, for the occlusion and contraction studies, respectively.

3.3.4 Simulation Results

Figure 3.8 demonstrates that, compared to conventional power Doppler, the proposed technique can suppress tissue clutter while preserving slow flow. The vessel is clearly

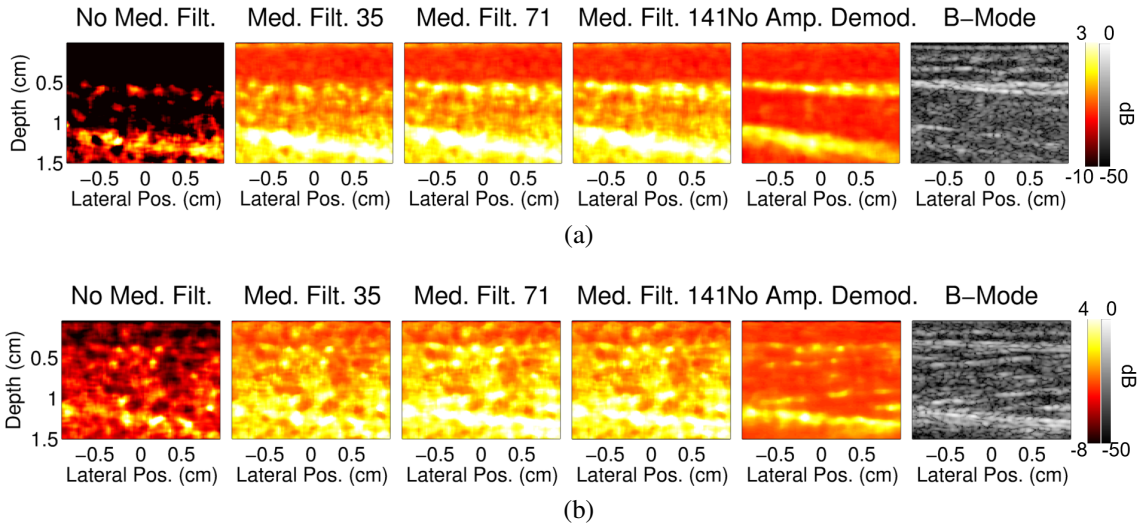

Figure 3.5: Power Doppler images are shown for the 22 and 17 second time points of the (a) *in vivo* arterial occlusion and (b) muscle contraction scans, respectively, for data processed with no median filter (first column), with median filters of size 35 (second column), 71 (third column), 141 (fourth column), and with no amplitude demodulation (fifth column). The corresponding B-mode images are shown in the last column.

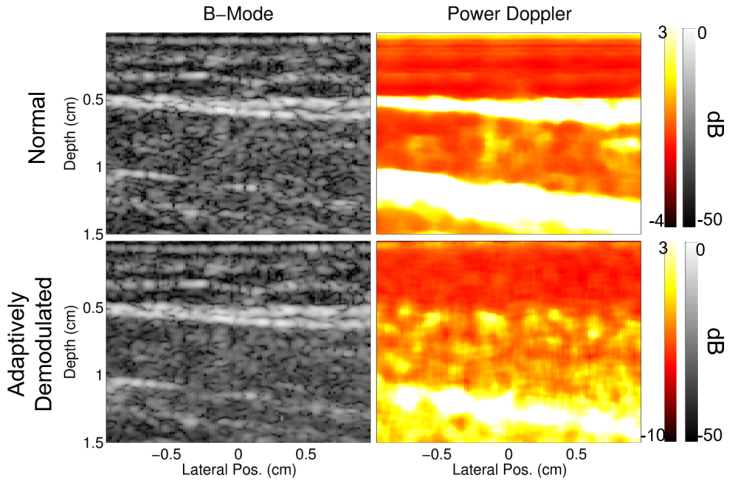

Figure 3.6: B-mode and power Doppler images before and after adaptive demodulation (using a median filter of 35 samples for the amplitude demodulation) are shown for the 22s time point of the *in vivo* occlusion scan.

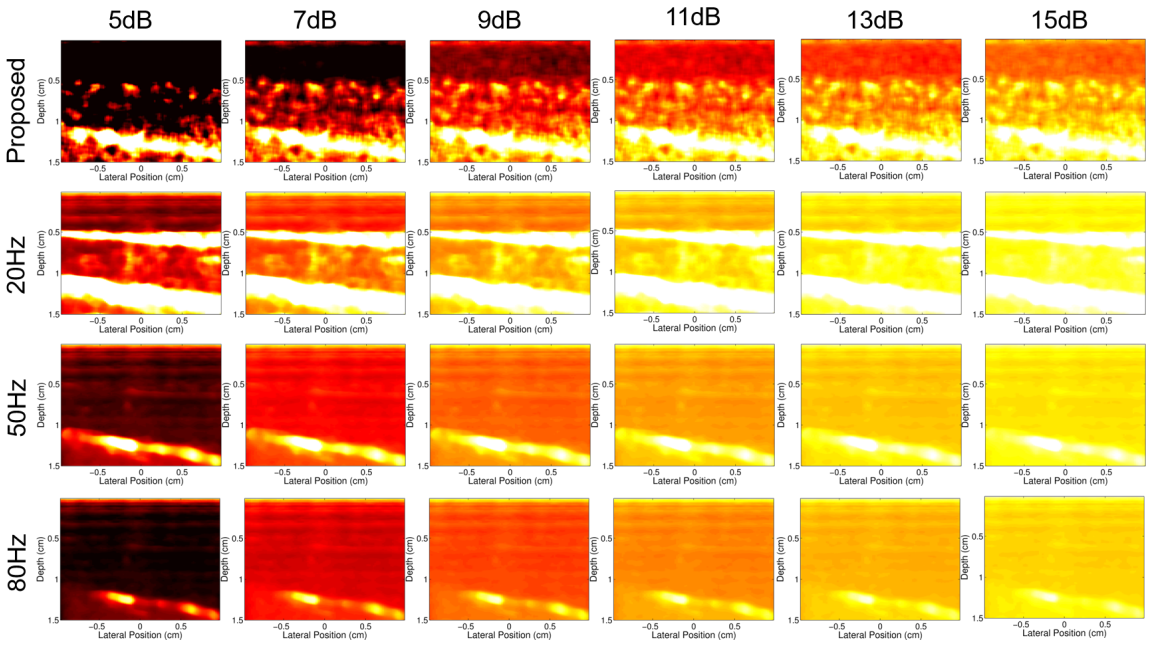

Figure 3.7: Power Doppler images made from the 22s time point of the occlusion scan for the proposed filter (first row) and conventional filter with 20Hz (second row), 50Hz (third row), and 80Hz (bottom row) filter cutoffs. Dynamic ranges between 5 and 15dB are compared. The maximum in all images is 3dB.

seen in Figure 3.8b for 1mm/s and 2mm/s peak velocities, while tissue clutter dominates in Figure 3.8a for the same speeds. The 0.5mm/s adaptively demodulated case is less prominent, but still shows more flow than the normal power Doppler image for that speed.

Figure 3.9 shows normal and adaptively demodulated power Doppler images side-by-side for cutoff values between 0.1 and 5Hz (to detect flow above 0.01 and 0.5mm/s, respectively) and for dynamic ranges between 5 and 15dB. Regardless of clutter filter cutoff or dynamic range, no flow is visible with the conventional method.

3.4 Discussion

The sonographer hand motion bandwidth results demonstrate that adaptive demodulation can isolate slow flow velocities from tissue clutter at relative blood signals at least 60dB lower than the tissue. Others have reported the amplitudes of blood signals as being up to 100dB lower than tissue clutter [15]. For our current system, the signal to noise

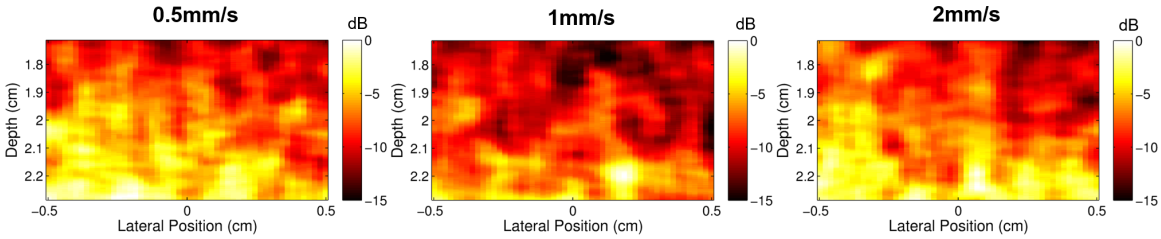

(a)

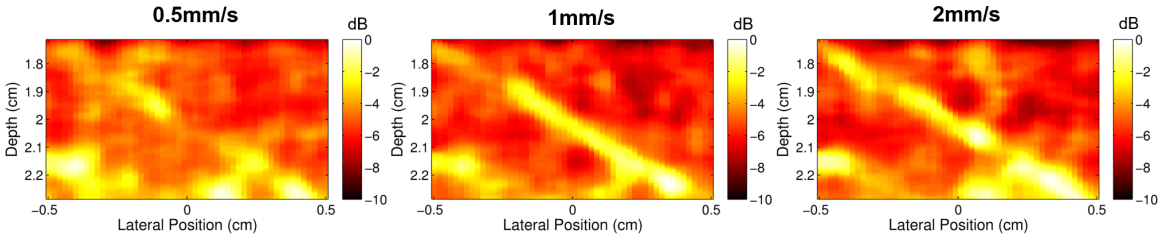

(b)

Figure 3.8: Power Doppler images are shown for 0.5mm/s, 1mm/s, and 2mm/s parabolic blood scatterer velocities for (a) normal and (b) adaptively demodulated simulation data.

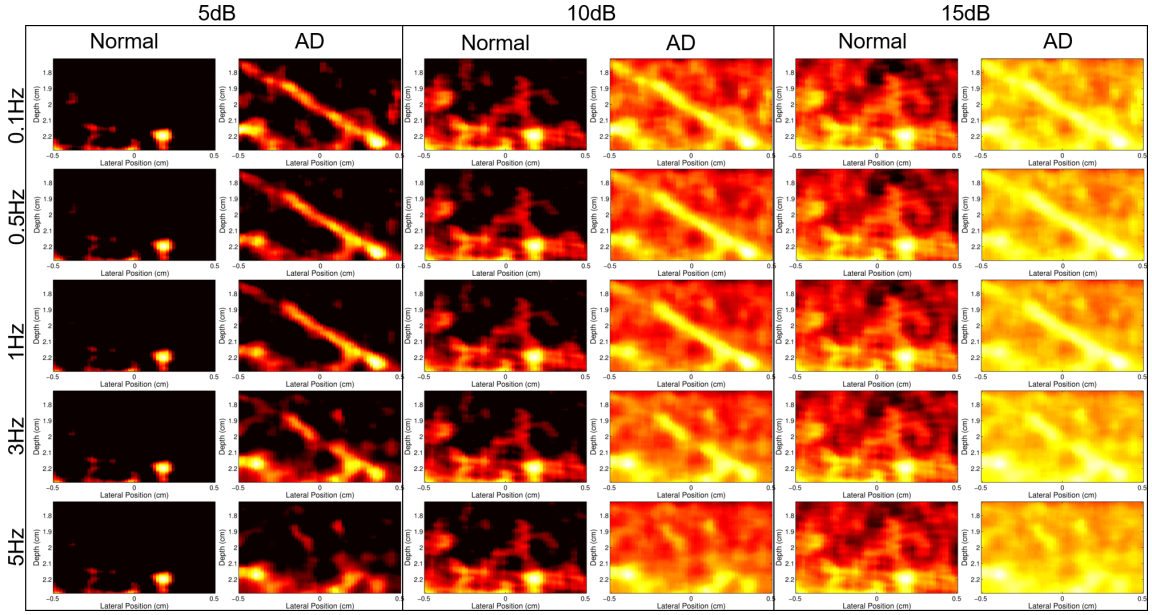

Figure 3.9: Power Doppler images of the 1mm/s peak velocity simulation with and without adaptive demodulation (AD) (left and right in each column, respectively) are shown for dynamic ranges between 5 and 15dB (columns) with filter cutoffs between 0.1Hz and 5Hz (rows).

limit is reached around 80dB below tissue after adaptive demodulation. The PWSF and MPW sequence modifications used for the hand motion studies both improve SNR and lower the noise floor by about 10dB (as seen in Figure 3.1a). However, the MPW case did not result in improved bandwidth suppression at -60dB, and we only saw a minor improvement with the PWSF sequence (as seen in Table 3.2). Since the PWSF sequence also improves resolution and image quality, the improvement seen with PWSF, although small, is not negligible and is likely due to decreased intrinsic spectral broadening resulting from the transmit beam shape. Since the SPW and MPW methods have lower resolution due to unfocused transmit beams, intrinsic spectral broadening will result from geometrical focal broadening during receive beamforming, resulting in larger bandwidths of the tissue clutter [64]. This suggests that intrinsic spectral broadening is a more immediate limitation of the method compared to SNR. Apart from sequence modifications, higher transmit voltage also improves SNR. However, the use of a higher transmit voltage (30.7V) for the hand motion phantom SPW study did not result in a substantially higher SNR value compared to the *in vivo* studies, which used the same acquisition sequence using only half the transmit voltage (16.1V). This is likely due to the the phantom and *in vivo* data being acquired on different media. However, this further suggests that SNR is not a significant direct limitation of the method.

As discussed in Chapter 2, we propose a median filtering of the amplitude demodulation function in an attempt to ensure that tissue signal is the primary contributor to the amplitude modulation estimate. Ideally, the median filter should be long enough to avoid suppression of the blood signal and short enough to allow for maximal tissue clutter suppression. For example, if blood flows outside of a given pixel faster than the acquisition rate (i.e. blood is incoherent between consecutive acquisitions), small median filter sizes would suffice. Although little is known about the coherence length of slow flow, it is plausible that when imaging slow flow, the blood signal will be coherent across a longer time than with fast flow. Therefore, larger filter sizes would be required to ensure the blood signal amplitude

is not demodulated. A median filter of 35 samples was used for the experiments in this paper. Additionally, the effects of increasing the filter size on tissue clutter bandwidth and qualitative power Doppler images were assessed. Future work will aim to confirm optimal, application-specific filter sizes.

Expected reactive and exercise hyperemia behaviors are well characterized, which provided reasonable standards for evaluating our algorithm in applicable clinical settings. Although the *in vivo* results presented in this paper are preliminary, both the arterial occlusion and contraction studies are consistent with previous findings of perfusion and blood-oxygen-level-dependent (BOLD) MRI characteristics under these conditions. For the arterial occlusion study, Lebon et al. and Englund et al. both showed time to peak perfusion times between 15 and 20s after arterial occlusion in the calf muscle, which agrees with the results shown in Figure 3.3a [65, 66]. For the adaptively demodulated data with a 20Hz high pass filter (proposed filter method), the peak blood flow time point occurs at about 22s, which is about 18s after the cuff was released (cuff was released at about 4s), as seen in Figure 3.3a. Similarly for the contraction study, Towse et al. showed that peak BOLD signal intensity occurs between 5-7s post-muscle contraction, which correlates with the results shown in Figure 3.4a [61, 67]. In Figure 3.4a, the proposed filter method resulted in peak power at about 17s which is approximately 5s post-contraction (last contraction time point occurs at about 12s). It is also important to note that the median power Doppler values in both Figures 3.3a and 3.4a are referenced to the last time point for each case. We therefore expected to see power Doppler values below or at least at zero during occlusion and before contraction, assuming there should be increased perfusion post-occlusion and post-contraction, which was not the case. However, results found in the literature show similar trends in perfusion values, with post-occlusion and post-contraction values even decreasing to values below those during occlusion and before contraction after reaching peak perfusion [61, 65, 66].

Although the *in vivo* studies involved changes in blood flow and are supported by sim-

ilar findings in the literature, neither study definitively proved that the proposed technique is able to suppress tissue clutter while also preserving slow flow. The simulation results address this and are consistent with other experiments in the literature for testing slow flow detection [40, 41]. The simulation results confirm that the technique can preserve slow flow in addition to suppressing tissue clutter.

Finally, our results indicate that previous limits on blood flow estimation with ultrasound are not fundamental and are conservative [14]. The true fundamental limit remains an open question.

3.5 Conclusion

Due to spectral broadening caused by patient and sonographer hand motion, conventional Doppler methods are limited to blood flow above 5-10mm/s for clinical imaging frequencies, which eliminates sensitivity to slow flow or perfusion [14]. To address this, we introduced an adaptive clutter demodulation scheme that suppresses the bandwidth of tissue clutter while still preserving signal from slow blood flow. The proposed algorithm was developed and assessed by way of phantom and *in vivo* studies. The approach was shown to successfully reduce hand motion spectrum bandwidths, potentially allowing for the detection of blood velocities well below assumed theoretical limits. Additionally, the proposed filter resulted in a higher dynamic range between the lowest and highest blood flow time points compared to conventional filters for both *in vivo* studies. Furthermore, both *in vivo* studies resulted in peak blood flow time points that supported previous findings. Finally, we confirm that the method can simultaneously suppress tissue clutter and preserve slow flow through controlled simulation experiments.

Chapter 4

Combining Adaptive Clutter Demodulation with Other Perfusion-Focused Advancements

This work was originally published in [68]: Tierney, Jaime, et al. "Combining Slow Flow Techniques with Adaptive Demodulation for Improved Perfusion Ultrasound Imaging without Contrast." *IEEE Transactions on Ultrasonics, Ferroelectrics and Frequency Control* 66.5 (2019): 834-848.

4.1 Introduction

In the previous chapter, we introduced an adaptive phase and amplitude demodulation scheme to reduce the bandwidth of the tissue clutter signal prior to high pass filtering to better enable ultrasound perfusion imaging without contrast agents [54]. We developed and implemented an initial realization of the method using single plane wave power Doppler imaging with conventional high pass filtering on experimental phantom and *in vivo* data. We demonstrated that adaptive demodulation can solve the tissue clutter spectral broadening problem and potentially allow for lower blood velocities ($<$1mm/s) to be detected without contrast [54]. However, our results were mainly proof-of-concept, and we have yet to fully explore the boundaries and limitations of the method. Additionally, apart from the spectral broadening problem, there are several other factors that can limit perfusion visualization.

In our initial implementation of adaptive demodulation, we overcame some of the other limitations associated with slow blood flow imaging, like beam-to-flow angle dependence and short ensemble lengths, by using power Doppler and plane wave imaging. Power Doppler is less angle-dependent and more sensitive to smaller vessels since it measures the amount of blood rather than the true velocity [1, 10], as discussed in Section 1.1.3. There-

fore, because we are focusing on perfusion, or the slowest, most randomly-oriented flow, we use power Doppler. Additionally, we use plane wave imaging to eliminate the trade-off between frame rate and ensemble length, allowing for high frame rate imaging while also maintaining sufficient sampling for tissue filtering [13, 38]. However, limitations still exist with single plane wave imaging and conventional tissue filtering, and recent advancements in both beamforming and tissue clutter removal have been proposed to help solve these additional problems [10, 17, 40, 41, 44].

As discussed in Sections 1.5.2 and 1.5.3, plane wave synthetic focusing and coherent flow power Doppler (CFPD) applied to plane wave synthetic focused data are alternative beamforming methods that can help overcome single plane wave imaging limitations. Single plane wave images suffer from low signal-to-noise ratio and reduced lateral resolution because it only uses a single unfocused transmit event per image. Plane wave synthetic focusing involves transmitting and coherently summing multiple angled plane waves to increase signal-to-noise ratio and synthesize transmit focusing at all locations in the image [39]. Because plane wave synthetic focusing only needs a few angles to regain the resolution of a focused transmit, it maintains the frame rate and ensemble length benefits of single plane wave imaging [10]. CFPD applied to plane wave synthetic focused data intends to further improve signal-to-noise ratio by suppressing non-stationary diffuse reverberation clutter in addition to thermal noise [40, 41]. Although plane wave synthetic focusing and CFPD can improve sensitivity to slow flow, they still rely on effective tissue filtering.

Conventional Doppler tissue filtering, which typically uses infinite or finite impulse response or polynomial regression filters, has been extensively studied and optimized [13, 15, 16]. Two of the main limitations with conventional filters are that they rely on clear temporal spectral separation of tissue and blood, and they are applied only in the slow-time dimension [17]. Adaptive demodulation helps overcome the former. As discussed in Section 1.5.4, singular value decomposition (SVD) methods have been proposed to help overcome both of these limitations, assuming long slow-time ensembles are used [17, 49].

These SVD methods incorporate both temporal and spatial information to better separate tissue from blood, presumably decreasing the reliance on clear temporal spectral separation [17, 49]. However, it has been shown that the frequency content of temporal eigenvectors is still important to consider when using these filters [46, 49].

Here we aim to improve upon our initial implementation of adaptive demodulation by using controlled simple simulation experiments to assess the limitations and boundaries of the method. We also evaluate beamforming and tissue filter improvements with and without adaptive demodulation. Additionally, because adaptive demodulation is a pre-filtering method, CFPD is a beamforming technique, and SVD is a filter, we are able to assess each of these proclaimed slow-flow techniques separately as well as in combination. We test our simulation findings using phantom and *in vivo* data.

4.2 Methods

4.2.1 Simulations

To evaluate the limitations and boundaries of adaptive demodulation as well as improvements in beamforming and tissue filtering, we use a single small vessel simulation experiment. Using Field II [63], we simulated plane wave channel data of a 0.5mm diameter vessel of blood scatterers angled 30° to the beam and centered at a depth of 2cm within a 0.6cm by 1cm area of tissue scatterers (Figure 4.1a). In the following subsections, we describe how tissue motion was implemented and how each adaptive demodulation, beamforming, and tissue filtering parameter was adjusted and evaluated.

Tissue Motion

To simulate realistic tissue motion, we used displacements estimated from sonographer hand motion phantom data to displace both the tissue and blood scatterers. Six volun-

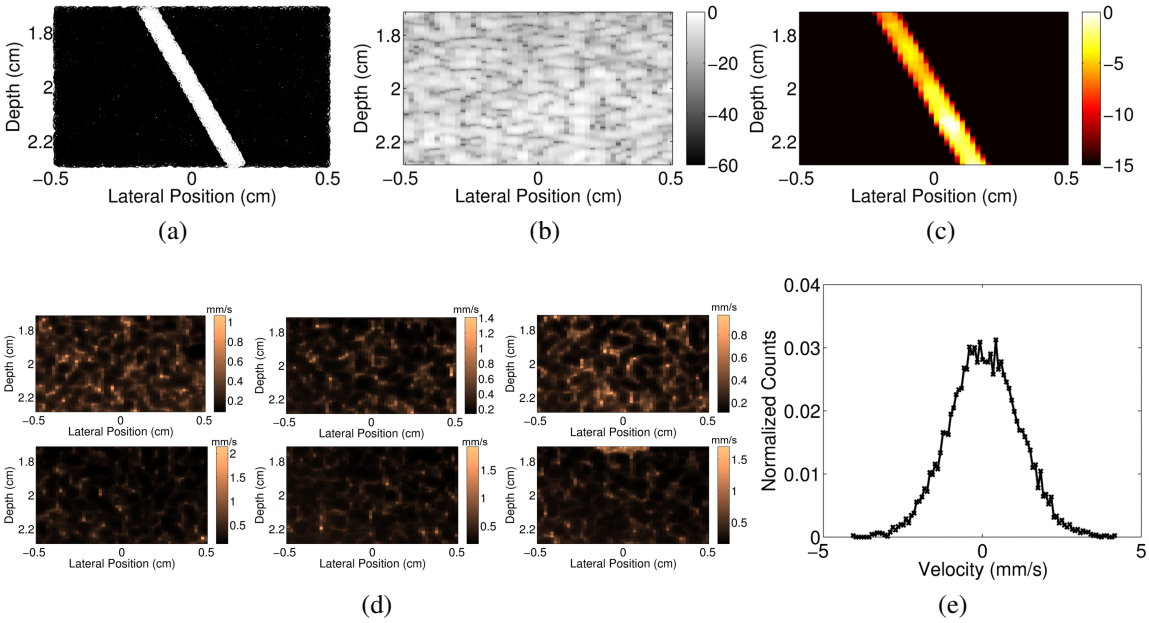

Figure 4.1: (a) Example realization of tissue (black) and blood (white) scatterers used for simulations. (b) Example simulated plane wave synthetic focused B-mode image on a dB scale. (c) Example simulated power Doppler image with no tissue motion on a dB scale. (d) Root mean square of hand motion velocities (mm/s) for each tissue clutter realization. (e) Histogram of velocities for an example pixel from an example tissue clutter realization.

teers acquired 0° plane wave channel data of a stationary quality assurance phantom (CIRS Model 040GSE, Norfolk, VA) using a 7.8125MHz center frequency at a pulse repetition frequency of 9kHz for 3s using a Verasonics Vantage System (Verasonics, Inc., Kirkland, WA) and L12-5 probe. A Hann apodization and aperture growth to achieve an F/# of 2 were implemented during receive beamforming. Beamformed data were band-pass filtered and up-sampled by a factor of 2 to achieve a sampling frequency of 62.5MHz. Total displacements over the first second of data were computed using the same method described in Section 2.3 using an axial kernel size of 1.25λ and a lag of 1ms for the relative displacement estimator. Total displacements were interpolated according to the location of the tissue and blood scatterers and used to generate 6 realistic tissue clutter realizations. Root mean square of hand motion velocities through slow-time are shown for each realization in Figure 4.1d. Velocities were computed on the hand motion data sets using a slow-time

lag of 8ms and a kernel size of 1.25λ. Figure 4.1e shows a histogram of velocities for an example pixel from an example realization.

Parameter Study

For each realization, we simulated 1s of channel data using 9 transmit angles evenly spaced between -8° and 8° at a pulse repetition frequency of 9kHz using a 1 cycle pulse. We simulated tissue and blood channel data separately. We varied transmit frequency, blood-to-noise channel signal ratio, tissue-to-blood channel signal ratio, peak blood scatterer velocity, beamforming methods, tissue filter methods, and also displacement estimation parameters used for adaptive demodulation. The adaptive demodulation displacement estimation parameters are axial kernel size and slow-time lag. The kernel size defines the window size used for axial averaging in the 2D autocorrelation relative displacement estimator. For a given kernel, relative displacements are computed between slow-time samples that are up to a maximum lag apart. A summary of all parameters is shown in Table 4.1. We used a fixed sampling frequency of 31.25MHz. We band-pass filtered and up-sampled all data to 62.5MHz after beamforming. We band-pass filtered all data again after applying adaptive demodulation.

Baseline Parameters

When varying each parameter, we used the same baseline values for all other parameters. Our baseline case used a 7.8125MHz transmit frequency and the full ensemble (1s). We scaled the blood channel data to be 40dB lower than tissue and added noise 0dB relative to the blood. Blood scatterers moved laminarly with a peak velocity of 1mm/s. We beamformed the data using the plane wave synthetic focusing method (resulting in a frame rate of 1kHz and 1s ensemble) and filtered tissue using a conventional 1Hz ($\approx$0.1mm/s) high-

Table 4.1: Simulation Experiment Parameter Summary. Baseline parameters are in bold font. AD, SPW, PWSF, and IIR stand for adaptive demodulation, single plane wave, plane wave synthetic focusing, and infinite impulse response, respectively.

Parameter	Values/Methods
AD Kernel Size (wavelengths)	1.25, 2.5, 5, **10**, 15
AD Lag (ms)	**1**, 3, 5, 7
Blood-to-Noise Ratio (dB)	-30, -20, -10, **0**, 10, 20
Tissue-to-Blood Ratio (dB)	10, 20, 30, **40**, 50, 60
Peak Blood Velocity (mm/s)	0.5, **1**, 2, 5, 10
Imaging Frequency (MHz)	2, 4, 6, **7.8125**, 10
Beamforming Method	SPW, **PWSF**, CFPD
Tissue Filtering Method	**IIR**, SVD

pass infinite impulse response (IIR) filter. We performed adaptive demodulation using a kernel size of 10λ for our axial displacement estimator. However, when varying imaging frequencies, we adjusted the kernel size to ensure the same number of samples was used for each case. We used a single 1ms lag to compute total displacements, which is equivalent to performing a cumulative sum of the relative displacements through slow-time. For all simulations, we did not incorporate any amplitude demodulation because we controlled the experiment to only have axial tissue motion. Baseline parameter values are bold font in Table 4.1.

Beamforming and Tissue Filtering

We used the same channel data for all three beamforming methods. For the single plane wave case, we used only the 0° plane wave channel data and parallel receive beamforming [38]. For the plane wave synthetic focusing case, we used all 9 angles and summed consecutive angled beamformed plane wave data [39]. For the CFPD case, we applied short-lag spatial coherence (SLSC) beamforming to filtered plane wave synthetic focused data using a max aperture lag of 20 and a kernel size of 1.5λ, as in Li et. al. [41]. For all cases, we used a Hann apodization and aperture growth to achieve an F/# of 2 during receive beam-

forming. For the CFPD case, we up-sampled and band-pass filtered the delayed channel data.

We used two different tissue filtering methods for this study: a conventional IIR filter and an SVD filter [17, 49]. A conventional 6th order type 1 Chebyshev IIR high-pass filter with a 1Hz cutoff was used. The cutoff was adjusted only for the peak blood scatterer velocity study. For all peak velocities, ranges of cutoffs were tested on the full 1s ensemble for a single realization, and an optimal cutoff was chosen based on the highest blood-to-background signal-to-noise ratio (see Equation 4.2). A 1Hz cutoff was used for the 0.5mm/s and 1mm/s normal and adaptively demodulated cases. A 10Hz cutoff was used for the 2mm/s normal and adaptively demodulated cases. 30Hz and 20Hz cutoffs were used for the 5mm/s normal and adaptively demodulated cases, respectively. 55Hz and 50Hz cutoffs were used for the 10mm/s normal and adaptively demodulated cases, respectively. For the SVD filter, tissue and noise eigenvalue cutoffs were chosen adaptively, as in Song et al. [49]. This process is summarized in Figure 4.2 and involves thresholding the singular value magnitude and temporal eigenvector mean Doppler frequency curves to select tissue and noise cutoffs. Thresholds were tested and chosen separately for data with and without adaptive demodulation based on which produced the closest to optimal SNR (see Equation 4.2). For tissue cutoff selection, two pre-cutoffs are chosen [49], as depicted in Figures 4.2a and 4.2b. In the method by Song et al., the maximum of these two cutoffs is used as the final tissue cutoff [49]. We looked at both the maximum and minimum and, based on highest blood-to-background SNR (see Equation 4.2), used the minimum for data with adaptive demodulation. For CFPD data, tissue filtering was performed on delayed channel data and all channels were included as spatial information for the SVD filter. Thresholds for choosing tissue cutoff 1, tissue cutoff 2, and the noise cutoff are respectively based on the slope of the singular value magnitude curve, mean Doppler frequency, and deviation of a linear fit to the singular value magnitude curve at the highest singular value orders. For all data without adaptive demodulation, thresholds of 5, 1Hz, and 0.05 were used for selecting

tissue cutoff 1, tissue cutoff 2, and the noise cutoff, respectively. For all data with adaptive demodulation, thresholds of 1.5, 0.5Hz, and 0.05 were used for selecting tissue cutoff 1, tissue cutoff 2, and the noise cutoff, respectively.

For the beamforming and filtering parameter studies, we also varied the ensemble size that we use for high-pass filtering and power Doppler estimation. For these studies, we looked at ensemble sizes of 20ms-1s (20-1000 samples).

Additionally, for both filtering techniques, we performed a more extensive tissue cutoff analysis on the 1mm/s peak velocity baseline and adaptively demodulated data. For the IIR filter, we tested a range of cutoffs between 0.5 and 25Hz (spaced by 1Hz from 1 up to 10Hz then spaced by 5Hz up to 25Hz) for ensemble sizes between 20ms and 1s for each realization. For the SVD filter, we tested tissue eigenvalue cutoffs between 1 and 20 for ensemble sizes between 20ms and 1s for each realization. For the SVD cutoff analysis, we did not incorporate any noise filtering.

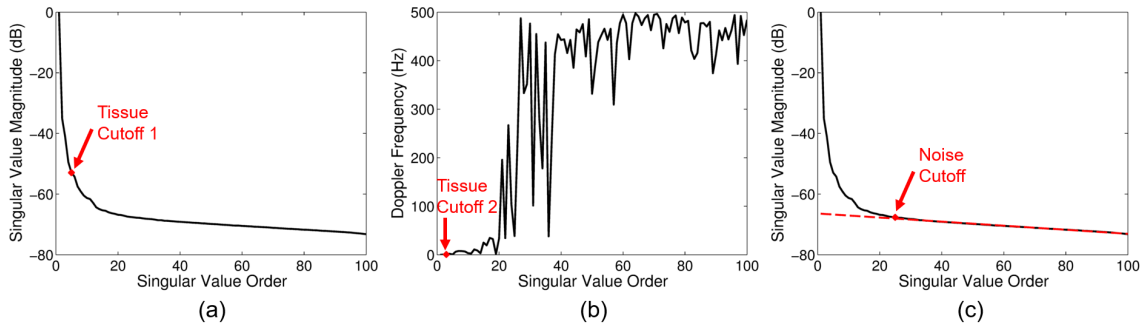

Figure 4.2: Example tissue and noise eigenvalue cutoff selection. (a) Tissue cutoff 1 is selected by finding when the slope of the singular value magnitude curve goes below a certain threshold (e.g., 5). (b) Tissue cutoff 2 is selected by finding the first temporal eigenvector mean Doppler frequency to go above a certain threshold (e.g., 1Hz). (c) The noise cutoff is selected by fitting a line to the singular value magnitude curve and finding when the curve starts to deviate from the line by more than a certain threshold (e.g. 0.05).

Qualitative and Quantitative Metrics

The power Doppler signal was computed using

$$PD(x,z) = \sum_{t=1}^{T} s(x,z,t)^2 \tag{4.1}$$

where $s(x,z,t)$ is the filtered SLSC signal for the CFPD cases and the magnitude of the filtered analytic signal for all other cases, x,z,t are the spatial, axial, and temporal dimensions, and T is the total number of slow-time samples or ensemble size. A 1mm by 1mm spatial median filter was applied to each power Doppler image. To quantify differences between different parameter values and techniques, we used blood-to-background signal-to-noise ratio (SNR), contrast-to-noise ratio (CNR), and generalized contrast-to-noise ratio (GCNR) metrics from Li et al. [41], Baranger et al. [69], and Molares et al. [70], respectively,

$$SNR = 10log_{10}\frac{\sqrt{\frac{1}{N}\sum_{i=1}^{N} PD_{sig}^2(i)}}{\sqrt{\frac{1}{M}\sum_{i=1}^{M} PD_{bkgd}^2(i)}} \tag{4.2}$$

$$CNR = 10log_{10}\frac{|\frac{1}{N}\sum_{i=1}^{N} PD_{sig}(i) - \frac{1}{M}\sum_{i=1}^{M} PD_{bkgd}(i)|}{STD(\frac{1}{M}\sum_{i=1}^{M} PD_{bkgd}(i))} \tag{4.3}$$

$$GCNR = 1 - OVL \tag{4.4}$$

where N and M are the total number of pixels in the vessel and background, respectively, PD_{sig} and PD_{bkgd} are the power Doppler values in the vessel and background, respectively, STD stands for the standard deviation, and OVL represents the overlap between histograms of the background and vessel pixels. The vessel mask was interpolated as necessary for the varying center frequency study to account for changes in resolution. Power Doppler images were made by log compressing Equation 4.1 ($I = 10log_{10}PD(x,z)$). Images were scaled to individual maximums and dynamic ranges were chosen separately for each beamformer and filter combination by computing the average power value of the background pixels of the adaptively demodulated data for that beamformer and filter. This value was used as the minimum value in the image for both data with and without adaptive demodulation. Exam-

ple B-mode and power Doppler images are shown in Figures 4.1b and 4.1c, respectively, for a case with no tissue motion.

4.2.2 Phantom Experiment

Polyvinyl alcohol (PVA) and graphite phantoms with a single small diameter vessel were used to further evaluate improvements in beamforming and tissue filtering with and without adaptive demodulation. Phantoms were made by placing 0.60-0.64mm diameter wires through the short ends of 2 by 3cm molds. A PVA and graphite mixture [71] was then poured into the molds, and then the molds were placed in the freezer for several days.

After thawing for a few hours and removing the molds and wire, a syringe pump was used to flow blood-mimicking fluid (CIRS Model 046, Norfolk, VA) through the vessel of each phantom at flow rates of 95μl/min (90 for 0.60mm diameter vessel) and 17μl/min, which equates to average velocities of about 5 and 1mm/s. For each flow speed, 6 different phantoms were used to ensure 6 different speckle realizations. For each phantom, a volunteer sonographer acquired 1s of plane wave channel data using the same Verasonics L12-5 probe used for the sonographer hand motion realizations described in Section 4.2.1. Channel data were acquired using a 7.8125MHz center frequency, 9 transmit angles evenly spaced between -8° and 8°, a pulse repetition frequency of 9kHz and a 1 cycle pulse length.

Channel data were beamformed using both the plane wave synthetic focusing and CFPD methods with the same receive beamforming parameters described in Section 4.2.1. Beamformed data were band-pass filtered and up-sampled to a sampling frequency of 62.5MHz. Adaptive demodulation was performed using the same baseline settings as in Section 4.2.1. Although lateral motion was likely present in this experiment, amplitude demodulation was not used in order to maintain consistency with the simulations. Data were band-pass filtered again after adaptive demodulation. The same IIR and adaptive SVD filters were used as described in Section 4.2.1, except that a 25Hz cutoff was used for the IIR filter for the faster flow case, and the thresholds were adjusted for the adaptive SVD

filter for both cases. For the faster flow case, for data without adaptive demodulation, tissue cutoffs 1, 2, and the noise cutoff were selected using thresholds of 2, 8Hz, and 0.01, respectively. For data with adaptive demodulation, tissue cutoffs 1, 2, and the noise cutoff were selected using thresholds of 0.5, 10Hz, and 0.01, respectively. For the slower flow case, for data without adaptive demodulation, tissue cutoffs 1, 2, and the noise cutoff were selected using thresholds of 2, 1Hz, and 0.01, respectively. For data with adaptive demodulation, tissue cutoffs 1, 2, and the noise cutoff were selected using thresholds of 2.5, 1.5Hz, and 0.01, respectively. Similar to the simulation experiment, the maximum tissue cutoff was used for data without adaptive demodulation, while the minimum was used for data with adaptive demodulation.

For this experiment, we considered our baseline case to be the plane wave synthetic focusing beamforming method with the conventional IIR filter and without adaptive demodulation. Adaptive demodulation, SVD, and CFPD were then evaluated separately as well as in combination. Power Doppler was computed and images were formed the same way as in Section 4.2.1. As was done for simulations, dynamic ranges were computed adaptively for each beamformer and filter combination by using the average power of the background of the adaptively demodulated data as the minimum value in the images with and without adaptive demodulation. Blood-to-background SNR, CNR, and GCNR (Equations 4.2, 4.3, and 4.4, respectively) were computed for ensemble sizes between 20ms and 1s, as was done for the simulations.

4.2.3 *In Vivo* Experiment

To demonstrate *in vivo* feasibility, we tested all combinations of adaptive demodulation, CFPD, and SVD on data acquired from a patient receiving trans-arterial chemoembolization (TACE). TACE is a minimally invasive treatment for intermediate stage liver lesions that do not qualify for curative resection or transplant [26]. TACE works by delivering high doses of chemotherapy as well as embolizing agents to simultaneously treat a tumor

and occlude its arterial supply [25]. Therefore, because these tumors are highly vascularized compared to the surrounding healthy liver tissue, we expect to see increased power or perfusion in a tumor before TACE and suppressed or no power in a tumor after TACE.

The patient gave informed written consent in accordance with Vanderbilt's Institutional Review Board prior to the start of the study. Using a Verasonics C5-2 probe, we acquired 2s of angled plane wave channel data (9 angles spaced evenly between -8° and 8°) immediately before and after TACE. The channel data were acquired using a 1 cycle pulse at a pulse repetition frequency of 5.4kHz (600Hz frame rate after beamforming) and an imaging frequency of 4.2MHz. Channel data were acquired at a sampling frequency of 16.7MHz, and all beamformed data were up-sampled by a factor of 3 to achieve a sampling frequency of 50MHz. For anatomical reference, immediately prior to the acquisition of each plane wave scan, a conventional focused scan was acquired at 6cm. SLSC beamforming was performed on the focused data using a maximum lag of 10 and a kernel size of 1.5 wavelengths [42].

Using the same plane wave synthetic focusing and CFPD methods and the same receive beamforming parameters described in Section 4.2.1, 0.5s ensembles of channel data before and after TACE were beamformed. Adaptive demodulation was performed using the same baseline settings as in Section 4.2.1. The same IIR filter described in Section 4.2.1 was used except with a 30Hz cutoff. SVD was applied using the same adaptive SVD approach with adjusted thresholds that was used for the simulation and phantom experiments. Thresholds of 0.25, 10Hz, and 0.0005 were used for selecting tissue cutoffs 1 and 2 and the noise cutoff, respectively. The same thresholds were used for data with and without adaptive demodulation.

Power Doppler was computed and images were formed the same way as in Section 4.2.1, except that a 2mm by 2mm spatial median filter was applied to each image (instead of 1mm by 1mm). Displayed images were scaled to individual maximums. Dynamic ranges were chosen to achieve qualitatively similar noise floors. To quantify differences

between techniques and time points, a tumor-to-background contrast metric was computed as follows,

$$C = 10log_{10}\frac{\frac{1}{N}\sum_{i=1}^{N} PD_{tumor}(i)}{\frac{1}{M}\sum_{i=1}^{M} PD_{bkgd}(i)} \tag{4.5}$$

where N and M are the total number of pixels in the tumor and background, respectively, and PD_{tumor} and PD_{bkgd} are the power Doppler values in the tumor and background, respectively. GCNR was also computed as in Equation 4.4, where OVL represents the overlap between histograms of the power Doppler values in the tumor and background.

Gold-standard contrast-enhanced computed tomography (CT) was also acquired before and 2 months after TACE. Before TACE, we expect to see tumor enhancement. After TACE, assuming successful treatment, we expect to see lipiodol uptake with no enhancement. Lipiodol is a carrier substance for the chemotherapy that is selectively retained in tumors and enhances CT images separate from the contrast agents used for enhancing blood flow in follow-up imaging [72]. Therefore, bright lipiodol enhancement in the tumor in follow-up imaging indicates successful retention of the chemotherapy [30].

4.3 Results

4.3.1 Simulations

Figure 4.3 shows blood-to-background SNR for the parameters listed in Table 4.1 (except for beamforming and tissue filtering). The kernel size of the relative displacement estimator and the lag used for computing total displacements have minimal effect on SNR (Figures 4.3a and 4.3b). The blood-to-noise ratio result shown in Figure 4.3c suggests that adaptive demodulation becomes less effective if blood is more than 20dB lower than noise (i.e., overall SNR is less than 20dB). Figure 4.3d shows that adaptive demodulation is most effective when the tissue-to-blood ratio is between 20 and 50dB. Adaptive demodulation is most effective and necessary for velocities below 5mm/s, as shown in Figure 4.3e. Finally, Figure 4.3f shows that with adaptive demodulation, SNRs increase slightly with increas-

ing imaging frequency. Without adaptive demodulation, SNRs remain fairly constant with increasing imaging frequencies.

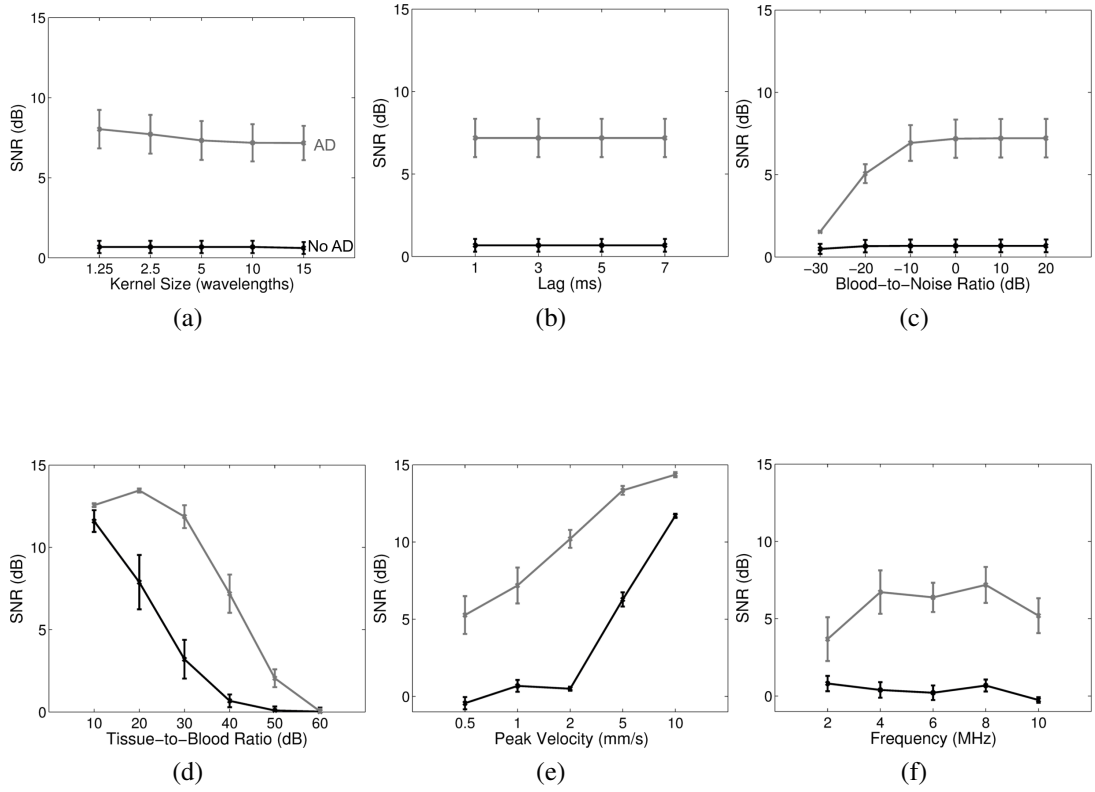

Figure 4.3: Simulated blood-to-background SNR ($\pm$ standard error) for (a) varying adaptive demodulation (AD) kernel sizes, (b) AD slow-time lag, (c) blood-to-noise ratio, (d) tissue-to-blood ratio, (e) peak blood velocity, and (f) imaging frequency. SNRs with and without AD are shown in gray and black, respectively. Plane wave synthetic focusing and IIR filtering were used for each case.

Figure 4.4 compares single plane wave, plane wave synthetic focusing, and CFPD beamforming methods with and without adaptive demodulation. A 1Hz IIR cutoff was used for tissue filtering. Figures 4.4a and 4.4b show that CNR and GCNR increase with adaptive demodulation for all ensembles for all three methods. Adaptive demodulation with CFPD produces the highest CNRs for all ensembles and shows a peak between 100 and 200ms ensembles. Without adaptive demodulation, CFPD produces the highest CNRs and GCNRs compared to plane wave synthetic focusing and single plane wave beamform-

ing. Figure 4.4c supports these results qualitatively and shows power Doppler images for an example tissue motion realization for the 400ms ensemble for each beamforming method with and without adaptive demodulation. For the cases without adaptive demodulation, the images are primarily dominated by tissue clutter, but the vessel can be seen in the CFPD case. With adaptive demodulation, the vessel can be seen in all three cases, but the tissue clutter and noise are suppressed the best with the combination of adaptive demodulation and CFPD.

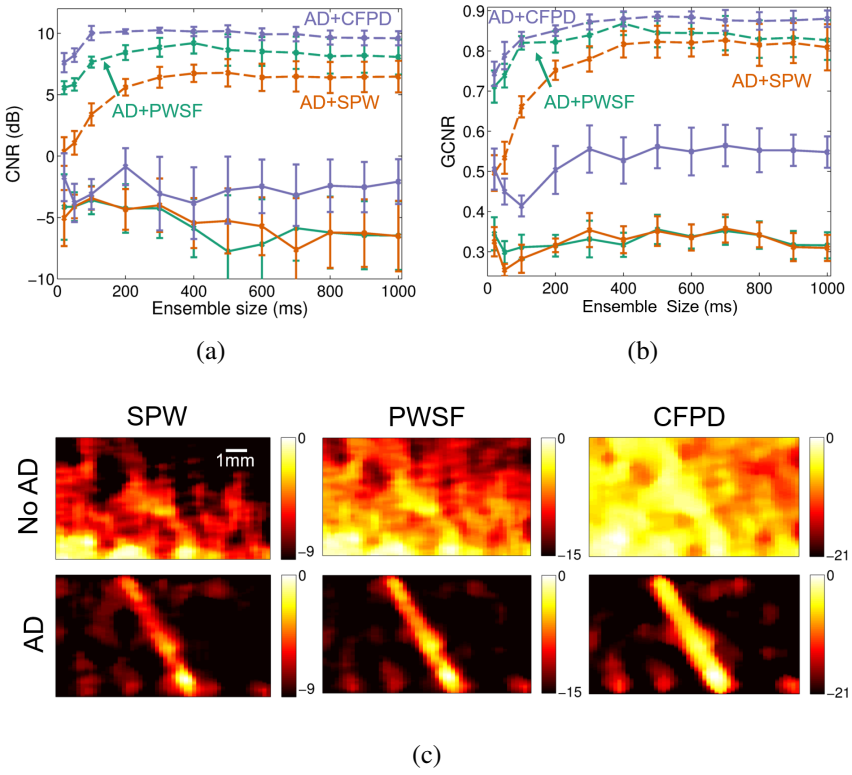

Figure 4.4: Simulated (a) CNR and (b) GCNR (± standard error) vs. ensemble size are plotted for single plane wave (SPW) (orange), plane wave synthetic focusing (PWSF) (teal), and CFPD (purple) beamforming methods with adaptive demodulation (AD) (dotted) and without (solid). (c) Simulated power Doppler images for an example tissue motion realization are shown for SPW (left), PWSF (middle), and CFPD (right) beamforming methods with AD (bottom) and without (top) for the 400ms ensemble. Images are on a dB scale.

Figure 4.5 compares conventional IIR (with a 1Hz cutoff) and adaptive SVD filtering methods with and without adaptive demodulation. Figures 4.5a and 4.5b show that adaptive

demodulation increases blood-to-background SNR and CNR for all ensembles for the IIR filter. With SVD filtering, adaptive demodulation improves SNR and CNR for ensembles below 500ms. For ensembles below 500ms, adaptive demodulation with SVD produces the highest SNRs. Figure 4.5c supports these results qualitatively and shows power Doppler images for an example tissue motion realization for the 400ms ensemble for each filtering method with and without adaptive demodulation. Without adaptive demodulation, the IIR image is dominated by tissue clutter, but the vessel is seen clearly with SVD by itself. With adaptive demodulation, the vessel can be seen in both cases, but the background noise and tissue clutter are suppressed the best in the image with adaptive demodulation and SVD.

Figure 4.6 summarizes the IIR filter cutoff selection analysis. Figure 4.6a shows the average (across realizations) optimal cutoff to produce maximum CNR for each ensemble size for baseline and adaptively demodulated data. Based on this plot, a 1Hz cutoff is not the exact optimal cutoff on average for baseline or adaptively demodulated data for most ensemble sizes. However, the optimal cutoff for all cases is below 5Hz. Figure 4.6b shows how using a 1Hz cutoff for all realizations and ensemble sizes produces fairly similar CNR to the optimized cases. These observations are supported qualitatively in Figure 4.6c, which shows power Doppler images for an example realization using a 400ms ensemble for different cutoffs for baseline and adaptively demodulated data. Regardless of cutoff, the vessel cannot be seen in the baseline case. A 1Hz cutoff suppresses background noise better than a 0.5 or 5Hz cutoff for the adaptively demodulated case. Also, as expected with a peak velocity of 1mm/s (10Hz), flow cannot be seen when using a 10Hz cutoff in either case.

Figure 4.7 summarizes the SVD tissue filter cutoff selection analysis. Figure 4.7a shows the average (across realizations) optimal tissue cutoff to produce maximum CNR for each ensemble size for baseline and adaptively demodulated data. Based on this plot, we are not able to reproduce the exact optimal average tissue cutoff for baseline or adaptively demodulated data using the adaptive cutoff selection technique. However, Figure 4.7b shows how

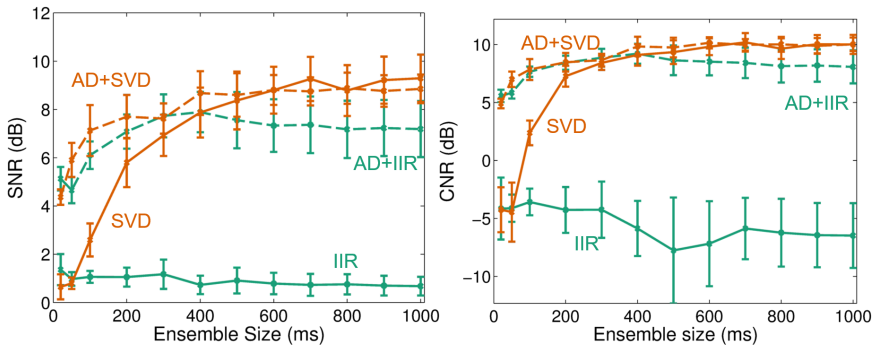

(a) (b)

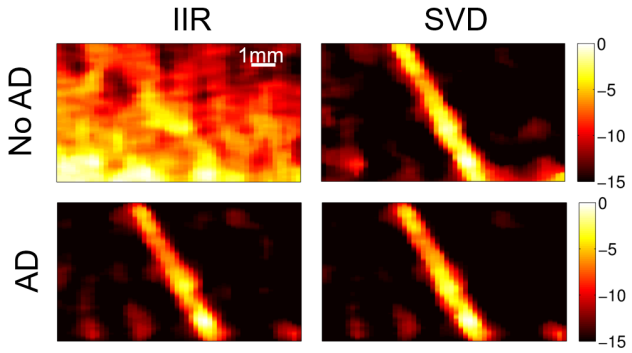

(c)

Figure 4.5: Simulated blood-to-background (a) SNR and (b) CNR (± standard error) vs. ensemble size is plotted for IIR (teal) and SVD (orange) filtering methods with adaptive demodulation (AD) (dotted) and without (solid). (c) Simulated power Doppler images for an example tissue motion realization are shown for IIR (left) and SVD (right) filtering methods with AD (bottom) and without (top) for the 400ms ensemble. Images are on a dB scale.

using the adaptive method for all realizations and ensemble sizes produces very similar CNR to the optimized cases and preserves the overall trends of the optimal curves. These findings are supported qualitatively in Figure 4.7c, which shows power Doppler images for a range of tissue eigenvalue cutoffs for an example realization using a 400ms ensemble. For this example, the optimal tissue eigenvalue cutoffs are 3 and 2 for the baseline and adaptively demodulated data, respectively. The adaptively chosen cutoffs are 4 and 2. Although the adaptive cutoff selection is an eigenvalue off for the baseline case, the resulting power Doppler images are fairly comparable. Also, the optimal adaptively demodulated

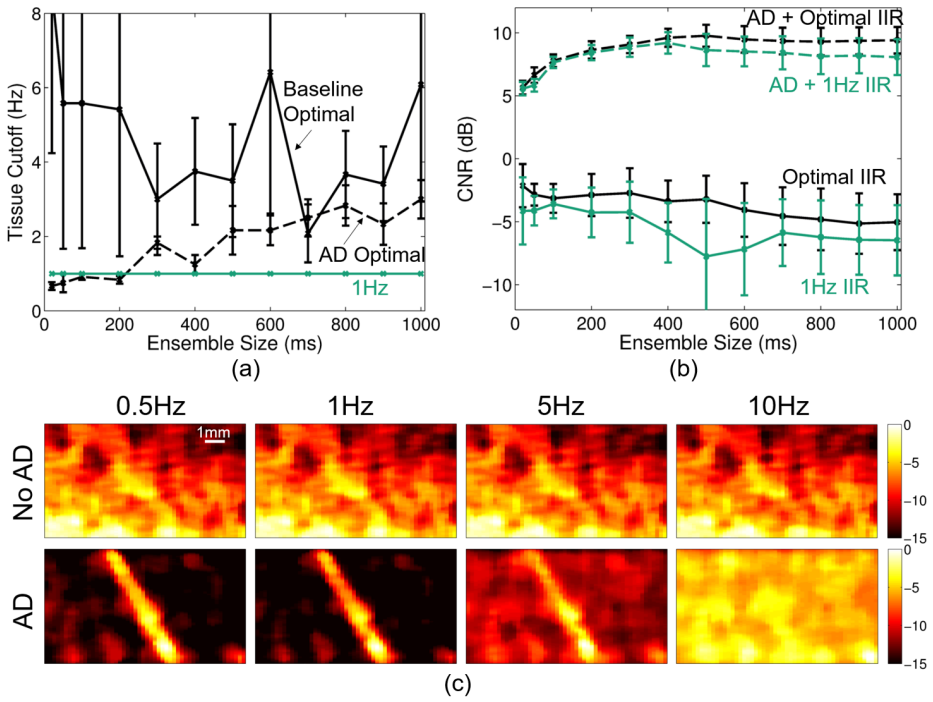

Figure 4.6: (a) Average optimal IIR cutoff ($\pm$ standard error) (black) vs. ensemble size for baseline (solid) and adaptively demodulated (AD) data (dashed). 1Hz cutoff is shown in teal. (b) Average CNR ($\pm$ standard error) obtained with optimal cutoff (black) and with a 1Hz cutoff (teal) vs. ensemble size for baseline (solid) and AD (dashed). (c) Baseline (top) and AD (bottom) power Doppler images for a single realization made using a 400ms ensemble size and conventional high-pass IIR filter with the following cutoffs (imaged from left to right): 0.5, 1, 5, and 10Hz. Images are on a dB scale.

case suppresses background noise better than the optimal baseline case. For both cases, the vessel is clearly seen within 1-2 eigenvalues away from the optimal cutoff, but tissue clutter and noise strongly interfere when a larger eigenvalue of 8 is used.

Adaptive demodulation, CFPD, and SVD have all been proposed as potential methods for improving slow blood flow imaging with ultrasound [17, 40, 54]. Because adaptive demodulation is a pre-filtering method, CFPD is a beamforming method, and SVD is a filtering method, they can be used separately or in combination. Figure 4.8a compares simulated blood-to-background SNR and CNR for varying ensemble sizes for each proclaimed slow flow method separately as well as for each combination of the methods (adaptive demodulation with CFPD, adaptive demodulation with SVD, CFPD+SVD, adap-

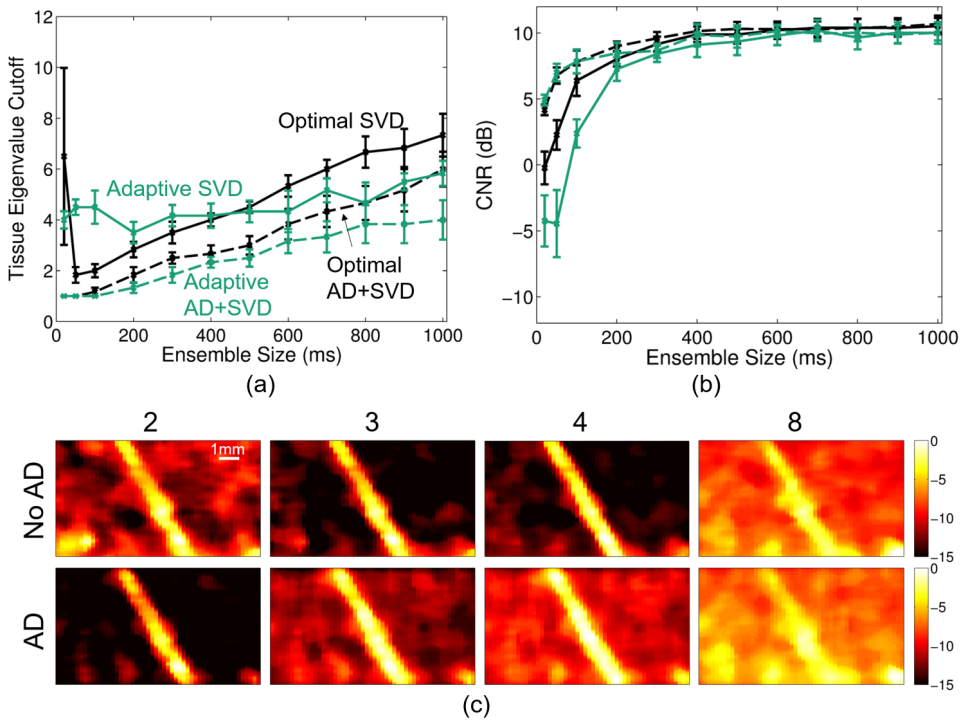

Figure 4.7: (a) Optimal (black) and adaptive (teal) SVD average tissue cutoff ($\pm$ standard error) vs. ensemble size for baseline (solid) and adaptively demodulated (AD) data (dashed). (b) Average CNR ($\pm$ standard error) obtained with optimal (black) and adaptively selected (teal) cutoffs vs. ensemble size for baseline (solid) and AD data (dashed). (c) Baseline (top) and AD (bottom) power Doppler images for a single realization made using a 400ms ensemble size and SVD filter (without noise filtering) with the following tissue eigenvalue cutoffs (imaged from left to right): 2, 3, 4, and 8. Images are on a dB scale.

tive demodulation with CFPD+SVD). Adaptive demodulation in combination with CFPD with a 100ms ensemble produced the highest SNR and CNR overall while CFPD+SVD produced the highest GCNR overall. For smaller ensemble sizes (below 200ms), combinations with adaptive demodulation produced the highest SNRs, CNRs, and GCNRs, while combinations with SVD perform similarly to those with adaptive demodulation for larger ensembles.

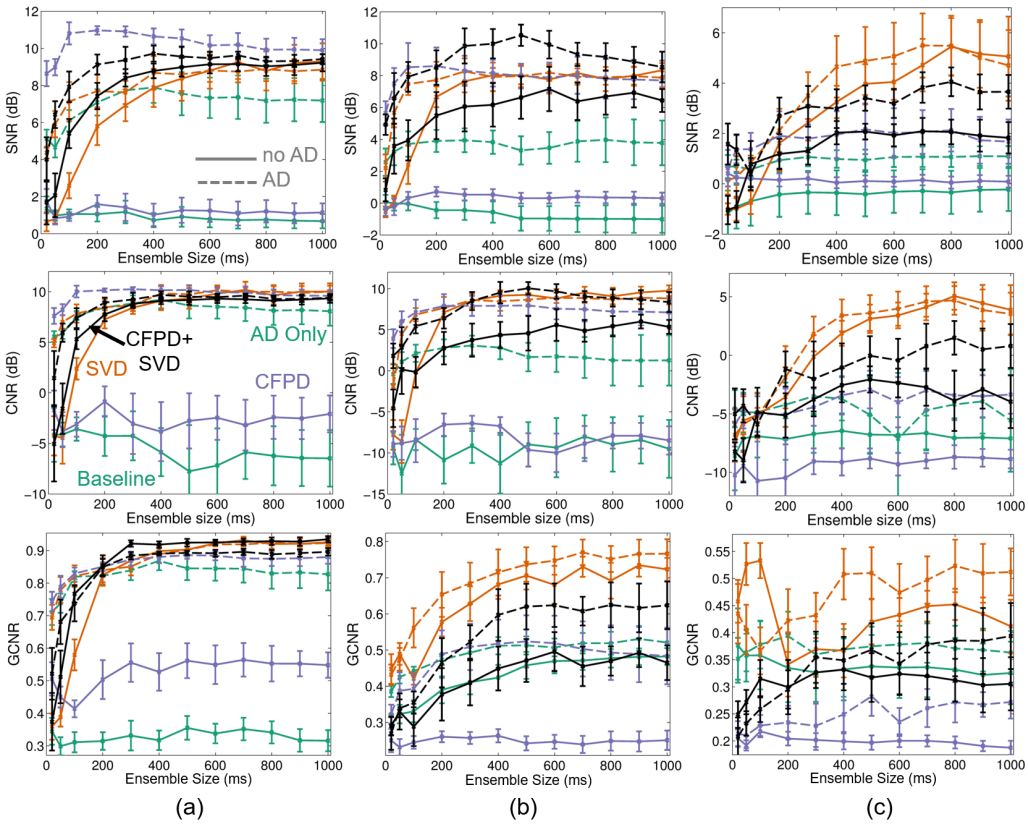

Figure 4.8: Blood-to-background SNR (top), CNR (middle), and GCNR (bottom) ($\pm$ standard error) vs. ensemble size is plotted for baseline (teal), SVD (orange), CFPD (purple), and CFPD+SVD (black) with adaptive demodulation (AD) (dotted) and without (solid) for (a) 1mm/s simulations (b) 5mm/s phantom and (c) 1mm/s phantom. Baseline is plane wave synthetic focusing beamforming with a conventional IIR filter and no AD. AD was applied for all cases using a 10λ kernel size and 1ms slow-time lag. Simulated data had a blood-to-noise ratio of 0dB and a tissue-to-blood ratio of 40dB. For both simulations and phantoms, a 7.8125MHz transmit frequency was used.

4.3.2 Phantom

Figure 4.8b shows the same information as Figure 4.8a for the 5mm/s average velocity single vessel phantom data. The overall SNR and CNR trends and values match fairly well to those observed in simulations. Similar to simulations, adaptive demodulation with CFPD results in a peak SNR and CNR around 100ms. However, the highest overall SNR and CNR was produced using adaptive demodulation with CFPD+SVD. For the smallest ensemble sizes (below 200ms), combinations with adaptive demodulation produced the

highest SNRs and CNRs, while SVD by itself performs similarly to methods with adaptive demodulation for larger ensembles. GCNR shows different trends than SNR and CNR. SVD with and without adaptive demodulation produces the most separation between blood and background, while CFPD by itself produces the most overlap.

Figure 4.9 supports the results in Figure 4.8b qualitatively and shows power Doppler images for an example case for the 400ms ensemble for all combinations of adaptive demodulation, CFPD, and SVD. Figure 4.9a shows the B-mode and no filter power Doppler images for reference. Adaptive demodulation with CFPD suppresses the background noise the best and resulted in the highest CNR, but adaptive demodulation with CFPD and SVD shows the most uniform flow through the vessel. However, adaptive demodulation with SVD resulted in the highest GCNR.

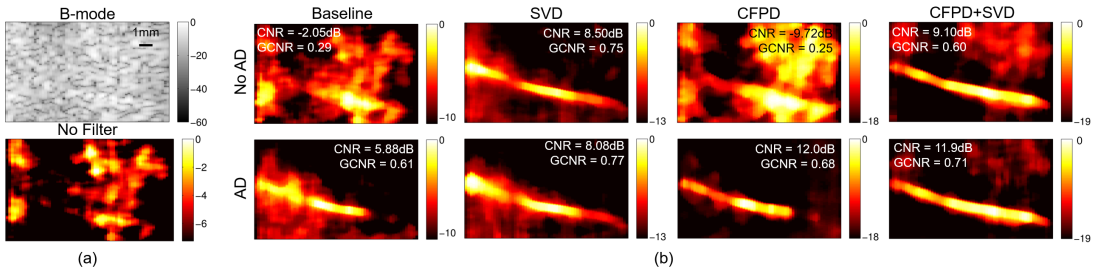

Figure 4.9: Qualitative example of the single vessel phantom with 5mm/s average blood velocity. (a) B-mode image and power Doppler image made without filtering. (b) Power Doppler images made with adaptive demodulation (AD) (bottom) and without (top) for baseline, SVD, CFPD, and CFPD+SVD. A 400ms ensemble was used for all power Doppler images. CNR and GCNR values are displayed on each image for reference. Images are on a dB scale.

The quantitative results for the 1mm/s average velocity single vessel phantom data are shown in Figure 4.8c. For this case, SNR and CNR are low for all methods at the smallest ensembles (below 200ms), indicating poor vessel visibility. However, SNR and CNR improve with ensembles above 200ms, especially when using adaptive demodulation with SVD. Adaptive demodulation with SVD also resulted in the highest GCNR for ensemble sizes above 200ms, but SVD by itself produces the least amount of overlap for ensembles below 200ms. Generally, adaptive demodulation improved SNR, CNR, and GCNR for each

method.

Figure 4.10 shows power Doppler images for an example case for the 400ms ensemble for all combinations of adaptive demodulation, CFPD, and SVD for the 1mm/s average flow phantom data. Figure 4.10a shows the B-mode and no filter power Doppler images for reference. Adaptive demodulation with SVD appears to suppress the background noise the best, but, similar to the faster flow phantom data, adaptive demodulation with CFPD+SVD shows the most uniform flow through the vessel and resulted in both the highest CNR and GCNR.

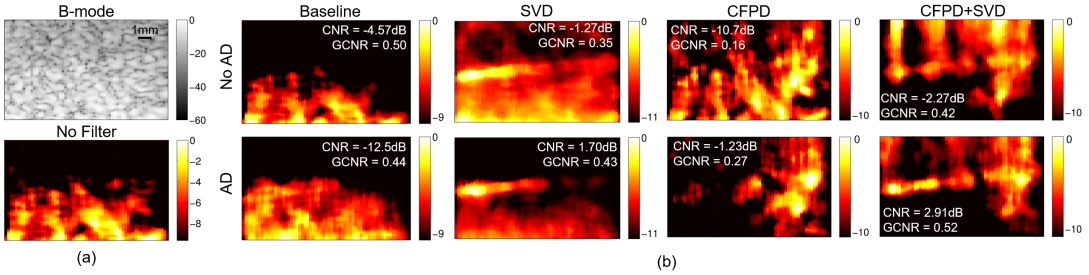

Figure 4.10: Qualitative example of the single vessel phantom with 1mm/s average blood velocity. (a) B-mode image and power Doppler image made without filtering. (b) Power Doppler images made with adaptive demodulation (AD) (bottom) and without (top) for baseline, SVD, CFPD, and CFPD+SVD. A 400ms ensemble was used for all power Doppler images. CNR and GCNR values are displayed on each image for reference. Images are on a dB scale.

4.3.3 *In Vivo*

Figure 4.11 shows anatomical SLSC images with corresponding power Doppler images before and after TACE. Before TACE, SVD and adaptive demodulation with SVD show the most heightened power in the tumor compared to the surrounding healthy liver tissue. After TACE, adaptive demodulation by itself and adaptive demodulation with SVD show the clearest suppression of power in the tumor compared to the surrounding tissue. There is an apparent vessel to the right of the tumor after TACE that is most clearly seen with CFPD combined with adaptive demodulation and CFPD combined with adaptive demodulation

and SVD.

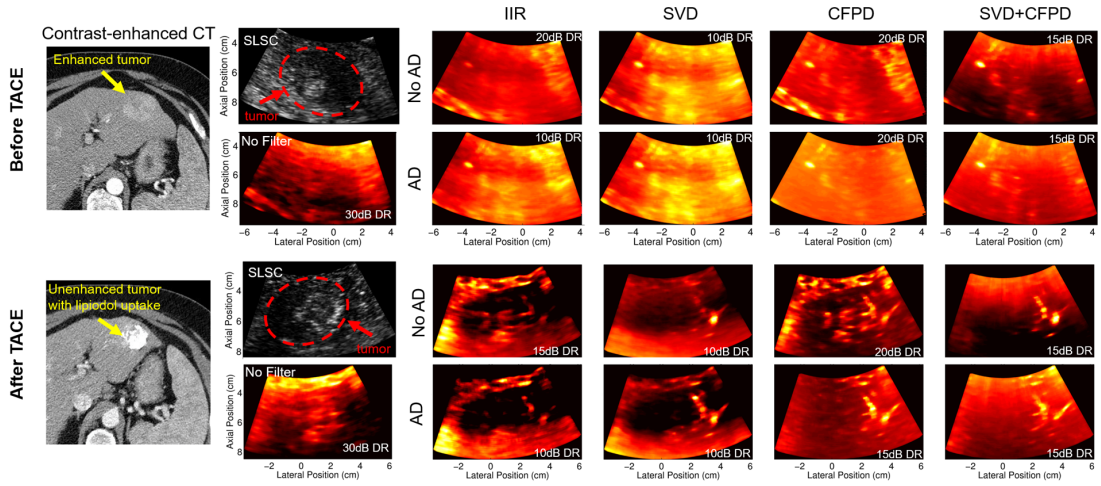

Figure 4.11: Gold-standard contrast-enhanced CT, anatomical SLSC and power Doppler images before (top) and after (bottom) TACE. Post-treatment CT and ultrasound were acquired 2 months and immediately after TACE, respectively. Power Doppler images are shown for each combination of adaptive demodulation (AD), SVD, and CFPD as well as for baseline IIR filtering and no tissue filtering. Dynamic ranges (DR) are displayed on each power Doppler image and were chosen to ensure qualitatively similar noise floors.

Figure 4.12 demonstrates the potential need for different dynamic ranges for data with and without adaptive demodulation. Based on the example in Figure 4.12, a 10dB dynamic range includes the majority of the signal for the image with adaptive demodulation. However, if a 10dB dynamic range is used for the data without adaptive demodulation, the majority of the signal is excluded. This is likely because more tissue passed through the conventional IIR filter when adaptive demodulation was not used. Therefore, a 20dB dynamic range was chosen for the data without adaptive demodulation to obtain qualitatively similar overall intensities.

The quantitative tumor-to-background contrast results are displayed in Table 4.2. SVD by itself resulted in the highest contrast and GCNR before TACE, while adaptive demodulation with IIR filtering resulted in the lowest contrast after TACE (i.e., largest suppression of power in the tumor compared to surrounding tissue). Adaptive demodulation with SVD resulted in the largest temporal change in power (6.9dB).

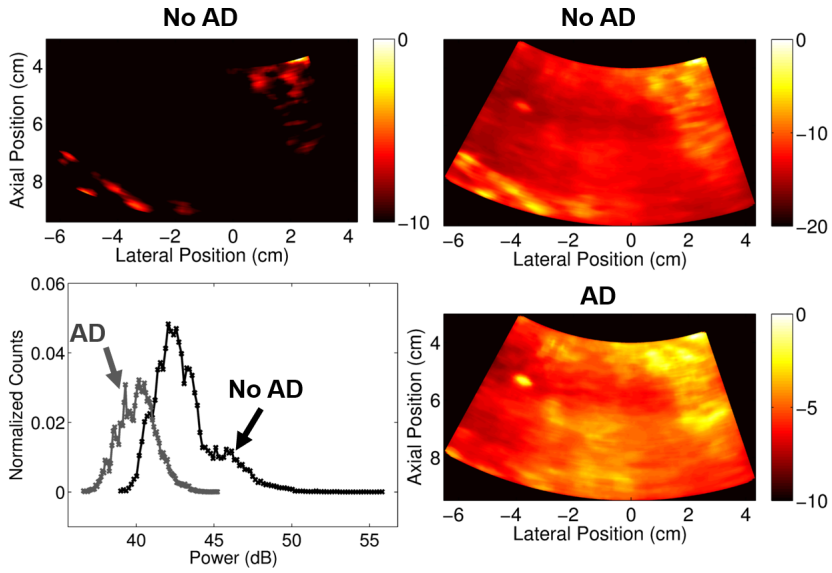

Figure 4.12: *In vivo* dynamic range evaluation. Power Doppler images are on a dB scale and are shown for the data before TACE made with conventional IIR filtering. Images without adaptive demodulation (AD) are shown in the top row with dynamic ranges of 10dB (left) and 20dB (right). The image with AD is shown in the bottom right and is made with a dynamic range of 10dB. The plot in the bottom left shows the histograms of the data (after log compression but before scaling to the maximums) with AD (gray) and without AD (black).

The gold-standard contrast-enhanced CT images support the ultrasound results. The pre-treatment CT image confirms that the tumor had greater cumulative vasculature compared to the surrounding healthy liver tissue. The 2 month follow-up CT image after TACE confirms that the treatment successfully stopped blood flow to the tumor and that lipiodol was retained, indicating tumor necrosis [30].

4.4 Discussion

The simulated parameter study resulted in expected trends for the blood-to-noise ratio, tissue-to-blood ratio, and peak velocity experiments. We anticipated that adaptive demodulation would become less effective in noisy environments because, regardless of tissue bandwidth suppression, blood would be overpowered by noise, which is what we saw for

Table 4.2: Tumor-to-background contrast (dB) before and after TACE computed on power Doppler images with no filtering and with all possible combinations of IIR, SVD, CFPD, and adaptive demodulation (AD). GCNR values are indicated in parentheses. Change in contrast = $C_{before} - C_{after}$.

Method	Before TACE	After TACE	Change
No Filter	2.4 (0.19)	7.4 (0.64)	-5.0
IIR	2.2 (0.88)	-3.3 (0.91)	5.5
AD+IIR	1.8 (0.90)	-5.0 (1.00)	6.8
SVD	2.4 (0.97)	-3.7 (1.00)	6.0
AD+SVD	2.3 (0.96)	-4.6 (1.00)	6.9
CFPD	0.1 (0.33)	2.2 (0.58)	-2.1
AD+CFPD	-0.7 (0.62)	0.1 (0.07)	-0.7
CFPD+SVD	0.4 (0.29)	3.7 (0.93)	-3.3
AD+CFPD+SVD	-0.4 (0.49)	2.6 (1.00)	-3.1

blood-to-noise ratios below -20dB. Also, because adaptive demodulation relies on tissue to be sufficiently stronger than blood so as not to estimate and demodulate blood motion, we expected to see a decrease in blood-to-background SNR at low tissue-to-blood ratios, which is what we observed for tissue-to-blood ratios less than 20dB. Finally, we expected to see increased blood-to-background SNR as peak blood velocity increased because this would lead to better spectral separation between blood and tissue, which is what we saw for all velocities tested.

The parameter study also resulted in a few unexpected trends. We expected to see an increase in blood-to-background SNR with larger kernel sizes, longer lags, and higher imaging frequencies, but we saw minimal changes when varying these parameters. We expected that increasing the kernel size would improve the accuracy of the tissue displacement estimator and thereby improve the adaptive demodulation of the tissue clutter [57], but we actually observed a slight decrease with larger kernels. It is possible that small tissue displacements were averaged out with the larger kernels [57], preventing full demodulation of the tissue clutter. We also expected tissue displacement estimation accuracy, and therefore adaptive tissue clutter demodulation, to improve with larger lags [56], and although we

did see a very slight increase in SNR for lags above 1 slow-time sample, the small improvement does not warrant the trade off for longer processing times. For the realizations used in this experiment, it is possible that a lag of 1 slow-time sample produces estimates that are sufficiently close to the true displacement which is why we do not see much improvement with larger lags. Larger kernel sizes and lags can also suffer from decorrelation effects which could also explain the observed trends [73]. Finally, we expected to see a consistent increase in SNR with increasing imaging frequencies, which would support the findings by Heimdal and Torp [14]. However, without adaptive demodulation, SNRs are relatively constant, and with adaptive demodulation, SNR does increase slightly, but decreases for the 10MHz case. These discrepancies could be because we used different kernel sizes for different center frequencies to maintain similar axial fields of view. Also, it is possible that we would see a steadier increase if we looked at more frequencies above 10MHz.

Although precisely optimal tissue cutoffs were not used for IIR and SVD filtering, Figures 4.6 and 4.7 demonstrate that the observed optimal trends are still generally achieved with a fixed IIR cutoff and an adaptive SVD approach. Optimal cutoff selection is impossible clinically with unknown structures in the field of view. Therefore, for realistic clinical scenarios, cutoffs are chosen based on the application, which we have reproduced here to showcase the feasibility of these methods.

The simulation results were mostly validated with the single vessel phantom data with 5mm/s average blood flow. The phantom blood-to-background SNR, CNR, and GCNR for this case have similar trends and values to the simulated metrics. However, unlike simulations, the highest SNR is achieved when combining all three methods together. Apart from this discrepancy, the 5mm/s velocity phantom trends generally agree with the simulation trends, which supports the reproducibility of our simulations. The slower flow phantom data (1mm/s average flow) produced lower metric values overall and the trends were not as well matched to the simulation and faster flow phantom data. For this case, SVD with and without adaptive demodulation produced the highest SNR, CNR, and GCNR. For ensem-

bles below 500ms, adaptive demodulation with SVD improves SNR and CNR compared to SVD by itself. Although this phantom case produced different trends than the simulations and 5mm/s phantom case, it still demonstrates the value of adaptive demodulation for each method (i.e., the dotted AD curves are all generally higher than the solid no AD curves). Furthermore, the example realization shown in Figure 4.10 shows how these techniques have the potential to resolve predominately lateral flow.

For both the simulations and 5mm/s average flow phantom data, the SNRs, CNRs, and GCNRs for all cases appear to either peak at smaller ensembles and then converge at larger ensembles or slowly plateau. This is less apparent for the 1mm/s average flow phantom, but still generally true. It is possible that the metrics converge due to signal decorrelation at long ensembles and that averaging over shorter ensembles would produce higher image quality metrics. Another hypothesis is that the demodulated noise becomes a more significant source of error for longer ensembles. Future work will aim to investigate correlation changes through slow-time as well as the effects of the demodulated noise term. Additionally, longer than 1s ensembles should be evaluated to see if SNR, CNR, and GCNR truly converge or if they ultimately continue to increase or decrease.

The *in vivo* TACE study provides a unique setting for testing slow flow techniques because it involves both spatial and temporal changes in perfusion. Before TACE we expect to see heightened power in the tumor because we know liver tumors are highly vascularized compared to the surrounding healthy liver tissue. Gold-standard pre-treatment CT imaging confirms this, and 2-month follow-up CT imaging confirms that the treatment was successful. Therefore, after TACE we expect to see suppressed power Doppler in the tumor compared to surrounding tissue. For the example case included in this work, adaptive demodulation combined with IIR and adaptive demodulation combined with SVD resulted in the largest changes in tumor contrast, suggesting that there is a potential benefit of using adaptive demodulation for detecting both temporal and spatial changes in tumor perfusion before and after TACE. Although other factors could contribute to the increase in power

in the tumor before TACE, it is reasonable to believe that most of the enhanced power is due to increased flow because we know this happens physiologically. Also, because we are using a 30Hz (5.5mm/s) IIR cutoff, we do not expect power in the images to be directly correlated to perfusion, but we do expect to be visualizing flow in vessels that directly feed into and drain out of capillaries, such as arterioles and venules. In the power Doppler images after TACE, a vessel to the right of the tumor is clearly resolved. This residual flow could potentially be from the pressure head of the feeding artery reaching but not perfusing the tumor branches, indicating successful arterial occlusion.

GCNR is a newly proposed metric that should be robust to dynamic range alterations caused by adaptive beamformers [70]. By computing the probability of detection, GCNR avoids the inherent issue with scaling SNR, CNR, and contrast for different beamformers that alter the signal in some way. We have implemented it in this work to account for comparisons between the different beamformers used in simulations, phantoms, and *in vivo* data, namely plane wave synthetic focusing and SLSC used in CFPD. In our initial implementation, GCNR generally agrees with the SNR, CNR, and contrast metrics. However, we also observed that GCNR can result in discrepancies between what is observed qualitatively. For example, in Figure 4.10, the GCNR value for conventional IIR filtering by itself (i.e., baseline) is 0.5, suggesting that there is a 50% chance of detecting flow in the vessel, which is not seen in the image. However, for adaptive demodulation and SVD, the GCNR value is only 0.43, even though the vessel is clearly seen in the image. The GCNR values make sense because the vessel signal is clearly much lower compared to background in the baseline image, while the vessel and background have more overlapping pixels in the adaptive demodulation and SVD image. However, the vessel is visually detected in the adaptive demodulation with SVD image despite the GCNR metric. Therefore, GCNR along with CNR, SNR, and contrast should be used carefully for flow detection comparisons.

The single vessel model used for the simulation and phantom experiment is useful for comparing techniques. However, it is not fully representative of realistic *in vivo* settings in

which many small vessels will be in the field of view and within a given resolution cell. The simulation and phantom vessel diameters used in this work are relatively small, but they are not on the order of capillary or other small vessel diameters, which are smaller than the achievable lateral resolution. Therefore, we do not expect to resolve flow in individual capillaries or other small vessels, especially with lower transmit frequencies and at deeper depths, as was used in our *in vivo* study, but we do expect to be sensitive to flow from the collection of small vessels within a given resolution cell. Based on this assumption, we hypothesize that heightened power within a single pixel in the tumor in our *in vivo* images before TACE in Figure 4.11 potentially results from increased flow in several small vessels within that pixel.

Apart from resolution limitations, depth-dependent SNR limitations will also affect perfusion imaging techniques at deeper depths. The simulation and phantom experiments in this work focus on shallower depths for testing different techniques, but realistic *in vivo* imaging will require sensitivity at deeper depths, as we observe in our *in vivo* example. We demonstrate that these techniques, especially adaptive demodulation and SVD, can work in realistic settings at depths down to 9.5cm and produce results that are consistent with expected physiological treatment effects. However, we show in Figure 4.3c that adaptive demodulation performs best at blood-to-noise SNRs above 20dB. This suggests that adaptive demodulation will suffer as SNR decreases. Similarly, the global SVD approach that we have applied relies on similar noise statistics throughout the field of view. This is less attainable *in vivo* with larger, deeper fields of view [49]. Song et al. addresses this with a block-wise approach with noise equalization [49]. Also, CFPD intends to improve depth-dependent SNR limitations by reducing near field reverberation clutter and thermal noise [41]. Therefore, implementing and optimizing some of these techniques could further improve imaging of slow flow at deeper depths.

It is worth noting that the CFPD signal has not yet been shown to be linearly correlated to blood volume as is the case with conventional power Doppler. Also, conventional power

Doppler signal will become less correlated to blood volume in low SNR environments. Because capillaries and other small vessels often cannot be qualitatively resolved, blood volume quantification is crucial. Therefore, the value of CFPD may be most relevant for resolvable structures, and, assuming reasonable SNR, conventional power Doppler with adaptive demodulation and SVD would be the best option for sub-resolution structures.

4.5 Conclusion

Perfusion ultrasound imaging is difficult, mainly because of spectral broadening of tissue clutter signal caused by patient and sonographer hand motion, but other issues like SNR are also challenging. We previously introduced adaptive demodulation as a solution for suppressing tissue clutter bandwidths. We implemented the method using single plane wave imaging and conventional IIR filtering. Here, we showed that we can improve this technique with better beamforming (plane wave synthetic focusing and CFPD) and tissue filtering (SVD). Simulated blood-to-background CNRs were highest when using adaptive demodulation with CFPD with smaller ensembles. Phantom CNRs were highest when combining adaptive demodulation, CFPD and SVD for the 5mm/s flow speed and when combining adaptive demodulation and SVD for the 1mm/s flow speed. Finally, we showed clinical feasibility and potential benefit for combining adaptive demodulation and SVD in our *in vivo* liver tumor embolization study. Combining these proclaimed slow-flow techniques has the potential to make perfusion ultrasound imaging possible.

Chapter 5

Adaptive Clutter Demodulation for Transarterial Chemoembolization Treatment Evaluation of Liver Tumors

This work is currently in review for publication in Scientfic Reports: Tierney, Jaime, et al. "Non-contrast power Doppler ultrasound imaging for early assessment of trans-arterial chemoembolization of liver tumors" *Scientific Reports*.

5.1 Introduction

As discussed in Section 1.3, transarterial chemoembolization (TACE) is a treatment option for hepatic malignancies that do not qualify for curative surgery [24, 25, 26, 27]. It works by simultaneously delivering high doses of chemotherapy and embolizing agents to the blood supply of a tumor to provide targeted treatment and occlude the arterial supply [24, 25, 26]. Gold-standard imaging evaluation aims to detect changes in tumor perfusion using contrast agents, assuming that decreased contrast in the tumor post-TACE indicates successful treatment [30]. However, contrast agents can cause artifacts that prevent follow-up imaging from being performed earlier than 4 weeks after treatment with gold-standard modalities [30, 27]. Although contrast-enhanced ultrasound has been considered as a solution to this problem [27], ultrasound contrast agents can also introduce treatment-related artifacts [33, 27]. Furthermore, contrast agents in general are limited by time and dose in the blood stream, making real-time applications challenging. Although Doppler ultrasound techniques without contrast have been shown to be limited by attenuation and tissue clutter for perfusion (i.e., the slowest blood flow in the smallest vessels) imaging applications in the past [34, 14, 36], there have been several significant advancements to slow blood flow imaging with ultrasound in recent years (as discussed in previous chapters) that have yet to

be assessed for use in TACE treatment evaluation.

Perfusion imaging with conventional Doppler techniques has been challenging mainly because of Doppler processing limitations, ineffective tissue filtering, and beamforming limitations [14, 36]. Conventional color Doppler techniques are generally limited by signal-to-noise ratio (SNR) and depend on knowing the beam-to-flow angle to make accurate estimations of blood velocity [8]. However, because perfusion signal is weak and occurs in the smallest and most randomly oriented vessels, estimating perfusion velocity is particularly challenging with color Doppler techniques [11, 12]. The introduction of power Doppler helped to overcome this problem because it computes the energy of the Doppler signal or the amount of moving blood as opposed to velocity, making it more sensitive to weak perfusion signal in addition to being relatively angle independent [8, 9].

Despite addressing SNR and the angle-dependency problem, tissue clutter interference with blood signal remains a barrier for perfusion applications. Tissue filtering techniques in general have been extensively studied and optimized for the purposes of conventional focused Doppler processing [13, 15, 19, 18, 20, 21]. Among these techniques are adaptive tissue motion correction schemes to be implemented prior to tissue filtering in the frequency-domain [13, 19]. Additionally, the most common clutter filtering methods, including infinite and finite impulse response (IIR and FIR, respectively) filters and polynomial regression filters, have been exhaustively evaluated and compared [15, 21]. Similarly, eigen-based filtering techniques have been extensively studied and have been shown to be superior to more traditional techniques, albeit more computationally expensive [43, 44, 45, 46]. However, a main limitation for all of these methods has been the trade-off between maintaining real-time frame rates and acquiring long ensembles for sufficient tissue filtering, a problem resulting from conventional Doppler beamforming which acquires a single line of a Doppler ensemble at a time [10].

More recently, advancements in beamforming have been proposed to improve sensitivity to slow flow, including plane wave synthetic focusing and coherent flow power Doppler

(CFPD) [39, 10, 41]. Plane wave applications have simultaneously overcome the trade-off between ensemble length and frame rate and have sparked renewed research in the area of slow flow imaging with ultrasound. As part of this renewal, we expanded upon the the tissue motion correction schemes mentioned previously [19, 13] and developed a time-domain adaptive tissue clutter demodulation scheme on long ensemble plane wave data, accounting for both phase and amplitude modulation to suppress the bandwidth of tissue clutter prior to filtering [54]. Plane wave techniques have also led to advanced eigen-based filtering techniques that can achieve full spatio-temporal 2D and higher order singular value decompositions (SVD) [17, 47, 48, 49]. Using mainly proof-of-concept experiments, we previously showed that combining our adaptive demodulation technique with some of the other latest improvements in tissue filtering and beamforming could potentially make imaging perfusion without contrast possible [68].

Although non-contrast power Doppler imaging has been considered for TACE treatment evaluation in the past [34], it has not been considered with the latest perfusion-focused improvements. Here, we propose non-contrast power Doppler imaging with adaptive demodulation in combination with improvements in beamforming and tissue filtering as a potential tool to evaluate TACE. Apart from the clinical benefits of using non-contrast ultrasound, because TACE acutely changes tumor perfusion, it also provides a unique clinical scenario to evaluate adaptive demodulation and other slow flow ultrasound algorithms. Additionally, this study tests these methods at deeper depths and with a lower transmit frequency than used in any other proof-of-concept studies. We demonstrate initial feasibility in a small pilot study.

5.2 Materials and Methods

5.2.1 Patients and Procedure

This study was approved by and performed in accordance with the relevant guidelines and regulations of Vanderbilt's institutional review board. Ten patients undergoing TACE gave informed written consent to participate. One of the patients received TACE twice (3 months apart) and consented twice, resulting in a total of 11 subject acquisitions. Inclusion criteria consisted of the patient being over 21 years of age with a scheduled TACE procedure and the ability to provide informed consent. All patients received conventional TACE. The ultrasound acquisitions did not alter the treatment protocol or impose any additional risk for which ethical committee authorization would be necessary. Table 5.1 summarizes patient demographics and tumor information.

Table 5.1: Summary of patient demographics and tumor characteristics for each subject acquisition. Tumor types consisted of neuroendocrine tumors (NET) and hepatocellular carcinomas (HCC). Tumor size is indicated as the largest measured diameter.

Subject	**Age (y)**	**Sex**	**BMI ($\frac{kg}{m^2}$)**	**Type**	**Size (cm)**	**Location**
1	56	M	47.4	HCC	4.7	Segment 3
2	52	F	23.0	HCC	2.0	Segment 5/6
3	55	M	24.4	NET	6.3	Segment 6
4*	60	F	27.3	HCC	3.4	Segment 5
5	58	M	25.8	HCC	2.4	Segment 5
6	43	F	25.0	NET	6.0	Segment 6/7
7	64	F	22.4	NET	4.1	Segment 4B
8*	60	F	27.3	HCC	4.5	Segment 5
9	60	M	32.5	HCC	3.4	Segment 5/6
10	73	M	21.7	NET	6.0	Segment 6
11	63	M	24.4	HCC	5.3	Segment 6

*same patient

5.2.2 Imaging

A Verasonics C5-2 probe with a 4.2MHz center frequency was used to acquire a 6cm focused scan followed continuously by 2s of an angled plane wave sequence. For both the focused and unfocused sequences, the channel data were acquired and saved immediately before and after TACE for each patient. Compared to a focused scan which acquires a single line at a time, plane wave imaging insonifies the entire field of view at once, as depicted in Figure 5.1. In the case of a curvilinear array, the wave is more spherical than planar, but we use the term "plane wave" to be consistent with the literature. With respect to Doppler techniques, plane wave imaging overcomes the long-standing trade-off between frame rate and ensemble length [10] and is discussed in more detail in the following section. The plane wave sequence used 9 angles between -8° and 8° at a PRF of 5.4kHz. Both sequences imaged down to 10cm. Imaging was performed by the interventional radiologist performing the procedure. When possible, patients were asked to hold their breath during each scan.

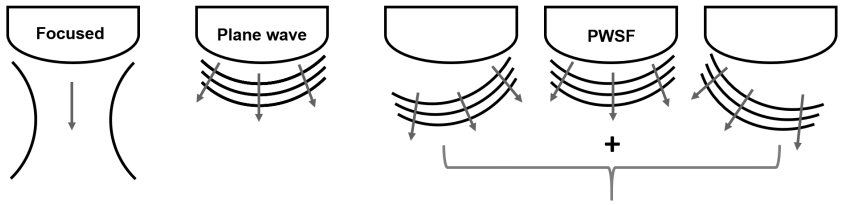

Figure 5.1: Cartoon depiction of the different transmit sequences used in this study. Focused scans acquire a single lateral location of an image at a time and are focused at a single depth. Plane wave scans sacrifice transmit focusing and involve transmitting from all elements at once to insonify the entire field of view. Plane wave synthetic focusing (PWSF) involves transmitting multiple angled plane waves and then summing them to gain transmit focusing throughout the image (i.e., at all depths and lateral locations).

5.2.3 Post-processing

All post-processing was done in MATLAB R2014a (The MathWorks, Inc., Natick, MA).

5.2.3.1 Beamforming

For the focused sequence, conventional delay-and-sum beamforming was used to generate anatomical B-mode images. Short-lag spatial coherence (SLSC) beamforming was also implemented on the focused data for additional and sometimes improved anatomical referencing [42]. A maximum aperture lag of 10 elements and an axial kernel size of 1.5λ (λ=center frequency wavelength) were used for SLSC beamforming. For both delay-and-sum and SLSC, Hann apodization and aperture growth to achieve an F/# of 2 were implemented during receive beamforming.

For the plane wave sequence, plane wave synthetic focusing was implemented as in Montaldo et al. [39], resulting in a frame rate of 600Hz after beamforming. Plane wave synthetic focusing, as depicted in Figure 5.1, combines beamformed consecutive angled plane wave data to achieve transmit focusing throughout the image [39]. Hann apodization and aperture growth to achieve an F/# of 2 were implemented during receive beamforming. Beamformed data were up-sampled and band-pass filtered. Up-sampling was performed to achieve a sampling frequency of 50MHz. For tissue filtering and power Doppler estimation (described in following subsections), a 1s (600 sample) ensemble (either the first or second half of the full 2s ensemble) was qualitatively chosen based on M-mode motion for each data set. The first 0.5s of each 1s ensemble was used for initial qualitative and quantitative comparisons between patients and filtering techniques. An ensemble size evaluation was also performed for which ensembles between 83ms and 1s (50 and 600 samples) were compared. Due to frame rate limitations, conventional focused power Doppler imaging only uses up to 16 samples [10]. To mimic a conventional scan, a 16 sample ensemble was also evaluated and will be referred to as the "conventional" method. However, it is worth noting that because we are using plane wave synethetic focusing to focus at all locations, our "conventional" method should still be better (in terms of resolution) than traditional power Doppler imaging as currently implemented on most commercial scanners.

5.2.3.2 Adaptive Demodulation

Adaptive demodulation was applied as in Tierney et al. [54] to the beamformed plane wave data. To account for axial tissue motion, phase demodulation was implemented using a 10λ (λ=center frequency wavelength) axial kernel size and lag of 1 slow-time sample (1.7ms) to compute relative and total tissue displacements through slow-time, respectively. These parameters were chosen based on previous work [68]. Amplitude demodulation did not provide any additional benefit and was therefore not applied.

A mean frequency down-mixing approach was also implemented on the conventional sequence for which there may be a substantial mean tissue frequency other than zero due to the short ensemble length. This was implemented the same way as was done in Bjaerum et al. [15]

5.2.3.3 Tissue Filtering

Each data set was cropped to a smaller field of view prior to tissue filtering. A conventional IIR filter as well as an adaptive SVD filter were applied to each data set. For the IIR filter, a 30Hz (5.5mm/s) high-pass 6th order type 1 Chebyshev filter was used. A symmetric initialization was performed for which 20 mirrored samples (16 samples for the conventional case) were added to each slow-time signal before filtering and removed after. The IIR filter used was chosen based on previous studies [13] as well as internal comparison to other IIR and FIR filters. For the SVD filter, an adaptive 2D spatio-temporal approach was used as in Song et al. [49]. The same thresholds were used for all data sets for adaptively determining tissue and noise cutoffs. Two tissue cutoffs were computed and the maximum or minimum were used based on which produced the best qualitative and quantitative result for the 0.5s (300 sample) ensemble for each data set.

5.2.3.4 Image Evaluation

Power Doppler was computed on each data set using

$$PD(x,z) = \sum_{t=1}^{T} |s(x,z,t)|^2 \tag{5.1}$$

where $s(x,z,t)$ is the filtered analytic signal, x,z,t are the spatial, axial, and temporal dimensions, and T is the total number of slow-time samples (i.e, ensemble size). A 2mm by 2mm spatial median filter was applied to each power Doppler image. Aperture growth effects were accounted for by dividing each power Doppler value at a given depth by the number of aperture positions used for aperture growth at that depth.

To quantify differences between before and after TACE time points as well as differences between processing techniques, we use a tumor-to-background contrast metric as follows,

$$C = 10log_{10}\frac{\frac{1}{N}\sum_{i=1}^{N} PD_{tumor}(i)}{\frac{1}{M}\sum_{i=1}^{M} PD_{bkgd}(i)} \tag{5.2}$$

where N and M are the total number of pixels in the tumor and background, respectively, and PD_{tumor} and PD_{bkgd} are the power Doppler values in the tumor and background, respectively. Contrast provides a relative measurement of spatial changes in power between the tumor and surrounding liver tissue. To measure temporal changes, change in contrast was computed as the difference between time points (before minus after) for each patient. Power amplitude can vary between acquisitions due to different noise characteristics and fields of view, which can make comparisons between before and after TACE challenging. However, because contrast is a relative metric to each individual image, comparing temporal changes in contrast is feasible. Furthermore, these quantitative metrics are independent of how the images are scaled for qualitative display. Example tumor and background masks are shown in Figure 5.2. Masks were manually drawn for each data set using the power Doppler images in addition to the anatomical B-mode and SLSC images.

Assuming successful treatment, we expect decreased power (i.e., perfusion) in the tumor after TACE. We also expect potentially elevated power in the tumor before TACE due to tumor hypervascularity [27, 30, 33]. Based on this hypothesis, we expect contrast to be positive before TACE, which would suggest increased blood flow in the tumor relative to the background tissue. Conversely, we expect contrast to be negative after TACE if blood flow in the tumor has been effectively occluded. Therefore, we expect the change in tumor contrast to be positive and greater than the before TACE contrast value, which would mean that the power in the tumor decreased after TACE relative to the power in the tumor before TACE.

Displayed power Doppler images were made by log compressing (5.1) ($I = 10log_{10}PD(x,z)$). Images were scaled to individual maximums and dynamic ranges were chosen to include the middle 70% of the full dynamic range (i.e., the top and bottom 15% were set to the maximum and minimum values, respectively).

5.2.3.5 Statistics

Post-hoc power was computed on the change in contrast values for comparisons between each filtering technique and the conventional method, assuming a 2-sided test with $\alpha = 0.05$ and normal distribution. Additionally, a two-sample paired t-test was performed between each filtering technique and the conventional method. Furthermore, to determine relative contributions to differences between techniques, a linear regression model was fit to the change in contrast values for which ensemble size, adaptive demodulation, and SVD were used as predictors. To facilitate direct comparisons, each predictor was centered about the mean and normalized by overall power. An F-test was used to assess the model fit.

5.3 Results

Focused B-mode and SLSC images were both used for identifying tumor boundaries and determining crop regions. Figure 5.2 shows example focused B-mode and SLSC im-

ages of subject 10 before and after TACE. The tumor is clearly seen in both the B-mode and SLSC images, but some boundaries and structures are enhanced with SLSC. Example tumor and background regions of interest (ROIs) are shown overlaid on the SLSC images for reference. Using the anatomical focused B-mode and SLSC images, the beamformed data were cropped to around the tumor for tissue filtering and power Doppler estimation, as depicted by the orange crop region in Figure 5.2. This smaller field of view was used to better facilitate our global SVD filtering approach which assumes similar noise statistics throughout the input region [49].

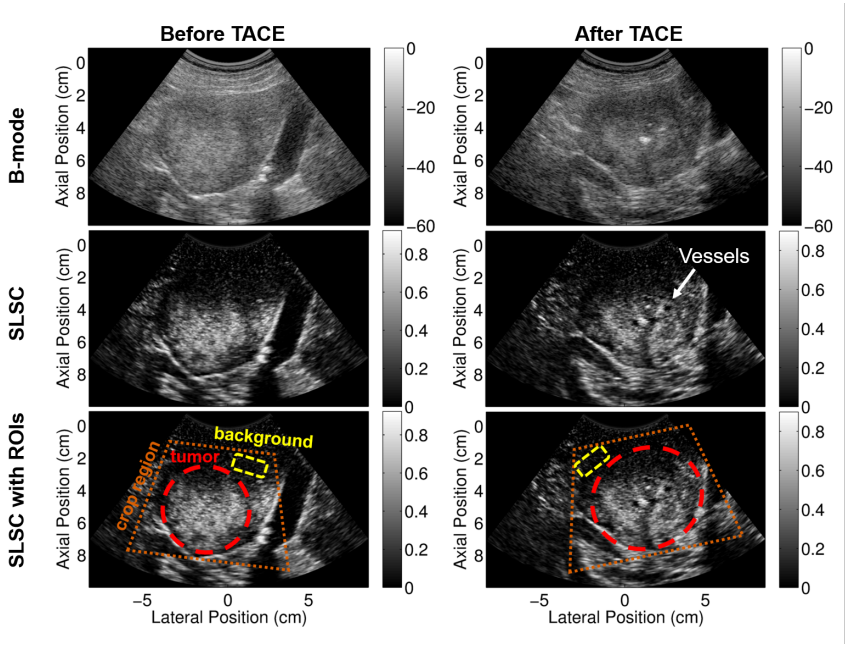

Figure 5.2: Example full field of view focused B-mode (top) and SLSC (middle and bottom) images before (left) and after (right) TACE. Potential vessels are indicated in the after TACE SLSC image that are not apparent in the B-mode. Example crop region (orange), tumor (red), and background (yellow) ROIs are displayed on focused full field of view SLSC images in the bottom row. B-mode images are scaled to individual maximums and are displayed on a dB scale. SLSC images are scaled from 0 to the maximum coherence in the image.

Qualitatively, adaptive demodulation with SVD filtering produced power Doppler images that have increased power (i.e., blood flow or perfusion) in the tumor before TACE and decreased power after, which is consistent with the hypothesis for complete or partial response and is less apparent with conventional power Doppler. This is apparent in Fig

5.3 which shows example cropped B-mode, SLSC, and power Doppler images for subjects 10, 9, and 5 before and after TACE. Power Doppler images were made with conventional methods (16-sample ensemble with IIR filtering) as well as with adaptive demodulation and SVD filtering (300-sample ensemble). Specifically, the overall power distribution within the tumor in the conventional power Doppler images is similar between time points for each case. Furthermore, the structures seen in the conventional power Doppler images are highly correlated to the structure seen in the focused B-mode and SLSC images. The power Doppler images with adaptive demodulation and SVD filtering show structures unseen in the B-mode and SLSC images, such as clear vessels surrounding the tumor, as shown in Fig 5.3a for subject 10. Although the power in the tumor for subject 9 (Fig 5.3b) is not necessarily lower than the power in the surrounding liver tissue after TACE in the image with adaptive demodulation and SVD filtering, as is perhaps the case in Figs 5.3a and 5.3c for subjects 10 and 5, respectively, it is likely that a partial response to treatment was achieved based on the comparison between the post-TACE the pre-TACE images. Additionally, for subject 5, although power in the tumor is faint before TACE with adaptive demodulation and SVD filtering, power is clearly lower in the tumor after TACE compared to surrounding liver tissue when using advanced methods, as shown in Fig 5.3c. These observations are not apparent when using conventional methods.

The dynamic ranges of the displayed power Doppler images are different because of the adaptive scaling approach described previously. However, the dynamic ranges are also inherently different because of the different filters and processing techniques used. If the advanced methods are better able to suppress signal from tissue and noise, the dynamic range will be smaller because it will only include the blood signal. If tissue and noise are still present, as can be the case with conventional methods, the dynamic range will be larger because it will include the signal energy from each component (tissue, blood, and noise). Figure 5.4 demonstrates the potential variability in dynamic ranges and shows histograms and corresponding power Doppler images after TACE for subject 9. Histograms were made

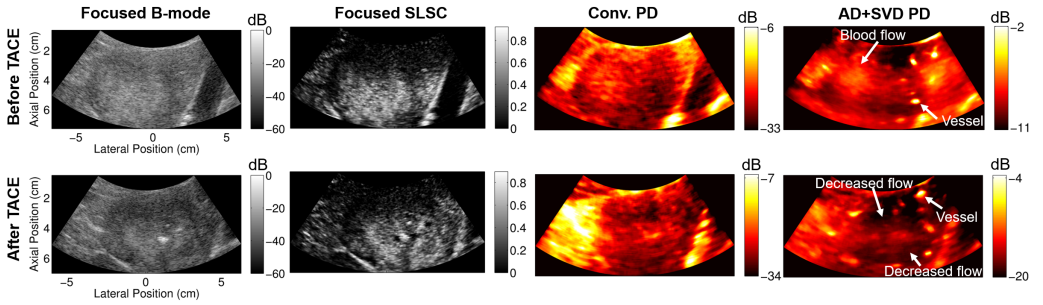

(a)

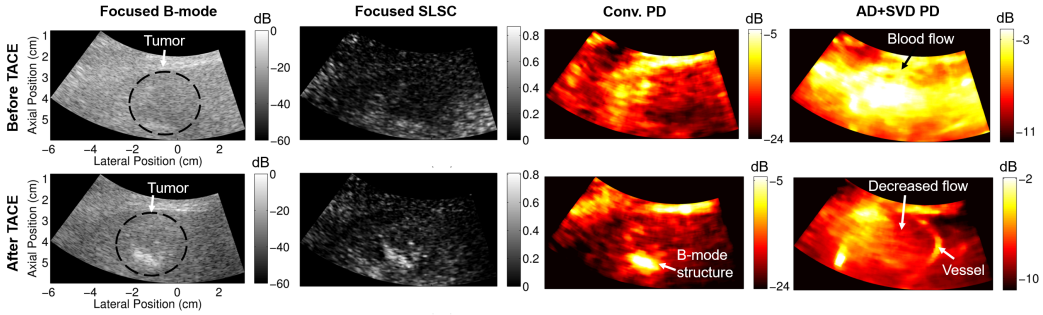

(b)

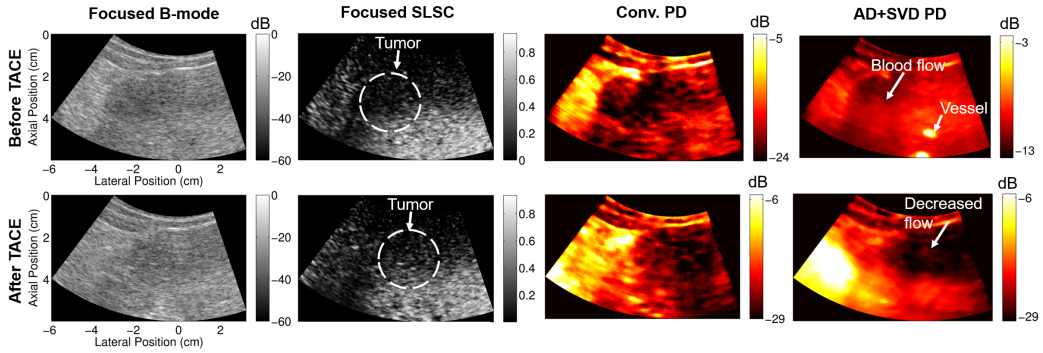

(c)

Figure 5.3: Focused B-mode, focused SLSC, and power Doppler images before (top) and after (bottom) TACE for subjects 10 (a), 9 (b), and 5 (c). Power Doppler (PD) images were made with conventional (Conv.) methods and with adaptive demodulation (AD) and SVD filtering. 27ms (16 samples) and 0.5s (300 samples) ensemble sizes were used for the conventional and advanced methods, respectively. SLSC images are scaled from 0 to the maximum coherence in the image. Potential vessels, tumor flow, and decreased flow are indicated in the AD+SVD images that are not apparent in the conventional PD images for each case.

of the power Doppler images after log compression and scaling to individual maximums. The histograms show how the dynamic range is much larger when conventional methods are used, suggesting that tissue and noise are present. The adaptively chosen dynamic ranges intend to include the majority of each signal, as seen by the orange and green dots on the histograms in Figure 5.4 which indicate the adaptive dynamic ranges for the conventional and advanced methods, respectively.

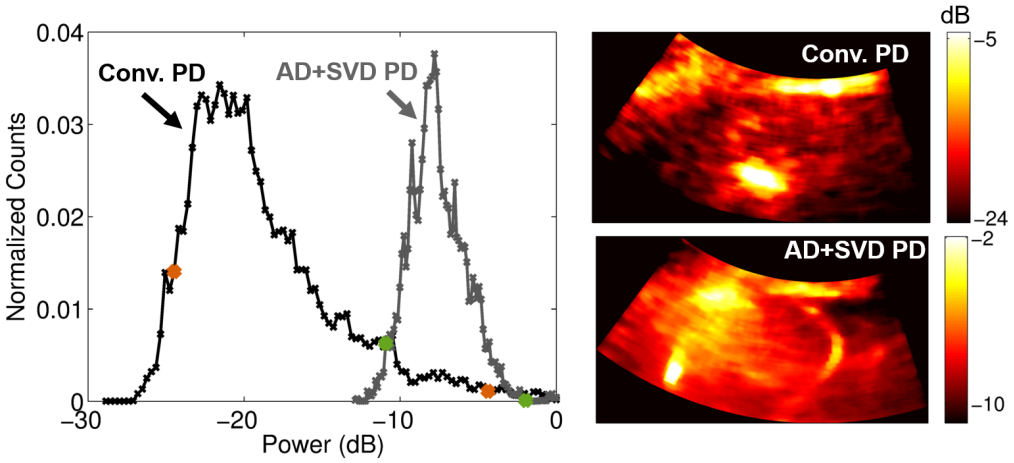

Figure 5.4: Example dynamic range evaluation for subject 9 after TACE. Histograms are shown on the left for power Doppler (PD) images made with conventional methods (black) (i.e., 16-sample ensemble and IIR filtering) and with adaptive demodulation (AD) and SVD filtering (gray). Histograms were made after log compression and scaling to individual maximums. The orange and green dots indicate the dynamic ranges adaptively chosen (middle 70% of the full dynamic range) for the conventional and AD+SVD cases, respectively. Corresponding power Doppler (PD) images are shown on the right on dB scales. PD images were log compressed, scaled to individual maximums, and cropped to the adaptively selected dynamic ranges.

Quantitatively, changes in contrast were highest when using advanced methods. Fig 5.5 shows a box plot of the change in contrast for each processing technique. Except for the conventional method which used a 27ms (16 samples) ensemble size, a 0.5s (300 samples) ensemble size was used for all other methods. The conventional method by itself, with adaptive demodulation, and with the mean phase shift resulted in the smallest changes in median contrast of 0.62dB, 0.03dB, and -0.80dB respectively. Change in contrast is highest when using adaptive demodulation with SVD filtering which resulted in a median change in

contrast of 7.42dB. Adaptive demodulation with IIR filtering resulted in a notable median change in contrast of 4.76dB and also resulted in the highest 75th percentile value. Both of these cases also resulted in statistically significant differences from the conventional method with p-values less than 0.01. All post-hoc power values and t-test p-values are displayed in Table 5.2.

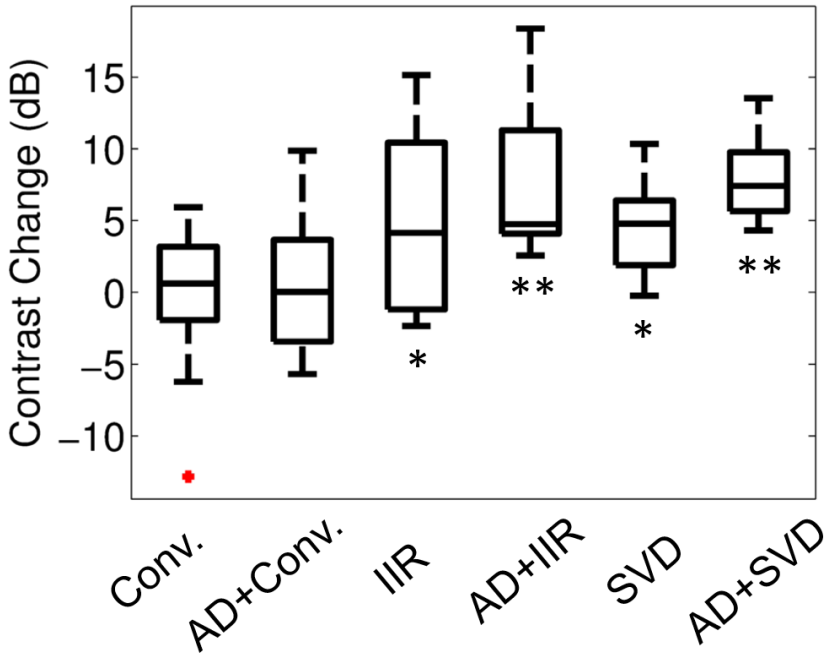

Figure 5.5: Change in tumor-to-background contrast for each processing technique: Conventional (Conv.), adaptive demodulation (AD)+Conv., mean phase shift (MPS)+Conv., IIR, AD+IIR, SVD, AD+SVD. The median value for each method is the central mark in each box. The 25th and 75th percentiles are the bottom and top edges of each box, respectively. The bars extending from each box indicate the minimums and maximums, and outliers are marked in red. Statistically significant differences from the conventional method are indicated with * ($p < 0.05$) and ** ($p < 0.01$).

Compared to standard IIR filtering alone, advanced methods were more robust to varying ensemble sizes. Figs 5.6a and 5.6b show average contrast and average change in contrast, respectively, for each processing method and for ensemble sizes between 27ms and 1s (16 and 600 samples). Before TACE, adaptive demodulation with SVD filtering and SVD by itself produce the highest average contrast for ensemble sizes below 600ms (360 samples), as shown in Fig 5.6a. Adaptive demodulation with conventional IIR filtering pro-

Table 5.2: Post-hoc power estimates and p-values for comparisons between each processing method and the conventional method. Adaptive demodulation and mean phase shift are abbreviated as AD and MPS, respectively.

Method:	**AD+Conv.**	**MPS+Conv.**	**IIR**	**AD+IIR**	**SVD**	**AD+SVD**
power (%)	11.7	6.77	63.5	94.6	81.2	99.3
p-value	0.460	0.651	0.044	0.005	0.017	0.001

duces the highest average contrast for the largest ensemble sizes. After TACE, all methods produce lower average contrast when using ensemble sizes above 0.5s (300 samples), and adaptive demodulation with IIR filtering produces the lowest average contrast overall at a 667ms (400 sample) ensemble size. These trends are supported in Fig 5.6b which shows that adaptive demodulation with SVD filtering produces the highest average change in contrast for smaller ensemble sizes, while adaptive demodulation with IIR filtering produces the largest average change overall when using an 833ms (500 samples) ensemble size. When no tissue filtering is used, the average change in contrast is negative, indicating that there is increased power in the tumor after TACE. This is likely because of lipiodol in the tumors which shows up as bright B-mode structure and would therefore translate to heightened power in an image without adequate tissue filtering. Statistically, the linear model used to fit the data in Fig 5.6b (excluding the no tissue filter data) resulted in an F-statistic corresponding to a p-value less than 0.01, indicating that the model fit the data significantly better than a constant intercept value. Additionally, the model predictors resulted in coefficient values of 11.9, 17.3, 32.4, and 4.57 for SVD (compared to IIR filtering), adaptive demodulation, ensemble size, and the intercept, respectively. These coefficient values suggest that ensemble size is the most important factor in manifesting differences in the change in contrast values from conventional IIR filtering. These values also indicate that adaptive demodulation and SVD filtering strongly influence improvements in changes in contrast values, with adaptive demodulation being more important than SVD.

To support the trends in Figure 5.6 qualitatively, Figure 5.7 shows example power

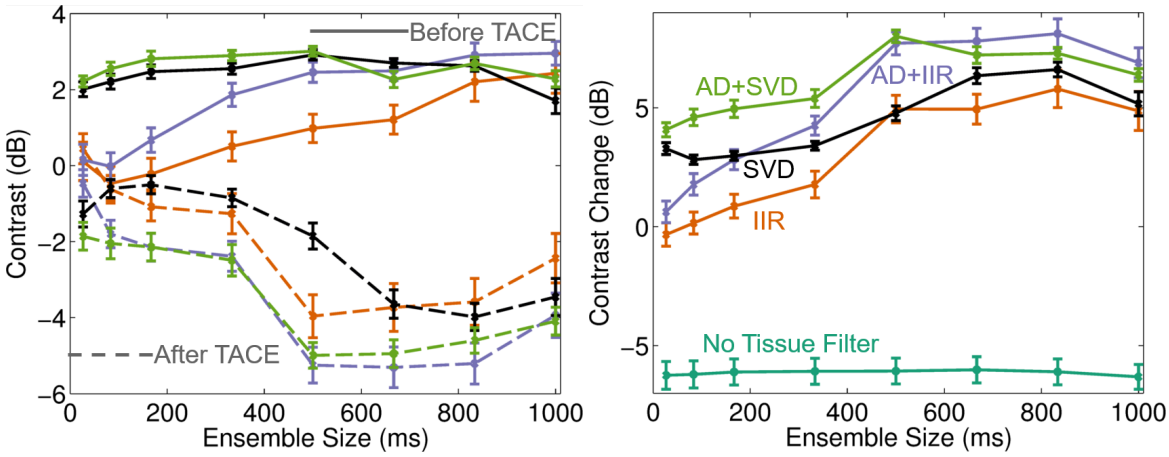

(a) (b)

Figure 5.6: Average contrast (left) and change in contrast (right) for varying ensemble sizes and for each processing method: IIR (orange), adaptive demodulation (AD)+IIR (purple), SVD (black), and AD+SVD (green). On the left, contrast values before and after TACE are shown as the solid and dashed curves, respectively. On the right, change in contrast for when no tissue filtering is used is shown in teal for reference. The no tissue filter values are negative likely because the lipiodol used during TACE is hyperechoic and becomes structure in the tumor.

Doppler images of subject 1 using conventional IIR filtering and using adaptive demodulation with SVD filtering for ensemble sizes of 333ms, 500ms, and 667ms (200, 300 and 400 samples). Before TACE, the power Doppler images made with conventional IIR filtering show minimal signal inside the tumor, while the images made with adaptive demodulation and SVD filtering show enhanced power in the tumor compared to when no tissue filtering is used. After TACE, both methods show suppressed power in the tumor, but IIR filtering fails to suppress all of the signal seen in the SLSC and no filter images. In contrast, the images made with adaptive demodulation and SVD filtering show suppressed signal in the tumor, especially when using the 0.5s (300 samples) ensemble size. Also a clear vessel is seen lining the tumor in the images made with adaptive demodulation and SVD filtering that is not seen in the images made with IIR filtering, no filtering or the SLSC images.

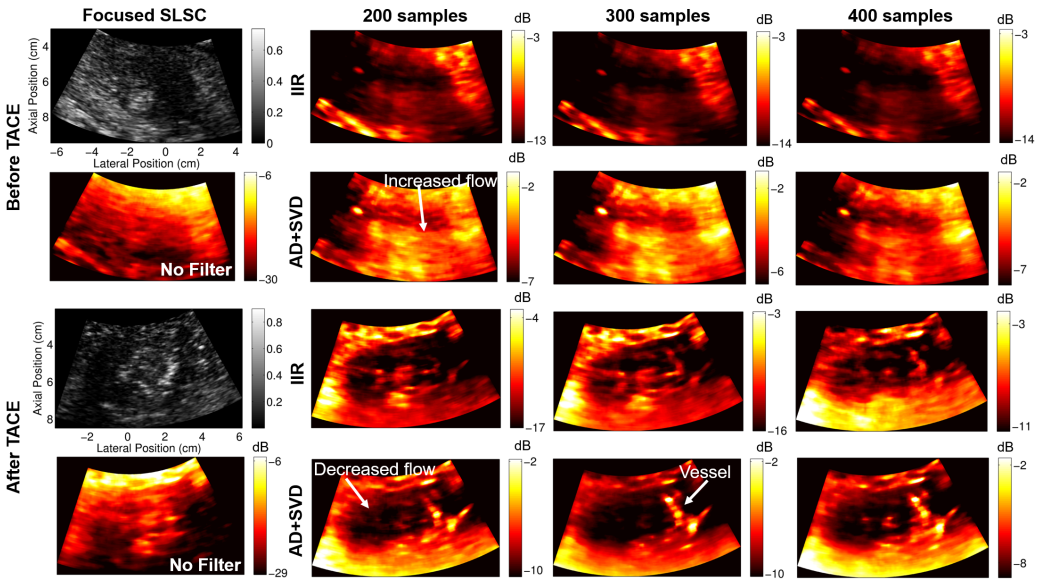

Figure 5.7: Focused SLSC and power Doppler images of subject 1 before TACE (top) and after TACE (bottom). Power Doppler images are made using no tissue filtering, IIR filtering, and with adaptive demodulation (AD) and SVD filtering for ensemble sizes of 200, 300, and 400 samples (333ms, 500ms, and 667ms).

5.4 Discussion

The results demonstrate that adaptive demodulation in combination with advancements in beamforming and filtering can adequately detect changes in perfusion after TACE. More specifically, adaptive demodulation with SVD filtering resulted in the largest median changes in contrast between time points, which is indicative of successful occlusion of the tumor arterial supply. These changes were far less apparent with conventional methods.

Because our conventional method uses synthetic transmit aperture beamforming to focus at all locations in the image, it should have better resolution and SNR than a true conventional power Doppler acquisition implemented with single focus transmits. However, because we use plane waves and acquire our data with a research scanner, we will likely not have SNR that is comparable to what is commercially available. Future studies could incorporate a truly conventional power Doppler scan using a commercial scanner to address this, but the improved SNR that comes from using a clinical platform would also

improve the advanced methods.

The results are supported by previous work that showed the benefit of using adaptive demodulation and SVD compared to IIR filtering alone in simulations, *in vitro* phantom, and preliminary *in vivo* experiments [68, 74]. However, most of those studies tested these techniques at a 7.8MHz imaging frequency and at depths only down to 2.5cm [68, 74]. Here, we show that these methods can be effective at a clinical imaging frequency of 4.2MHz and down to 10cm. Moreover, compared to other studies that have shown the benefit of SVD filtering in fairly stationary and shallow organs like transplanted kidneys [17], we show here that these methods can be successfully applied in the larger and more mobile liver.

In the same previous work, we showed that adaptive demodulation is particularly useful when using smaller ensemble sizes [68], which is what we observed in this work as well. To minimize processing time and facilitate real-time applications, smaller ensemble sizes are preferred. In this work, a 0.5s ensemble size actually produced higher changes in contrast than the full 1s ensemble for most techniques, which could be due to unoptimized filtering or decorrelation effects due to large physiological or sonographer hand motion. Regardless, in this work, a 0.5s ensemble size proved to be the smallest and most effective ensemble size for visualizing both qualitative and quantitative changes in blood flow before and after treatment.

This work intends to showcase initial feasibility of using non-contrast ultrasound as a tool to evaluate TACE. To do this, we made the assumption that treatment was on average successful, which, based on the cited response rate of 62-76% [28, 29], is unlikely. Therefore, the tumor and background ROIs were drawn to avoid potential incomplete response regions in an effort to depict general changes in perfusion. However, there were potential residual tumor or blood flow regions observed in our small pilot study that will need to be confirmed as real or artifact with gold-standard follow-up imaging. Thus, a necessary future study will aim to statistically compare our proposed non-contrast ultrasound technique to CE-MR or CE-CT.

We include preliminary statistics in this work to support the study sample size and to indicate statistically significant differences between each technique and the conventional method. With the proposed combination of adaptive demodulation and SVD, we observed the highest statistical power and significance, suggesting that 11 subjects for an initial pilot study is sufficient.

Non-contrast ultrasound has several advantages over CE-US, CE-MRI, and CE-CT. It is completely noninvasive, more affordable, more accessible, and it is not constrained by time and dose of contrast agents. Additionally, it is not affected by the same treatment-induced imaging artifacts as with CE imaging and could potentially be used immediately after or during the procedure. If non-contrast ultrasound has the potential to have similar if not better performance to these other techniques, it could be an invaluable addition to current treatment evaluation and potentially substantially improve treatment responses.

5.5 Conclusions

Curative treatments are rarely available for hepatic malignancies, and palliative management of these diseases are often necessary with TACE treatment. However, TACE is variably effective and evaluation is limited by late follow-up imaging. We propose non-contrast perfusion ultrasound imaging as a solution for immediate, and potentially intra-procedural, treatment evaluation. We show preliminary feasibility of our proposed technique in a small pilot study. Our results indicate that combining slow flow techniques could potentially make non-contrast perfusion imaging a viable tool for evaluating TACE.

Chapter 6

Developing an Independent Component Analysis-Based Spatiotemporal Clutter Filtering Method for Non-Contrast Slow Flow Ultrasound Imaging

This work is currently in review for publication in IEEE Transactions on Medical Imaging: Tierney, Jaime, et al. "Independent Component-Based Spatiotemporal Clutter Filtering for Slow Flow Ultrasound" *IEEE Transactions on Medical Imaging*.

6.1 Introduction

As discussed in detail in previous chapters, several recent advancements in Doppler processing, beamforming and tissue filtering have been proposed as potential solutions to improve slow blood flow ultrasound imaging. Among these is our proposed time-domain adaptive tissue clutter demodulation technique [54]. Additionally, PCA-based filtering has been extensively considered for optimal tissue filtering [43, 45, 44, 46], and it has been incorporated with other recently proposed slow flow techniques [17, 49, 48, 68].

Independent component analysis (ICA)-based tissue filtering has also been considered and was previously shown to better separate blood from tissue and noise compared to PCA-based filters [44, 75]. However, ICA-based filtering has not been as extensively investigated as PCA-based filtering, and its fundamental limits have yet to be evaluated with other slow flow-focused advancements, like angled plane wave beamforming or adaptive demodulation. Additionally, because it was applied to focused Doppler sequences, its potential as a full spatiotemporal filter has yet to be evaluated. Because ICA assumes statistical independence between components, it should better identify statistically dependent non-gaussian source signals that are uncorrelated and would therefore map to different principal components [76]. In other words, it is possible that tissue, blood, and noise source signals could

be mapped to overlapping principal components (assuming non-gaussian source signals), in which case ICA could provide better delineation [44, 75, 76].

We previously showed that combining adaptive demodulation, angled plane wave beamforming, and adaptive SVD filtering can improve image quality of slow flow [68]. Here, we aim to incorporate a spatiotemporal ICA-based filtering technique with these other slow-flow advancements and compare it to SVD in terms of highest achievable image quality. Compared to our previous preliminary work [77], we aim to more thoroughly describe our ICA implementation and provide more substantial evidence for the benefit of ICA using single vessel phantoms and controlled simulations with ground truth blood signal. Additionally, we propose a novel adaptive blood independent component sorting and selection technique using a correlation-based sorting method and a K-means clustering approach to adaptively separate tissue and blood components. Furthermore, we apply these methods to multiple simulation and phantom realizations at different flow speeds, which extensively expands upon previous work for which we used amplitude thresholding for component sorting and selection and a single phantom realization for validation [78]. Furthermore, we demonstrate initial *in vivo* feasibility using liver tumor data.

6.2 Theory and Implementation

6.2.1 ICA Model

To outline our approach to ICA, we first assume a simple signal model as follows,

$$\mathbf{D} = \mathbf{C} + \mathbf{B} + \mathbf{N} \in \mathbb{R}^{Z \times L \times T} \tag{6.1}$$

where $\mathbf{D}$ is our beamformed RF signal composed of tissue clutter ($\mathbf{C}$), blood ($\mathbf{B}$), and noise ($\mathbf{N}$). $\mathbb{R}^{Z \times L \times T}$ represents the set of real numbers with dimensions Z, L, and T which are the total number of axial, lateral, and temporal samples, respectively. We use only real data for the analyses in this work to simplify the ICA implementation. As in to PCA/SVD

approaches to ultrasound clutter filtering [17, 49], we can reshape $\mathbf{D}$ into a two-dimensional Casorati matrix, $\mathbf{S} \in \mathbb{R}^{M \times T}$, in space and time, where $M = ZL$. PCA techniques work by decomposing $\mathbf{S}$ directly into its corresponding eigenvectors and eigenvalues. ICA generally works by solving for two unknowns, $\mathbf{A} \in \mathbb{R}^{M \times Q}$ and $\mathbf{X} \in \mathbb{R}^{Q \times T}$, related to $\mathbf{S}$ as follows,

$$\mathbf{S} = \mathbf{A}\mathbf{X} \tag{6.2}$$

where $\mathbf{X}$ contains the unmixed source signals, $\mathbf{A}$ is a mixing matrix containing the information for mixing the source signals in $\mathbf{X}$ to produce $\mathbf{S}$, and Q represents the number of independent components. ICA involves two main steps: solving for $\mathbf{A}$ and then using $\mathbf{A}^{-1}$ to solve for $\mathbf{X}$. Many techniques exist for solving for $\mathbf{A}$. For our approach, we use a maximum likelihood (i.e., information maximization) method with BFGS optimization [79, 80, 81].

In our application of ICA, we use a transposed version of $\mathbf{S}$, with dimensions T by M. We also perform an initial dimensionality reduction on $\mathbf{S}^{'}$ to remove noise using SVD and the assumption that noise constitutes the lowest energy eigenvalues [46, 17, 49, 48, 44]. We then perform the optimization on the spatial eigenvectors of $\mathbf{S}^{'}$ only, denoted $\mathbf{Y}$, as described below,

$$\mathbf{S}^{'} = \mathbf{V}\boldsymbol{\lambda}\mathbf{U}^{'} \in \mathbb{R}^{T \times M} \tag{6.3}$$

$$\mathbf{Y} = \boldsymbol{\lambda}\mathbf{U}^{'} = \mathbf{A}\mathbf{X} \in \mathbb{R}^{E \times M} \tag{6.4}$$

where $\mathbf{V} \in \mathbb{R}^{T \times E}$, $\boldsymbol{\lambda} \in \mathbb{R}^{E \times E}$, and $\mathbf{U} \in \mathbb{R}^{E \times M}$ are the temporal eigenvectors, eigenvalues, and spatial eigenvectors of $\mathbf{S}^{'}$, respectively, with noise removed, $\mathbf{A} \in \mathbb{R}^{E \times Q}$ is a square mixing matrix, $\mathbf{X} \in \mathbb{R}^{Q \times M}$ contains the source signals, and $E = Q$ is the number of principal and independent components corresponding to blood and tissue. We perform ICA on the de-noised, spatial eigenvectors to minimize computational burden of the optimization algorithm. After solving for $\mathbf{A}$, we can multiply $\mathbf{A}^{-1}$ by $\mathbf{Y}$ to get $\mathbf{X}$.

Once the independent components are sorted and the principal and independent blood

components are identified, as described in more detail in the following subsections, we can then reconstruct the blood signal as follows,

$$\mathbf{S}'_{blood} = \mathbf{V}^{T\times B_{PC}}\mathbf{A}^{B_{PC}\times B_{IC}}\mathbf{X}^{B_{IC}\times M} \in \mathbb{R}^{T\times M} \tag{6.5}$$

where B_{PC} and B_{IC} are the number of blood principal and independent components, respectively. Finally, we can transpose and reshape $\mathbf{S}'_{blood}$ back to its original dimensions, $\mathbf{B} \in \mathbb{R}^{Z\times L\times T}$.

6.2.2 Independent Component Sorting

Unlike for principal components, which are, by definition, intuitively sorted by descending energy (i.e., tissue should be greater than blood which should be greater than noise), independent component ordering is challenging [76, 82, 83, 84]. For our implementation, we sort according to correlation coefficients computed between reconstructed power Doppler images made with each individual independent component q (PD_q) and a power Doppler image made with all components (PD_Q) as follows,

$$\rho_{sort}(q) = \frac{\sum(PD_Q .* PD_q)}{\sqrt{\sum PD_Q^2}\sqrt{\sum PD_q^2}} \tag{6.6}$$

where PD_Q and PD_q are made by reshaping $\mathbf{V}^{T\times E}\mathbf{A}^{E\times Q}\mathbf{X}^{Q\times M}$ and $\mathbf{V}^{T\times E}\mathbf{A}_q^{E\times 1}\mathbf{X}_q^{1\times M}$ using independent component q only, respectively, back to the original dimensions (Z by L by T) and summing the squared values through slow-time. A power Doppler image made with all components is equivalent to a power Doppler image made with no tissue filtering for which tissue power will dominate since tissue signal is stronger than blood. Therefore, a component that produces a high correlation coefficient likely contains tissue while a component that produces a low correlation coefficient contains blood. An example power Doppler image made with all components and corresponding correlation values are shown in Fig.

6.1. The power Doppler image displayed in Fig. 6.1 has been log compressed and scaled for image quality purposes, but no log compression or scaling was done for the correlation sorting.

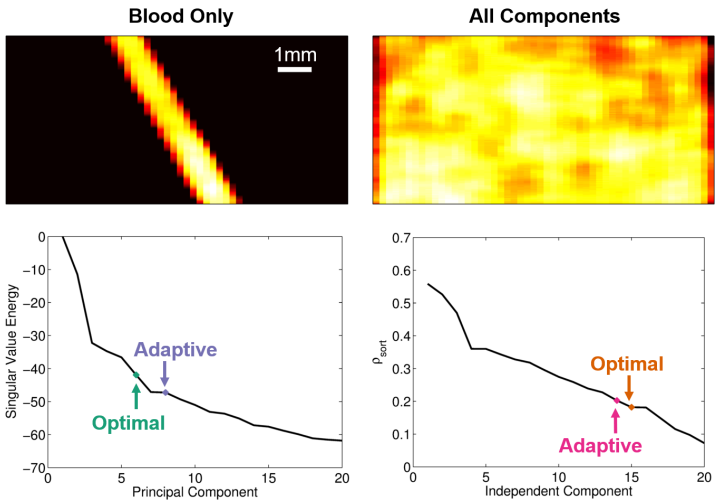

Figure 6.1: Example simulation realization for a 400 sample slow-time ensemble. Power Doppler images shown in the top row are scaled to individual maximums and a 20dB dynamic range. The power Doppler image on the left depicts a case with blood flow only (i.e., no tissue or noise). The power Doppler image on the right shows a case with tissue, blood, and noise with no clutter filtering. The bottom row shows the energy of the singular values for each principal component on the left and the correlation coefficients (as computed in Equation 6.6) for each independent component on the right. Example adaptive and optimal cutoffs are shown for each case (SVD on the left and ICA on the right). A fixed noise cutoff of 20 was used for this example.

6.2.3 Blood Component Selection

Once the independent components are sorted in **AX**, choosing the appropriate cutoff between tissue and blood is also challenging–a problem relevant for principal components as well. To determine whether or not ICA provides any additional benefit to PCA, it is worth comparing the two methods under optimal conditions. However, because it is impossible to determine optimal conditions clinically, adaptively identifying blood components is crucial.

To determine optimal cutoffs, we perform an exhaustive cutoff analysis using simulations and phantoms for which we know ground truth information. For SVD, we choose

whichever cutoff k produces the highest image quality (IQ) correlation coefficient when compared to the blood only power Doppler image (for simulations) or whichever cutoff produces the best blood-to-background signal-to-noise ratio (SNR) image quality metric (for phantoms), as defined in the next section. The correlation coefficient computed for measuring simulation image quality is similar to Equation 6.6 as follows,

$$\rho_{IQ}(k) = \frac{\sum (PD_B . * PD_k)}{\sqrt{\sum PD_B^2}\sqrt{\sum PD_k^2}} \tag{6.7}$$

where PD_B and PD_k are the power Doppler images made using blood only signal and made using principal or independent component k as the starting blood component, respectively. For these power Doppler images, a 2-dimensional spatial median filter, described in more detail in the next section, is applied before computing ρ_{IQ}. Additionally, a Fisher transformation was applied to all ρ_{IQ} values before taking the mean across realizations. An inverse Fisher transformation was then applied to the mean values for quantitative display. An example of a simulated blood only power Doppler image is shown in Fig. 6.1. Again, the blood only power Doppler image displayed in Fig. 6.1 has been log compressed and scaled for image quality purposes, but no log compression or scaling was done for the correlation computation. For ICA, we use the chosen optimal SVD cutoff for the temporal eigenvector principal component filtering and then use whichever independent component cutoff produces the highest ρ_{IQ} or best SNR as described above. For both methods, we use a fixed noise cutoff to restrict variables, as indicated in the next section.

To determine adaptive cutoffs, we perform an initial adaptive eigenvalue thresholding on the principal components. We threshold based on when the slope of the energy of the eigenvalues goes below a certain value, as depicted in Fig. 6.1 [46, 49] and use this as the principal component cutoff for SVD filtering and ICA temporal eigenvector filtering. Then, for the independent components, we perform a 100-iteration K-means clustering on ρ_{sort} (i.e., Equation 6.6) to group the coefficients into 3 groups. Whichever group constitutes the

last independent component is the group identified as blood. K-means could potentially group non-consecutive components, thus providing an additional level of sorting. Example optimal and adaptive cutoffs are depicted in Fig. 6.1.

6.3 Methods

6.3.1 Simulation Data Acquisition

Field II [63] was used to simulate angled plane wave channel data of a 0.6 by 1cm area of tissue scatterers containing a 0.5mm diameter vessel of blood scatterers centered at a 2cm depth. Blood flow was laminar and moved at a peak velocity of 1mm/s. Tissue and blood scatterers were displaced using displacements estimated from 6 different hand motion phantom data sets to generate 6 realistic tissue motion realizations. Tissue, blood and noise channel data were simulated, beamformed, and post-processed separately. Blood and noise channel data were scaled to be 40dB lower than tissue signal.

6.3.2 Phantom Data Acquisition

Eight different phantoms were made using a polyvinyl alcohol and graphite mixture and 1 freeze-thaw cycle. Each phantom had a 0.6mm diameter wall-less vessel within a 2 by 3cm mold. Using a syringe pump, blood mimicking fluid (CIRS Model 046, Norfolk, VA) flowed through each phantom vessel at average velocities of either 1mm/s or 5mm/s. To ensure 6 different realizations for each flow speed, 6 different phantoms were used for each case. A hand held Verasonics L12-5 probe was used to acquire plane wave channel data for each realization for each flow speed.

6.3.3 *In Vivo* Data Acquisition

Plane wave channel data were acquired from a patient with a 4.6cm-diameter hepatocellular carcinoma (HCC) lesion located in segment 2 of the liver right above the portal

vein. HCC tumors are known to be highly vascularized and perfusion characteristics are used for treatment and diagnosis [30]. Informed written consent in accordance with Vanderbilt's Institutional Review Board was obtained from the patient prior to the start of the acquisition. Using a Verasonics C5-2 probe, an interventional radiologist acquired 167ms of angled plane wave channel data.

6.3.4 Beamforming

Channel data were acquired at a 7.8MHz transmit center frequency for the simulation and phantom experiments and a 4.2MHz transmit center frequency for the *in vivo* data. For all experiments, 9 angled plane waves evenly spaced between -8° and 8° were transmitted at pulse repetition frequencies (PRF) of 9kHz for 1s (simulation and phantom) or 5.4kHz for 167ms (*in vivo*). Channel data were beamformed using parallel receive beamforming and consecutive angles were summed to synthesize transmit focusing, resulting in final PRFs of 1kHz (simulation and phantom) and 600Hz (*in vivo*) [39] and ensemble sizes of 1000-samples (simulation and phantom) and 100-samples (*in vivo*). Hann apodization and aperture growth to achieve an F/# of 2 were implemented during receive beamforming. Beamformed data were band-pass filtered after being up-sampled by factors of 2 and 3 to achieve sampling frequencies of 62.5MHz (simulation and phantom) and 50MHz (*in vivo*). Additionally, for *in vivo* anatomical reference, immediately prior to the acquisition of the plane wave scan, a conventional focused scan was acquired at 6cm.

6.3.5 Post-Processing

Adaptive demodulation was applied to each data set using the implementation described in Tierney et al. [54]. An axial kernel size of 10λ and a slow-time lag of 1 sample (i.e., 1.7ms for *in vivo* data and 1ms for all other data) were used to compute relative and total displacements, respectively, for the phase demodulation. Amplitude demodulation was not used.

Ensemble sizes between 20 samples (20ms) and 1000 samples (1s) were used for tissue filtering and power Doppler estimation for each simulation and phantom data set. The full ensemble size of 100 samples (167ms) was used for the *in vivo* example. SVD and ICA tissue filtering were implemented as described in the previous section using 20, 30, 40, and 47 as the principal component noise cutoff for the simulations, 1mm/s phantom data, 5mm/s phantom data, and *in vivo* data, respectively (i.e., $E = 20$ or $E = 30$ or $E = 40$ or $E = 47$). For the phantom data, a noise cutoff of 20 was used for the 20 sample ensemble. For the *in vivo* data, the noise cutoff was adaptively chosen by fitting a line to the right half of the eigenvalue curve and determining at which component the eigenvalues deviate from the line by a threshold of 0.01 [49].

Power Doppler was computed using $PD(z,x) = \sum_{t=1}^{T} d(z,x,t)^2$ for each beamformed and filtered data set. A 1mm by 1mm spatial median filter was applied to each power Doppler image for the simulations and phantoms. A 2mm by 2mm spatial median filter was applied to the *in vivo* power Doppler images. For simulated data, correlation coefficients (compared to blood only power Doppler, i.e., ρ_{IQ}) were computed as in Equation 6.7. For simulation and phantom data, blood-to-background SNR, contrast-to-noise ratio (CNR) and generalized contrast-to-noise ratio (GCNR) [70] were computed as follows,

$$SNR = 10log_{10}\frac{\frac{1}{N}\sum_{i=1}^{N} PD_{sig}(i)}{\frac{1}{M}\sum_{i=1}^{M} PD_{bkgd}(i)} \tag{6.8}$$

$$CNR = 10log_{10}\frac{|\frac{1}{N}\sum_{i=1}^{N} PD_{sig}(i) - \frac{1}{M}\sum_{i=1}^{M} PD_{bkgd}(i)|}{STD(\frac{1}{M}\sum_{i=1}^{M} PD_{bkgd}(i))} \tag{6.9}$$

$$GCNR = 1 - OVL \tag{6.10}$$

where N and M are the total number of pixels in the vessel and background, respectively, PD_{sig} and PD_{bkgd} are the power Doppler values in the vessel and background, respectively, STD stands for the standard deviation, and OVL represents the overlap between histograms of the background and vessel pixels. The entire region outside of the simulation or phantom

vessel was considered as background. Power Doppler images were made by log compressing the power Doppler signal ($I = 10log_{10}PD(z,x)$). Images were scaled to individual maximums and dynamic ranges were chosen by computing the average power value of the background pixels for each image. This value was used as the minimum value in the image. For the *in vivo* data, the full dynamic range was used for image display.

6.3.6 Optimal Blood Component Selection

For computing optimal image quality metrics, simulation and phantom data were filtered using tissue cutoffs between 1 and E for SVD and between 1 and Q for ICA for each realization and ensemble. When reconstructing power Doppler images with ICA, a fixed principal component cutoff was used for temporal eigenvector filtering. As described in the previous section, for simulations, the principal component cutoff that produced the highest SVD ρ_{IQ} (Equation 6.7) was used as the cutoff for temporal eigenvector filtering. For phantoms, the principal components that produced the highest SVD SNR was used for temporal eigenvector filtering.

6.3.7 Adaptive Blood Component Selection

As described in the previous section, the cutoff between tissue and blood principal components was chosen by computing when the slope of the eigenvalues goes below a certain threshold. The same threshold was used for all ensemble sizes for each filter case (SVD, adaptive demodulation+SVD, ICA, adaptive demodulation+ICA). Thresholds of 2 and 3 were used for determining the principal component cutoff between tissue and blood for simulated data with and without adaptive demodulation, respectively. Thresholds of 1 and 3 were used for the 1mm/s phantom data with and without adaptive demodulation, respectively. A threshold of 0.5 was used for all of the 5mm/s phantom data. A threshold of 0.25 was used for the *in vivo* data.

To determine the independent component cutoff between tissue and blood, a K-means

clustering was performed and is described in more detail in Section 6.2.3. Additionally, for the *in vivo* data, the noise principal component cutoff was chosen adaptively as described in Section 6.3.5.

6.4 Results

6.4.1 Simulations

The simulation results demonstrate that ICA can remove tissue clutter better than SVD by itself both optimally and adaptively for all ensemble sizes tested. Fig. 6.2 shows the optimal and adaptive results for an example realization using a 400-sample ensemble with adaptive demodulation applied. For this example, the adaptive SVD eigenvalue thresholding approach chose the cutoff that produced the highest achievable correlation to the blood only power Doppler image. The same was not true for ICA, but the adaptive K-means approach chose a cutoff that was reasonably close to the optimal cutoff. Both the optimal and adaptive ICA power Doppler images show better clutter suppression and more uniform flow through the vessel than the SVD case.

These qualitative results are supported quantitatively in Figs. 6.3 and 6.4. Fig. 6.3 shows the correlation coefficients (ρ_{IQ}) computed for each ensemble size for optimal and adaptive ICA and SVD both with and without adaptive demodulation. Optimal ICA produces correlation coefficients that are consistently higher than optimal SVD both with and without adaptive demodulation. Adaptive demodulation provides an additional benefit to optimal ICA for smaller ensemble sizes which is consistent with previous work [68]. Adaptive ICA also produces correlation coefficients that are higher than adaptive SVD. Adaptive demodulation provides a benefit to adaptive SVD but does not produce the same improvements for adaptive ICA. Adaptive ICA also produces correlation coefficients that are higher than optimal SVD for larger ensemble sizes, as shown in the plot overlaying both optimal and adaptive results.

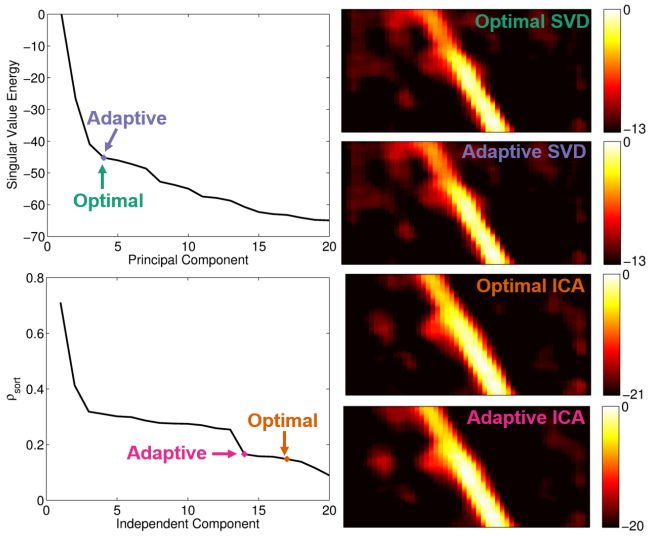

Figure 6.2: Optimal and adaptive simulation results for a single realization using a 400-sample ensemble and adaptive demodulation. Singular values are shown for each principal component in the top left. The optimal and adaptively selected principal component cutoffs are indicated in teal and purple, respectively, and are equivalent for this case. Correlation coefficients for each independent component (Equation 6.6) are shown in the bottom left plot. Optimal and adaptively selected independent component cutoffs are indicated in pink and orange, respectively. Corresponding optimal and adpative SVD and ICA power Doppler images are shown on the right on dB scales.

Fig. 6.4 shows the image quality results for the optimal and adaptive ICA and SVD approaches with and without adaptive demodulation. Similar to the correlation coefficients, optimal ICA produces higher SNR, CNR, and GCNR than optimal SVD. The same is true for adaptive ICA compared to adaptive SVD. Also, adaptive demodulation seems to improve optimal ICA image quality for smaller ensemble sizes but has little effect for adaptive ICA.

6.4.2 Phantoms

Similar to the simulation results, ICA is shown to produce superior image quality compared to SVD with the 1mm/s and 5mm/s phantom data both optimally and adaptively. Fig. 6.5 shows results for a single 1mm/s phantom data set using a 400-sample ensemble. Adaptive demodulation was not used for this example. Similar to Fig. 6.2, the adaptive

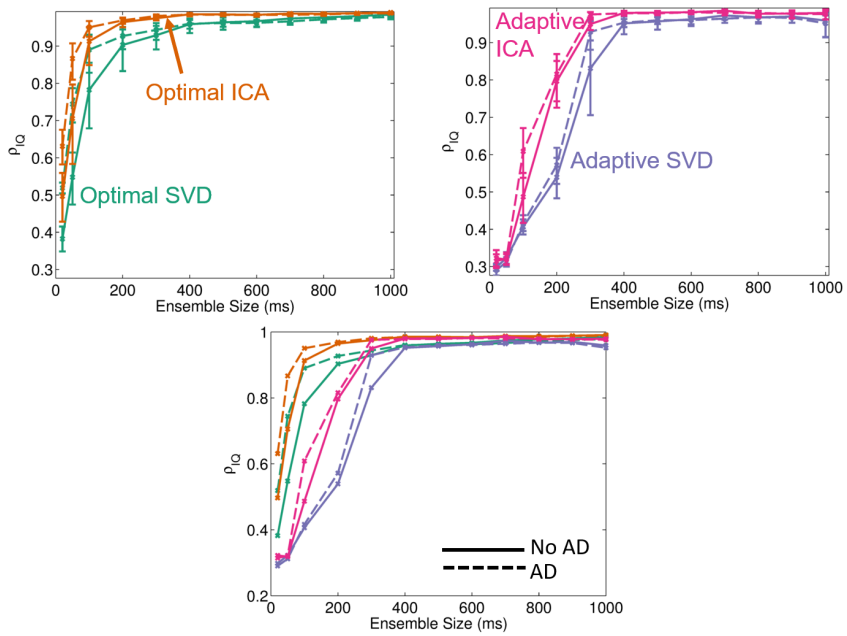

Figure 6.3: Simulated average correlation coefficients computed using Equation 6.7 are shown for ensemble sizes between 20 and 1000-samples (i.e., 20ms and 1s). Optimal and adaptive results are shown in the top left and right, respectively. Error bars indicate standard error. The plot on the bottom has both optimal and adaptive results without error bars for visualization purposes. Dashed curves indicate results with adaptive demodulation.

SVD approach chose the tissue cutoff that produces optimal SNR, therefore the adaptive and optimal SVD power Doppler images are the same. The adaptive ICA method did not result in the same tissue cutoff that produces optimal SNR, but it did result in a cutoff that produces an image that has arguably better background suppression than the optimal case. The optimal ICA image has brighter blood pixels and more uniform flow across the vessel laterally than the adaptive ICA image, but the tissue clutter below the vessel is suppressed better with adaptive ICA. Additionally, both the adaptive and optimal ICA images demonstrate better tissue clutter suppression than the optimal and adaptive SVD image.

Similar qualitative conclusions can be made for the 5mm/s phantom example shown in Fig. 6.6 for a 400-sample ensemble with adaptive demodulation. For this case, the adaptive SVD approach chose a tissue cutoff that does not produce exactly optimal SNR, but produced very close to optimal image quality. Similarly, adaptive ICA did not choose

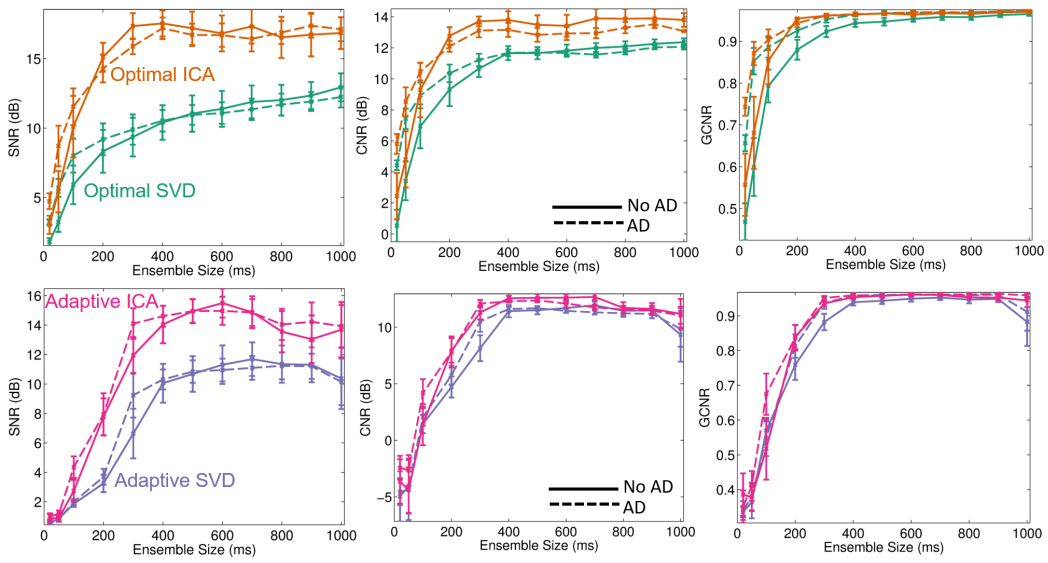

Figure 6.4: Simulated average SNR (left), CNR (middle), and GCNR (right) are shown for ensemble sizes between 20 and 1000-samples (i.e., 20ms and 1s). Optimal ICA (orange) and optimal SVD (teal) are shown in the top row. Adaptive ICA (pink) and adaptive SVD (purple) are shown in the bottom row. Error bars indicate standard error. Dashed curves indicate results with adaptive demodulation.

an optimal tissue cutoff, but it produced image quality that is very similar to the optimal ICA case. The ICA and SVD images for this case are similar, but ICA produces more uniform flow throughout the vessel. Although subtle, the improvement with ICA is not insignificant, especially for low SNR small vessel environments.

Optimal and adaptive ICA produced higher SNR, CNR, and GCNR for most ensemble sizes compared to optimal and adaptive SVD, respectively, as shown in Figs. 6.7 and 6.8 for both phantom data sets. For the 1mm/s phantom data, GCNR is higher when using SVD for the smallest ensemble sizes. This is likely because of no flow being detected in the vessel, which would result in a clear separation between bright tissue clutter in the background region and dark blood signal in the vessel. GCNR as we have implemented it does not account for negated trends. For both phantom cases and for both optimal and adaptive ICA, adaptive demodulation provides an additional benefit in SNR and GCNR for most ensemble sizes, which differs from what was seen in simulations. This trend is less

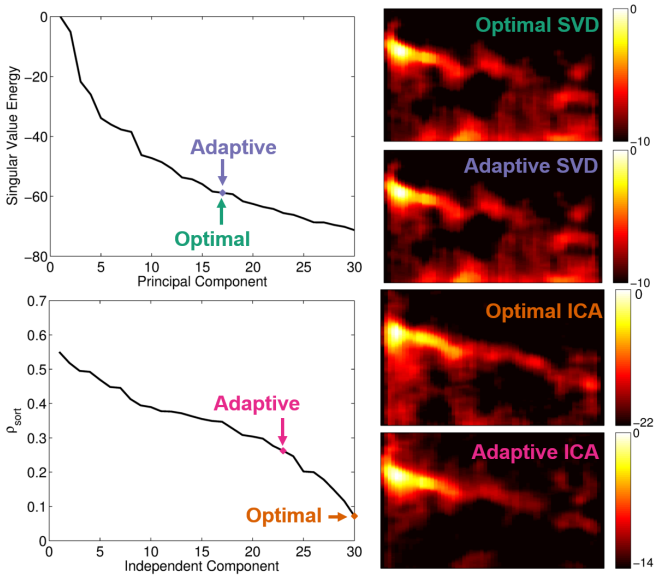

Figure 6.5: Optimal and adaptive 1mm/s phantom results for a single realization using a 400-sample ensemble. Adaptive demodulation was not used for this example. Singular values are shown for each principal component in the top left. The optimal and adaptively selected principal component cutoffs are indicated in teal and purple, respectively, and are equivalent for this case. Correlation coefficients for each independent component (Equation 6.6) are shown in the bottom left plot. Optimal and adaptively selected independent component cutoffs are indicated in pink and orange, respectively. Corresponding optimal and adpative SVD and ICA power Doppler images are shown on the right on dB scales.

apparent for CNR, but adpative ICA does appear to be less susceptible to outliers when adaptive demodulation is used, as seen in the adaptive CNR plots in Figs. 6.7 and 6.8

Although the adaptive ICA approach does not produce the same image quality as optimal ICA, it does produce better image quality than optimal SVD for larger ensemble sizes. This was demonstrated in Fig. 6.3, and is also supported in Fig. 6.9 which overlays all SNR results for varying ensemble sizes for the simulations, 1mm/s phantom data, and 5mm/s phantom data. The improvement with adaptive ICA is most apparent with the simulation and 1mm/s phantom data.

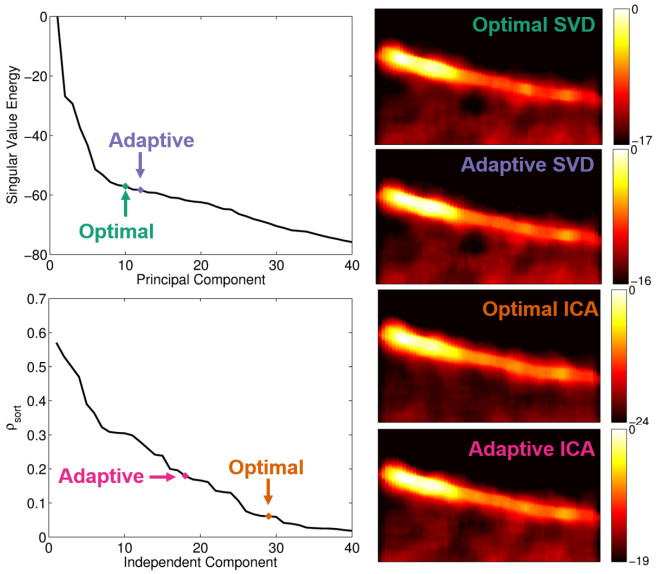

Figure 6.6: Optimal and adaptive 5mm/s phantom results for a single realization using a 400-sample ensemble with adaptive demodulation. Singular values are shown for each principal component in the top left. The optimal and adaptively selected principal component cutoffs are indicated in teal and purple, respectively. Correlation coefficients for each independent component (Equation 6.6) are shown in the bottom left plot. Optimal and adaptively selected independent component cutoffs are indicated in pink and orange, respectively. Corresponding optimal and adpative SVD and ICA power Doppler images are shown on the right on dB scales.

6.4.3 *In Vivo*

To demonstrate *in vivo* feasibility, adaptive SVD and ICA were applied to data of a HCC tumor in the liver. Fig. 6.10 shows example focused B-mode, angled plane wave B-mode, and power Doppler images made with no filtering, adaptive SVD and adaptive ICA. Compared to the image with no tissue filtering, adaptive SVD and ICA both show clear vessel structures that are not seen in the B-mode images. Although subtle, ICA does show improvements in clutter suppression and vessel SNR. Additionally, the ICA image shows small vessel structure that is not as clear in the SVD image, as indicated in the image labels.

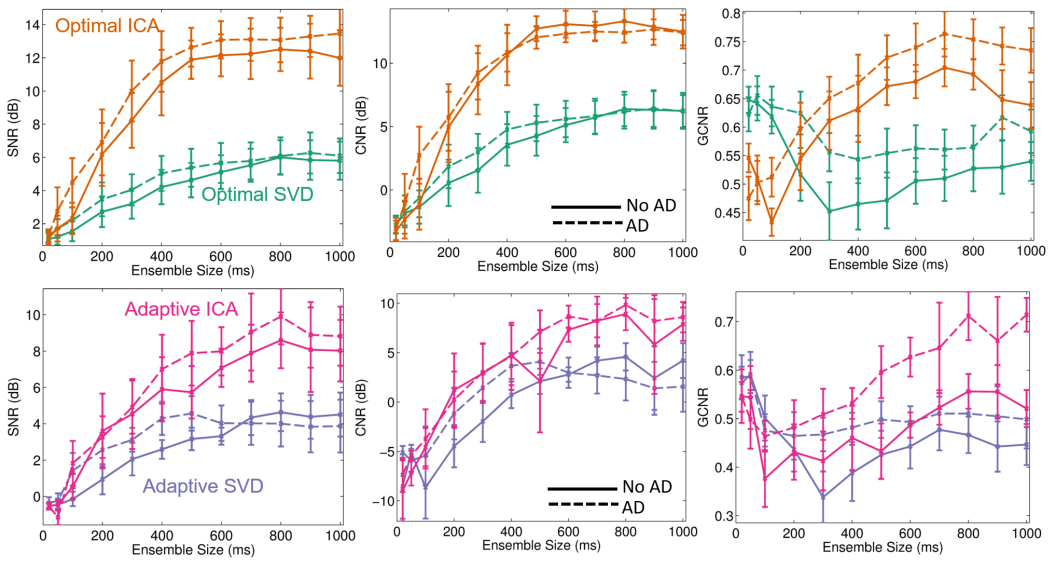

Figure 6.7: Average SNR (left), CNR (middle), and GCNR (right) are shown for ensemble sizes between 20 and 1000-samples (i.e., 20ms and 1s) for the 1mm/s phantom data. Optimal ICA (orange) and optimal SVD (teal) are shown in the top row. Adaptive ICA (pink) and adaptive SVD (purple) are shown in the bottom row. Error bars indicate standard error. Dashed curves indicate results with adaptive demodulation.

6.5 Discussion

The exhaustive search for optimal tissue cutoffs demonstrates the achievable benefit of ICA-based filtering compared to SVD by itself. In all simulation and phantom experiments, ICA produced the highest optimal SNR, CNR, and GCNR overall as well as the most qualitatively compelling images of tissue clutter suppression. Although it is meaningful that ICA produces the highest values across multiple image quality metrics, it is difficult to draw definitive conclusions based on these metrics due to their inherent biases and differences [70, 68]. We address this concern by making use of controlled simulations with which we were able to compare filtered images to ground truth blood signal. The correlation coefficients computed against this ground truth signal provide more substantial evidence for the potential benefit of ICA-based filtering compared to SVD by itself.

This work is the first to assess ICA-based filtering using ground truth simulations in combination with other slow flow ultrasound advancements, including angled plane wave

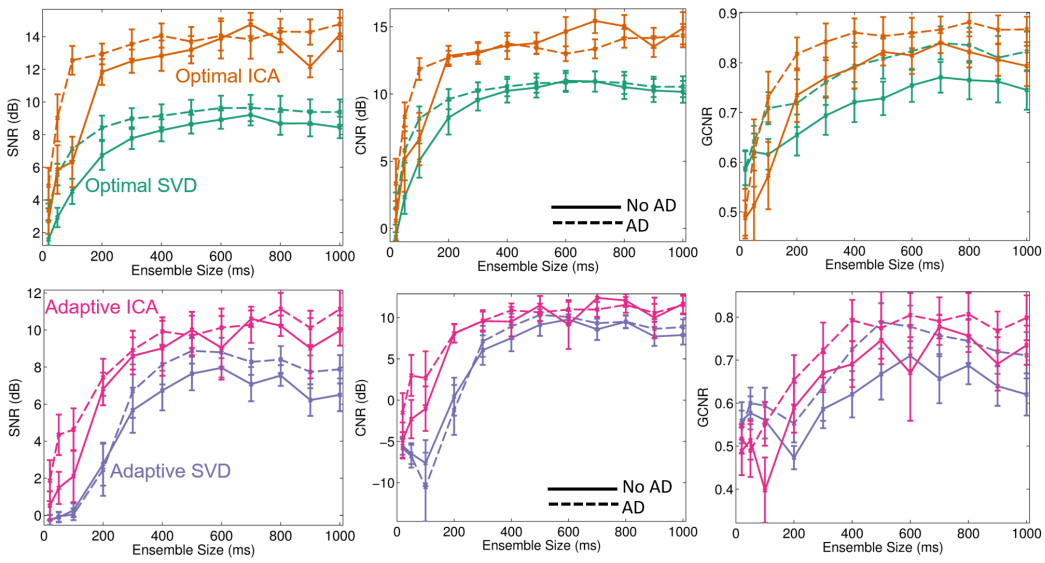

Figure 6.8: Average SNR (left), CNR (middle), and GCNR (right) are shown for ensemble sizes between 20 and 1000-samples (i.e., 20ms and 1s) for the 5mm/s phantom data. Optimal ICA (orange) and optimal SVD (teal) are shown in the top row. Adaptive ICA (pink) and adaptive SVD (purple) are shown in the bottom row. Error bars indicate standard error. Dashed curves indicate results with adaptive demodulation.

beamforming and adpative demodulation. Compared to conventional Doppler beamforming, plane wave sequences have enabled much longer ensembles to be achieved while maintaining reasonable frame-rates. The results in this work demonstrate the benefit of long ensembles for both ICA and SVD filtering, as shown with ground truth correlation estimates as well as image quality metrics. Similar to conclusions made in previous work [68], the metrics evaluated in this manuscript appear to plateau at larger ensembles, which could be indicative of a fundamental limit or an unaccounted for source of decorrelation. However, fixed noise cutoffs were used for both simulations and phantoms which could also explain the plateau, assuming the noise cutoff does not apply equally well to all ensemble sizes. Future work will aim to incorporate adaptive noise filtering in addition to the adaptive ICA and SVD techniques used in this work.

Although adaptive demodulation provided minimal benefit to the simulated image quality metrics, it did result in small improvements in the simulation correlation estimates for

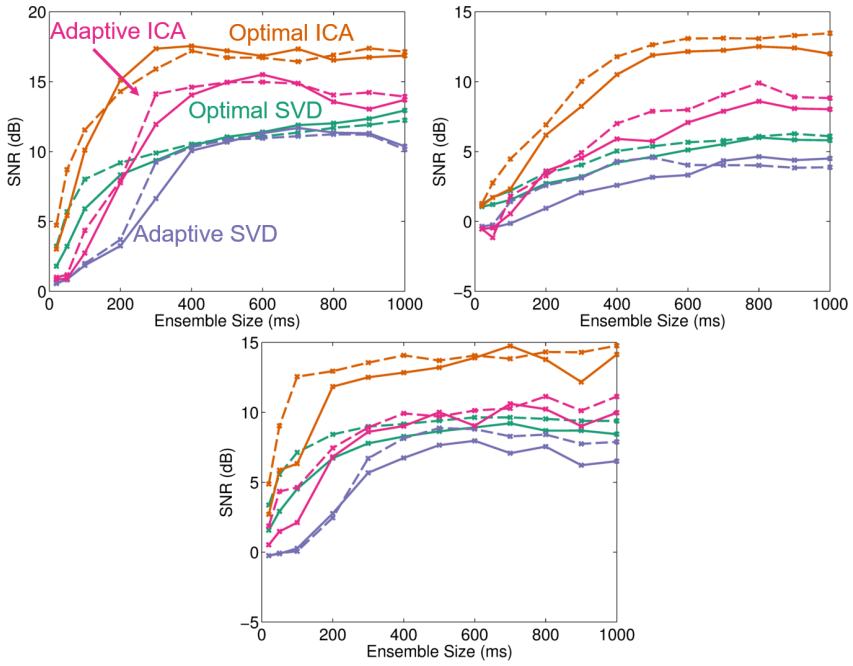

Figure 6.9: Average SNR for varying ensemble sizes is shown for simulations (top left), 1mm/s phantom data (top right) and 5mm/s phantom data (bottom). SNR produced using optimal ICA (orange), adaptive ICA (pink), optimal SVD (teal), and adaptive SVD (purple) are shown on each plot. Dashed curves indicate results with adaptive demodulation.

the optimal ICA approach at the smallest ensembles, which is also consistent with previous work [68]. However, based on the correlation estimates in Fig. 6.3, adaptive demodulation appears to improve both optimal and adaptive SVD filtering more so than ICA in simulations. That said, adaptive demodulation did provide more consistent improvements to both optimal and adaptive ICA in the 1mm/s and 5mm/s phantom data. This could perhaps be due to more tissue motion being present in the phantom data than the simulations for which adaptive demodulation would be more useful.

Although it was useful to compute highest achievable metrics to determine the true potential of each technique, it is not practical or possible *in vivo*. In this work we propose a novel adpative K-means clustering approach in combination with simple singular value thresholding to adaptively select blood independent and principal components, respectively. The simulation and phantom results demonstrate that adaptive ICA can produce

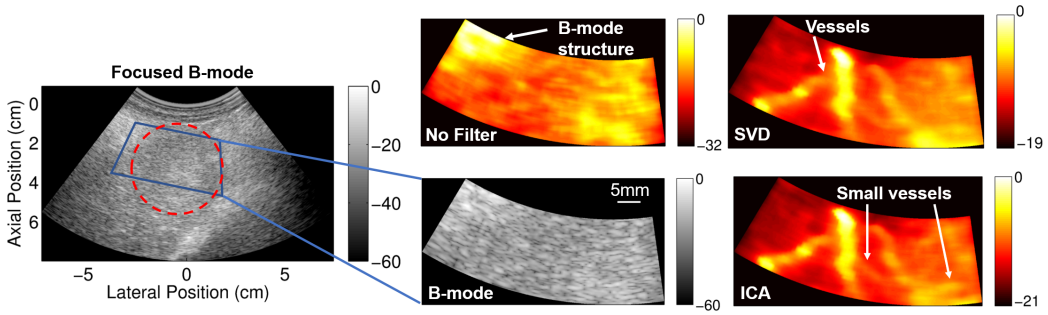

Figure 6.10: *In vivo* data of a HCC tumor in the liver. A full field of view focused B-mode image is shown on the left. The tumor is outlined in red and the field of view used to make power Doppler images is outlined in blue and indicated by the angled plane wave B-mode image in the bottom left. Power Doppler images were made using a 100-sample ensemble with no tissue filtering (top left), adaptive SVD filtering (top right) and adaptive ICA filtering (bottom right). Adaptive demodulation was not used for this example. All images are on a dB scale.

higher metrics than adpative and, for larger ensembles, optimal SVD. Additionally, the *in vivo* example supports these conclusions and shows improvements in small vessel visualization with adaptive ICA filtering compared to adaptive SVD. Although effective for the purposes of this work, the eigenvalue thresholding technique is likely not optimal for determining blood principal components. Several more advanced adaptive SVD approaches that also incorporate noise filtering have been proposed [49, 69] that would likely improve the adaptive SVD metrics. However, our results suggest that adaptive ICA will similarly benefit from these more advanced principal component cutoff techniques.

Finally, as mentioned previously, there are many ICA methods that exist. In this work we used an information maximization approach [79, 80, 81], and previously Gallippi and Trahey used the joint approximation diagonalization of eigen-matrices (JADE) algorithm [44, 75]. Other methods, including fourth-order blind identification (FOBI) and fast ICA, should also be evaluated to determine which is best suited for the spatiotemporal clutter filtering application. Additionally, input dimensionality should also be considered. For our implementation we perform ICA on the spatial eigenvectors. It is worth investigating further how ICA performs on temporal eigenvectors or if there is value in combining both

spatial and temporal eigenvector ICA filtering. Without these analyses, it is possible that the true potential of ICA has yet to be realized.

6.6 Conclusion

ICA was previously considered for ultrasound tissue filtering, but it has not been revisited since the proposal of recent slow flow-focused advancements. Additionally, controlled simulations with ground truth blood signal have not been previously used for determining the fundamental potential of both SVD and ICA. Furthermore, adaptive independent component sorting and selection has not been previously proposed or investigated for the purposes of ultrasound slow blood flow imaging. We address these shortcomings by developing a spatiotemporal ICA-based filtering technique using angled plane wave beamforming and evaluate it in comparison to the well-known SVD filter. We show that optimal and adaptive ICA can produce image quality metrics that are superior to optimal and adaptive SVD across varying ensemble sizes using simulations and phantom data. Furthermore, we demonstrate initial *in vivo* feasibility in a liver tumor data set.

Chapter 7

Conclusion and Future Work

Transarterial chemoembolization (TACE) treatment of liver tumors aims to reduce tumor perfusion and therefore relies on accurate perfusion imaging to evaluate treatment response. Although effective, contrast-enhanced imaging modalities suffer from treatment-induced artifacts that necessitate late follow-up imaging, typically 4-6 weeks post-treatment. The inability to assess treatment adequacy in real-time is a potential reason for lack of treatment response. Non-contrast perfusion ultrasound is a potential solution to this problem. However, perfusion ultrasound imaging without contrast is difficult for several reasons. Without contrast enhancement, blood ultrasound signal is weak compared to tissue signal, and, because perfusion occurs in the smallest, most randomly oriented vessels, perfusion blood signal is particularly difficult to detect. Therefore, SNR-enhancing and angle independent power Doppler techniques in combination with adequate tissue filtering is critical. Perfusion blood velocity is also slow and comparable to tissue motion caused by patient and sonographer hand motion. This causes a spectral overlap in the slow-time frequency domain which is conventionally used for separating and removing tissue signal. There is also evidence that this motion causes an overlap in the eigen-domain [48], affecting more advanced principal component analysis (PCA)-based tissue filtering methods. Therefore, despite advances in Doppler processing, beamforming, and tissue filtering, tissue clutter interference with blood has remained a barrier for realizing non-contrast perfusion ultrasound imaging for real-time TACE treatment evaluation.

This dissertation has demonstrated the potential of an adaptive time-domain tissue clutter demodulation scheme to address this problem and potentially allow for velocities to be detected that were previously thought to be impossible to visualize without contrast agents. The technique was validated, improved upon, and successfully applied to prelim-

inary TACE data. Additionally, an independent component analysis (ICA)-based tissue clutter filtering method was developed and integrated with other advancements, including the adaptive demodulation method, and was shown to be superior to PCA-based techniques. Furthermore, this work is the first to demonstrate that Doppler methods without contrast agents can detect changes in blood flow in unresolvable vessels. Although the work presented in this dissertation has provided substantial evidence for the possibility of perfusion ultrasound imaging without contrast to be used as an early TACE treatment evaluation tool, a few limitations still exist that should be addressed with future work.

The proposed adaptive demodulation technique was developed and validated through the use of simulation, phantom, and *in vivo* proof-of-concept experiments. As part of this work, a novel two-part phase and amplitude demodulation was proposed, and the presented results were the first to explicitly and quantitatively demonstrate that it is possible to achieve ultrasound velocity estimates that are an order of magnitude lower than previously deemed possible without contrast [14, 54]. Although broadly impactful, the developed technique could be improved. Specifically, the amplitude demodulation worked well for the initial experiments, but it did not provide substantial improvements for later work. This could in part be due to not having a logical way to optimize the size of the temporal median filter. For later work, we implemented a 35-sample median filter because that was what we found worked well for our initial work, but it is possible that this size needs to be reconsidered and tested for each individual experiment, making adaptation to different applications difficult. Another way to potentially solve this amplitude fluctuation problem would be to implement a lateral displacement estimation and correction using techniques like transverse oscillation [85] or 2-dimensional normalized cross correlation [86]. Additionally, estimating slow-time coherence, as was implemented for contrast-enhanced methods [87], could potentially aid in differentiating between tissue and blood and provide a better way to optimize the median filter length. Although more computationally expensive, incorporating methods like these could account for lateral and elevational motion more effectively and potentially

provide more complete tissue clutter suppression.

Adaptive demodulation combined with other slow flow-focused advancements (i.e., angled plane wave beamforming, coherent flow power Doppler (CFPD) beamforming, and singular value decomposition (SVD) filtering) was shown to improve slow flow detection in simulation and phantom experiments. This work is a valuable contribution to the field because it is the first to compare and combine these techniques, providing insight as to when each is most beneficial to use. Also, it is the first to evaluate these techniques using controlled simulations and phantoms with vessel sizes and blood velocities that are within range of perfusion-feeding vessels, like venules and arterioles. However, there are opportunities for improving these studies. As part of this work, adaptive demodulation parameters were optimized, but these experiments could have been more exhaustive. For example, throughout this dissertation, angled plane wave sequences used 9 angles spaced evenly between -8° and 8°. This sequence design has worked well for the purposes of the work presented in this dissertation, but other research in the lab has suggested that smaller angle spacing might be better for coherence-based beamforming methods, which could have affected the CFPD comparisons in Chapter 4. Similarly, it is possible that smaller or larger angle spacing or ranges could affect the performance of adaptive demodulation. Additionally, the experiments in Chapter 4 used single vessel simulations and phantoms, which we know are not realistic representations of perfusion environments. It would be valuable to repeat these studies in the future using perfusion-mimicking phantoms that are being developed in the lab. Finally, the work in Chapters 4 and 6 consistently show a plateau in image quality metrics with larger ensemble sizes. We have speculated that this could be due to decorrelation effects, noise artifacts, or possibly a fundamental limit. Future work is necessary to determine the true cause of this trend.

Initial evidence was shown to suggest that by incorporating adaptive demodulation with other slow-flow advancements, non-contrast perfusion ultrasound imaging could be used as an early and potentially real-time TACE treatment evaluation tool, which, to reiterate,

would be an invaluable tool for improving patient outcomes. This study showed initial feasibilty and promising results for potential clinical use. Apart from the clinical value of this work, because TACE involves spatial and temporal changes in perfusion in tumors at varying depths, this study also demonstrated the unique experimental value of TACE for testing slow flow ultrasound techniques. However, as mentioned previously, necessary future work will need to include confirmed patient outcomes with gold-standard follow-up CT or MRI imaging. Additionally, a larger sample size will be necessary to generate meaningful statistics to support clinical adoption. Furthermore, the pilot study presented in this dissertation used parameters for beamforming, adaptive demodulation and SVD filtering that worked well but were likely not optimal. For example, previous work determined that a 10λ kernel size worked well for relative displacement estimation for the adaptive demodulation method. However, this was determined using single vessel simulation data with a higher transmit center frequency. Therefore, it is possible that this value and other parameters should be better optimized for future TACE data evaluation.

Finally, in addition to the proposed adaptive demodulation technique, this dissertation summarizes early work developing and validating an ICA-based tissue clutter filtering method to further improve ultrasound detection of perfusion-level blood flow without using contrast agents. This work is the first to propose ICA as a full spatiotemporal filter facilitated by plane wave beamforming. Additionally, this work is the first to evaluate SVD and ICA using ground truth blood signal, made possible by controlled simulations. This effort is valuable because it addresses the ongoing concern among researchers in the field about the inherent biases of image quality metrics, including SNR, CNR, and GCNR [70]. Although this work demonstrated the value of ICA, it is preliminary, and there is valuable future work that should be pursued. Because ICA has so many variables, including the method used to solve for an appropriate mixing matrix, necessary future work will need to evaluate and provide mathematical reasoning for which method is best suited for the perfusion ultrasound imaging problem. Additionally, as part of this work, an initial adap-

tive approach was proposed for sorting and selecting blood independent components. This approach is likely not optimal and future studies should be conducted to determine the best sorting and selection methods for ICA. Furthermore, ICA was performed only on spatial eigenvectors. This sets the stage for evaluating the temporal dimension as well as a combination of both dimensions. Finally, for most of the work with SVD and ICA, small fields of view were used for the single vessel simulations and phantoms which enabled global implementations. However, block-wise approaches that are currently being developed in the lab will likely provide substantial improvements to these methods for *in vivo* TACE data.

The work proposed in this dissertation has focused on improving TACE treatment evaluation by providing earlier feedback than possible with other modalities. Because gold-standard follow-up imaging does not occur until at least 4 weeks post-treatment, re-treatment for incomplete responses can be more difficult due to tumor growth and decline of the patient's overall health. Immediate evaluation of treatment in the interventional suite could facilitate re-treatment during the same session. Apart from being more convenient for both the patient and radiologist, preventing multiple treatments and additional follow-up CT or MRI will also be more cost effective for the patient. Furthermore, assuming the proposed methods can be incorporated in real-time through the use of parallel computing and GPUs, non-contrast power Doppler ultrasound could also be a valuable addition to real-time monitoring of TACE. Digital subtraction angiography (DSA) is currently used to guide treatment delivery [30]. However, DSA is limited to visualization of the vessel architecture that has been injected with contrast, potentially leaving collateral tumor feeder vessels undetected [88]. Therefore, non-contrast blood flow estimation techniques could provide the necessary complimentary guidance and monitoring of treatment delivery.

In addition to TACE, non-contrast perfusion ultrasound imaging could benefit several other interventional procedures, including radioembolization and ablation. Transarterial radioembolization (TARE) differs from TACE in that it aims to induce tumor necrosis through

delivery of radioactive substances, such as Yittrium-90 (Y90), instead of chemotherapy to the tumor arterial supply [24]. Unlike TACE, TARE does not aim to induce an acute macroembolic effect through arterial occlusion [24]. However, changes in CT perfusion have been shown to indicate treatment response in liver metastases [89]. Similar to TACE treatment evaluation, these changes are not able to be detected earlier than 4-weeks post-treatment due to treatment-induced artifacts in gold-standard CT and MRI [89, 90]. Therefore, non-contrast ultrasound could potentially be similarly adopted for early TARE treatment evaluation to help predict treatment response.

The proposed techniques could also improve guidance of liver ablation therapies. B-mode ultrasound is currently used to guide ablative therapies, including radiofrequency ablation (RFA) [91]. However, because tumors can be difficult to differentiate from background tissue in B-mode, contrast-enhanced ultrasound has been proposed to provide better delineation of the tumor before and after RFA needle placement [91]. As mentioned previously, contrast agents are limited by time and dose in the blood stream, which is not ideal for time sensitive ablation procedures. Therefore, the proposed techniques could facilitate continuous scanning throughout the procedure and potentially improve targeting of treatment delivery.

Lastly, in addition to treatment monitoring and evaluation, the methods presented in this dissertation could also be useful for diagnostic purposes and in organs other than the liver. For example, a new project in the lab is aiming to use these methods for detecting brown adipose tissue (BAT), a highly vascularized type of adipose tissue [92]. Thermal activation of energy conversion in BAT is currently being investigated for treatments of obesity, and contrast-enhanced ultrasound has been considered as a tool for detecting the highly perfused BAT during extreme temperature changes [92]. The ongoing work in the lab is considering non-contrast perfusion imaging to detect these changes, which would allow flexibility in timing of acquisitions in addition to being less invasive.

Functional ultrasound imaging is another example for which the techniques presented

in this dissertation could prove useful. SVD filtering with angled plane wave imaging has been considered for this task [17]. However, adaptive demodulation and ICA have yet to be evaluated for brain perfusion ultrasound imaging. Adaptive demodulation could potentially improve awake studies for which tissue motion is more relevant. Additionally, based on the results in Chapter 6, ICA filtering could potentially greatly improve functional ultrasound sensitivity compared to SVD techniques. Other efforts in the lab are aimed at incorporating these techniques to determine practicality for functional imaging.

BIBLIOGRAPHY

[1] Jørgen Arendt Jensen. *Estimation of blood velocities using ultrasound: a signal processing approach*. Cambridge University Press, 1996.

[2] Martin E Anderson and Gregg E Trahey. A seminar on k-space applied to medical ultrasound. *Department of Biomedical Engineering, Duke University*, 2000.

[3] Graham Brooker. Sensors and signals, chapter 14: Doppler measurement. *Australian Centre for Field Robotics, University of Sydney*, 2006.

[4] Miguel A Quiñones, Catherine M Otto, Marcus Stoddard, Alan Waggoner, and William A Zoghbi. Recommendations for quantification of doppler echocardiography: a report from the doppler quantification task force of the nomenclature and standards committee of the american society of echocardiography. *Journal of the American Society of Echocardiography*, 15(2):167–184, 2002.

[5] Chihiro Kasai, Koroku Namekawa, Akira Koyano, and Ryozo Omoto. Real-time two-dimensional blood flow imaging using an autocorrelation technique. *IEEE Transactions on sonics and ultrasonics*, 32(3):458–464, 1985.

[6] T. Loupas, J. T. Powers, and R. W. Gill. An axial velocity estimator for ultrasound blood flow imaging, based on a full evaluation of the doppler equation by means of a two-dimensional autocorrelation approach. *IEEE Transactions on Ultrasonics, Ferroelectrics, and Frequency Control*, 42:672–688, 1995.

[7] O Bonnefous and Patrick Pesque. Time domain formulation of pulse-doppler ultrasound and blood velocity estimation by cross correlation. *Ultrasonic imaging*, 8(2):73–85, 1986.

[8] Jonathan M Rubin, Ronald O Bude, Paul L Carson, Robert L Bree, and Ronald S Adler. Power doppler us: a potentially useful alternative to mean frequency-based color doppler us. *Radiology*, 190(3):853–856, 1994.

[9] Jonathan M Rubin, Ronald S Adler, J Brian Fowlkes, Steve Spratt, John E Pallister, Jian-Feng Chen, and Paul L Carson. Fractional moving blood volume: estimation with power doppler us. *Radiology*, 197(1):183–190, 1995.

[10] E. Mace, G. Montaldo, B. F. Osmanski, I. Cohen, M. Fink, and M. Tanter. Functional ultrasound imaging of the brain: theory and basic principles. *IEEE transactions on ultrasonics, ferroelectrics, and frequency control*, 60:492–506, 2013.

[11] Ronald S Adler, Jonathan M Rubin, J Brian Fowlkes, Paul L Carson, and John E Pallister. Ultrasonic estimation of tissue perfusion: a stochastic approach. *Ultrasound in medicine & biology*, 21(4):493–500, 1995.

[12] Jian-Feng Chen, J Brian Fowlkes, Paul L Carson, Jonathan M Rubin, and Ronald S Adler. Autocorrelation of integrated power doppler signals and its application. *Ultrasound in medicine & biology*, 22(8):1053–1057, 1996.

[13] S. Bjaerum, H. Torp, and K. Kristoffersen. Clutter filter design for ultrasound color flow imaging. *IEEE Transactions on Ultrasonics, Ferroelectrics, and Frequency Control*, 49:204–216, 2002.

[14] A. Heimdal and H. Torp. Ultrasound doppler measurements of low velocity blood flow: limitations due to clutter signals from vibrating muscles. *IEEE Transactions on Ultrasonics, Ferroelectrics and Frequency Control*, 44:873–881, 1997.

[15] S. Bjaerum, H. Torp, and K. Kristoffersen. Clutter filters adapted to tissue motion in ultrasound color flow imaging. *IEEE Transactions on Ultrasonics, Ferroelectrics, and Frequency Control*, 49:693–704, 2002.

[16] S. Fadnes, S. Bjaerum, H. Torp, and L. Lovstakken. Clutter filtering influence on blood velocity estimation using speckle tracking. *IEEE Transactions on Ultrasonics, Ferroelectrics, and Frequency Control*, 62:2079–2091, 2015.

[17] C. Demene, T. Deffieux, M. Pernot, B. F. Osmanski., V. Biran, S. Franqui, and M. Tanter. Spatiotemporal clutter filtering of ultrafast ultrasound data highly increases doppler and fultrasound sensitivity. *IEEE Transactions on Medical Imaging*, 34:2271–2285, 2015.

[18] APG Hoeks, JJW Van de Vorst, A Dabekaussen, PJ Brands, and RS Reneman. An efficient algorithm to remove low frequency doppler signals in digital doppler systems. *Ultrasonic imaging*, 13(2):135–144, 1991.

[19] L. Thomas and A. Hall. An improved wall filter for flow imaging of low velocity flow. *IEEE Ultrasonics Symposium Proceedings*, 3:1701–1704, 1994.

[20] Anthony P Kadi and Thanasis Loupas. On the performance of regression and step-initialized iir clutter filters for color doppler systems in diagnostic medical ultrasound. *IEEE transactions on ultrasonics, ferroelectrics, and frequency control*, 42(5):927–937, 1995.

[21] Hans Torp. Clutter rejection filters in color flow imaging: A theoretical approach. *ieee transactions on ultrasonics, ferroelectrics, and frequency control*, 44(2):417–424, 1997.

[22] Mai Elfarnawany, Stephen Z Pinter, and James C Lacefield. Improved objective selection of power doppler wall-filter cut-off velocity for accurate vascular quantification. *Ultrasound in medicine & biology*, 38(8):1429–1439, 2012.

[23] Freddie Bray, Jacques Ferlay, Isabelle Soerjomataram, Rebecca L Siegel, Lindsey A Torre, and Ahmedin Jemal. Global cancer statistics 2018: Globocan estimates of

incidence and mortality worldwide for 36 cancers in 185 countries. *CA: a cancer journal for clinicians*, 68(6):394–424, 2018.

[24] L. Lobo, D. Yakoub, O. Picado, C. Ripat, F. Pendola, R. Sharma, R. ElTawil, D. Kwon, S. Venkat, L. Portelance, and R. Yechieli. Unresectable hepatocellular carcinoma: Radioembolization versus chemoembolization: A systematic review and meta-analysis. *Cardiovascular and Interventional Radiology Society of Europe*, 39:1580–1588, 2016.

[25] R. C. Gaba, R. J. Lewandowski, R. H. Hickey, M. O. Baerlocher, E. I. Cohen, S. R. Dariushnia, B. J. d'Othee, S. A. Padia, R. Salem, D. S. Wang, B. Nikolic, and D. B. Brown. Transcatheter therapy for hepatic malignancy: Standardization of terminology and reporting criteria. *Journal of Vascular Interventional Radiology*, 27:457–473, 2016.

[26] J. Lammer, K. Malagari, T. Vogl, F. Pilleul, A. Denys, A. Watkinson, M. Pitton, G. Sergent, T. Pfammatter, S. Terraz, Y. Benhamou, Y. Avajon, T. Gruenberger, M. Pomoni, H. Langenberger, M. Schuchmann, J. Dumortier, C. Mueller, P. Chevallier, and R. Lencioni. Prospective randomized study of doxorubicin-eluting-bead embolization in the treatment of hepatocellular carcinoma: Results of the precision v study. *Cardiovascular and Interventional Radiology Society of Europe*, 33:41–52, 2010.

[27] K. Nam, M. Stanczak, A. Lyshchik, P. Machado, Y. Kono, F. Forsberg, C. M. Shaw, and J. R. Eisenbrey. Evaluation of hepatocellular carcinoma transarterial chemoembolization using quantitative analysis of 2d and 3d real-time contrast enhanced ultrasound. *Biomedical Physics and Engineering Express*, 4:035039, 2018.

[28] Yan Zhao, Rafael Duran, Wei Bai, Sonia Sahu, Wenjun Wang, Sven Kabus, MingDe Lin, Guohong Han, and Jean-François Geschwind. Which criteria applied in multi-

phasic ct can predict early tumor response in patients with hepatocellular carcinoma treated using conventional tace: Recist, mrecist, easl or qeasl? *Cardiovascular and interventional radiology*, 41(3):433–442, 2018.

[29] Nathan Haywood, Kyle Gennaro, John Obert, Paul F Sauer, David T Redden, Jessica Zarzour, J Kevin Smith, David Bolus, Souheil Saddekni, Ahmed Kamel Abdel Aal, et al. Does the degree of hepatocellular carcinoma tumor necrosis following transarterial chemoembolization impact patient survival? *Journal of oncology*, 2016, 2016.

[30] D. B. Brown, B. Nikolic, A. M. Covey, C. W. Nutting, W. E. Saad, R. Salem, C. T. Sofocleous, and D. Y. Sze. Quality improvement guidelines for transhepatic arterial chemoembolization, embolization, and chemotherapeutic infusion for hepatic malignancy. *Journal of Vascular and Interventional Radiology*, 23:287–294, 2012.

[31] Y. Kono, O. Lucidarme, S. Choi, S. C. Rose, T. I. Hassanein, E. Alpert, and R. F. Mattrey. Contrast-enhanced ultrasound as a predictor of treatment efficacy within 2 weeks after transarterial chemoembolization of hepatocellular carcinoma. *Journal of Vascular and Interventional Radiology*, 18:57–65, 2007.

[32] Z. Sparchez, T. Mocan, P. Radu, O. Anton, M. Comsa, T. Vasile, and N. Bolog. Contrast enhanced ultrasonography in assessing the treatment response to transarterial chemoembolization in patients with hepatocellular carcinoma. *Medical Ultrasound*, 18:96–102, 2016.

[33] H. Moschouris, K. Malagari, I. Kornezos, M. G. Papadaki, P. Gkoutzios, and D. Matsaidonis. Unenhanced and contrast-enhanced ultrasonography during hepatic transarterial embolization and chemoembolization with drug-eluting beads. *Cardiovascular Interventional Radiology*, 33:1215–1222, 2010.

[34] K. Kubota, N. Hisa, T. Nishikawa, Y. Fujiwara, Y. Murata, S. Itoh, D. Yoshida, and

S. Yoshida. Evaluation of hepatocellular carcinoma after treatment with transcatheter arterial chemoembolization: comparison of lipiodol-ct, power doppler sonography, and dynamic mri. *Abdominal Imaging*, 26:184–190, 2001.

[35] Cheng-Jeng Tai, Ming-Te Huang, Chih-Hsiung Wu, Chen-Jei Tai, Yeu-Ching Shi, Chun-Chao Chang, Yu-Jia Chang, Li-Jen Kuo, Po-Lei Wei, Ray-Jade Chen, et al. Contrast-enhanced ultrasound and computed tomography assessment of hepatocellular carcinoma after transcatheter arterial chemo-embolization: A systematic review. *Journal of Gastrointestinal & Liver Diseases*, 25(4), 2016.

[36] C. Tremblay-Darveau, R. Williams, L. Milot, M. Bruce, and P. N. Burns. Combined perfusion and doppler imaging using plane-wave nonlinear detection and microbubble contrast agents. *IEEE Transactions on Ultrasonics, Ferroelectrics and Frequency Control*, 61:1988–2000, 2014.

[37] G. J. Tangelder, D. W. Slaaf, A. M. Muijtjens, T. Arts, M. G. oude Egbrink, and R. S. Reneman. Velocity profiles of blood platelets and red blood cells flowing in arterioles of the rabbit mesentery. *Circulation Research*, 59:505–514, 1986.

[38] J. Udesen, F. Gran, K. L. Hansen, J. A. Jensen, C. Thomsen, and M. B Nielsen. High frame-rate blood vector velocity imaging using plane waves: Simulations and preliminary experiments. *IEEE Transactions on Ultrasonics, Ferroelectrics, and Frequency Control*, 55:1729–1743, 2008.

[39] G. Montaldo, M. Tanter, J. Bercoff, N. Benech, and M. Fink. Coherent plane-wave compounding for very high frame rate ultrasonography and transient elastography. *IEEE Transactions on Ultrasonics, Ferroelectrics, and Frequency Control*, 56:489–506, 2009.

[40] Y. L. Li and J. J. Dahl. Coherent flow power doppler (cfpd): Flow detection using

spatial coherence beamforming. *IEEE Transactions on Ultrasonics, Ferroelectrics, and Frequency Control*, 62:1022–1035, 2015.

[41] Y. L. Li, D. Hyun, L. Abou-Elkacem, J. K. Willmann, and J. Dahl. Visualization of small-diameter vessels by reduction of incoherent reverberation with coherent flow power doppler. *IEEE Transactions on Ultrasonics, Ferroelectrics, and Frequency Control*, 63:1878–1889, 2016.

[42] M. A. Lediju, G. E. Trahey, B. C. Byram, and J. J. Dahl. Short-lag spatial coherence of backscattered echoes: Imaging characteristics. *IEEE Transactions on Ultrasonics, Ferroelectrics, and Frequency Control*, 58:1377–1388, 2011.

[43] Léon AF Ledoux, Peter J Brands, and Arnold PG Hoeks. Reduction of the clutter component in doppler ultrasound signals based on singular value decomposition: a simulation study. *Ultrasonic imaging*, 19(1):1–18, 1997.

[44] C. Gallippi and G. Trahey. Adaptive clutter filtering via blind source separation for two-dimensional ultrasonic blood velocity measurement. *Ultrasonic Imaging*, 24:193–214, 2002.

[45] Lasse Lovstakken, Steinar Bjaerum, Kjell Kristoffersen, Rune Haaverstad, and Hans Torp. Real-time adaptive clutter rejection filtering in color flow imaging using power method iterations. *IEEE transactions on ultrasonics, ferroelectrics, and frequency control*, 53(9):1597–1608, 2006.

[46] A. C. H. Yu and L. Lovstakken. Eigen-based clutter filter design for ultrasound color flow imaging: a review. *IEEE transactions on ultrasonics, ferroelectrics, and frequency control*, 57:1096–1111, 2010.

[47] M. Kim, C. K. Abbey, J. Hedhli, L. W. Dobrucki, and M. F. Insana. Expanding acquisition and clutter filter dimensions for improved perfusion sensitivity. *IEEE*

Transactions on Ultrasonics, Ferroelectrics and Frequency Control, 64:1429–1438, 2017.

[48] MinWoo Kim, Yang Zhu, Jamila Hedhli, Lawrence W Dobrucki, and Michael F Insana. Multidimensional clutter filter optimization for ultrasonic perfusion imaging. *IEEE transactions on ultrasonics, ferroelectrics, and frequency control*, 65(11):2020–2029, 2018.

[49] P. Song, A. Manduca, J. D. Trzasko, and S. Chen. Ultrasound small vessel imaging with block-wise adaptive local clutter filtering. *IEEE Transactions on Medical Imaging*, 36:251–262, 2017.

[50] A Heimdal and H Torp. Detecting small blood vessels in color flow imaging: A statistical approach. In *Ultrasonics Symposium, 1997. Proceedings., 1997 IEEE*, volume 2, pages 1219–1222. IEEE, 1997.

[51] Roger J Zemp, Craig K Abbey, and Michael F Insana. Ideal observer model for detection of blood perfusion and flow using ultrasound. In *Biennial International Conference on Information Processing in Medical Imaging*, pages 318–329. Springer, 2003.

[52] MinWoo Kim, Craig K Abbey, and Michael F Insana. Ultrasound perfusion signal processing for tumor detection. In *Medical Imaging 2016: Ultrasonic Imaging and Tomography*, volume 9790, page 97900O. International Society for Optics and Photonics, 2016.

[53] MinWoo Kim, Craig K Abbey, and Michael F Insana. Efficiency of us tissue perfusion estimators. *IEEE transactions on ultrasonics, ferroelectrics, and frequency control*, 63(8):1131–1139, 2016.

[54] J. Tierney, C. Coolbaugh, T. Towse, and B. Byram. Adaptive clutter demodulation for

non-contrast ultrasound perfusion imaging. *IEEE Transactions on Medical Imaging*, 36:1979–1991, 2017.

[55] J. J. Dahl, S. A. McAleavey, G. F. Pinton, M. S. Soo, and G. E. Trahey. Adaptive imaging on a diagnostic ultrasound scanner at quasi real-time rates. *IEEE Transactions on Ultrasonics, Ferroelectrics, and Frequency Control*, 53:1832–1843, 2006.

[56] R. C. Guass, G. E. Trahey, and M. S. Soo. Wavefront estimation in the human breast. In *Medical Imaging 2001. International Society for Optics and Photonics*, pages 172–181, May 2001.

[57] G. F. Pinton, J. J. Dahl, and G. E. Trahey. Rapid tracking of small displacements with ultrasound. *IEEE Transactions on Ultrasonics, Ferroelectrics, and Frequency Control*, 53:1103–1117, 2006.

[58] R. B. Thompson, R. J. Aviles, A. Z. Faranesh, K. Venkatsh, V. Wright, R. S. Balaban, and R. J. Lederman. Measurement of skeletal muscle perfusion during postischemic reactive hyperemia using contrast-enhanced mri with a step-input function. *Magnetic resonance in medicine*, 54:289–298, 2005.

[59] D. Lopez, A. Pollak, C. H. Meyer, R. Jiji, F. H. Epstein, J. R. Hunter, J. M. Christopher, and C. M. Kramer. Asl demonstrates higher and more homogenous calf muscle perfusion with post-occlusion hyperemia than with exercise. *Resonance*, 15:216, 2013.

[60] T. F. Towse, B. T. Childs, S. A. Sabin, E. C. Bush, C. P. Elder, and B. M. Damon. Comparison of muscle bold responses to arterial occlusion at 3 and 7 tesla. *Resonance*, 2015.

[61] T. F. Towse, J. M. Slade, and R. A. Meyer. Effect of physical activity on mri-measured blood oxygen level-dependent transients in skeletal muscle after brief contractions. *Journal of Applied Physiology*, 99:715–722, 2005.

[62] B. H. Friemel, L. N. Bohs, K. R. Nightingale, and G. E. Trahey. Speckle decorrelation due to two-dimensional flow gradients. *IEEE Transactions on Ultrasonics, Ferroelectrics, and Frequency Control*, 45:317–327, 1998.

[63] J. A. Jensen. Field: A program for simulating ultrasound systems. *Med. Biol. Eng. Comput.*, 34:351–353, 1996.

[64] G. Guidi, C. Licciardello, and S. Falteri. Intrinsic spectral broadening (isb) in ultrasound doppler as a combination of transit time and local geometrical broadening. *Ultrasound in Medicine and Biology*, 26:853–862, 2000.

[65] V. Lebon, P. G. Carlier, C. Brillault-Salvat, and A. Leroy-Willig. Simultaneous measurement of perfusion and oxygenation changes using a multiple gradient-echo sequence: application to human muscle study. *Magnetic Resonance Imaging*, 16:721–729, 1998.

[66] E. K. Englund, M. C. Langham, C. Li, Z. B. Rodgers, T. F. Floyd, and E. R. Mohler. Combined measurement of perfusion, venous oxygen saturation, and skeletal muscle t2* during reactive hyperemia in the leg. *Journal of Cardiovascular Magnetic Resonance*, 15:1–13, 2013.

[67] T. F. Towse, J. M. Slade, J. A. Ambrose, M. C. DeLano, and R. A. Meyer. Quantitative analysis of the postcontractile blood-oxygenation-level-dependent (bold) effect in skeletal muscle. *Journal of Applied Physiology*, 111:27–39, 2011.

[68] J. Tierney, K. Walsh, H. Griffith, J. Baker, D. Brown, and B. Byram. Combining slow flow techniques with adaptive demodulation for improved perfusion ultrasound imaging without contrast. *IEEE Transactions on Ultrasonics, Ferroelectrics, and Frequency Control*, 66:834–848, 2019.

[69] J. Baranger, B. Arnal, F. Perren, O. Baud, M. Tanter, and C. Demene. Adaptive

spatiotemporal svd clutter filtering for ultrafast doppler imaging using similarity of spatial singular vectors. *IEEE Transactions on Medical Imaging*, 2018.

[70] Molares. The generalized contrast-to-noise ratio. In *Proceedings of the IEEE International Ultrasonics Symposium*, Kobe, Japan, October 2018.

[71] D. Dumont, J. Dahl, E. Miller, J. Allen, B. Fahey, and G. Trahey. Lower-limb vascular imaging with acoustic radiation force elastography: demonstration of in vivo feasibility. *IEEE transactions on ultrasonics, ferroelectrics, and frequency control*, 56:931–944, 2009.

[72] T. J. Vogl, N. Naguib, A. Nour-Eldin, P. Rao, A. H. Emami, S. Zangos, M. Nabil, and A. Abdelkader. Review on transarterial chemoembolization in hepatocellular carcinoma: palliative, combined, neoadjuvant, briding, and symptomatic indications. *European Journal of Radiology*, 72:505–516, 2009.

[73] W. F. Walker and G. E. Trahey. A fundamental limit on delay estimation using partially correlated speckle signals. *IEEE transactions on ultrasonics, ferroelectrics, and frequency control*, 42:301–308, 1995.

[74] J. Tierney, M. George, C. Coolbaugh, T. Towse, and B. C. Byram. Combining adaptive demodulation with singular value decomposition filtering for improved non-contrast perfusion ultrasound imaging. In *Proc. SPIE 10580, Medical Imaging 2018: Ultrasonic Imaging and Tomography*, Houston, TX, USA, March 2018.

[75] Caterina M Gallippi, Kathryn R Nightingale, and Gregg E Trahey. Bss-based filtering of physiological and arfi-induced tissue and blood motion. *Ultrasound in medicine & biology*, 29(11):1583–1592, 2003.

[76] Sergios Theodoridis and Konstantinos Koutroumbas. Pattern recognition, edition, 2009.

[77] Jaime E Tierney, Don M Wilkes, and Brett C Byram. Independent component analysis-based tissue clutter filtering for plane wave perfusion ultrasound imaging. In *Medical Imaging 2019: Ultrasonic Imaging and Tomography*, volume 10955, page 1095503. International Society for Optics and Photonics, 2019.

[78] Jaime Tierney, Jennifer Baker, Kathryn Ozgun, Anthony Borgmann, Daniel Brown, and Brett Byram. Non-contrast perfusion ultrasound imaging for assessment of transarterial chemoembolization for hepatic malignancy. In *2018 IEEE International Ultrasonics Symposium (IUS)*, pages 1–3. IEEE, 2018.

[79] A. Bell and T.J. Sejnowski. An information-maximization approach to blind separation and blind deconvolution. *Neural Computation*, 7:1129–1159, 1995.

[80] H.B. Nielsen. Ucminf - an algorithm for unconstrained, nonlinear optimization. Technical Report IMM-TEC-0019, IMM, Technical University of Denmark, 2001.

[81] L. K. Hansen, J. Larsen, and T. Kolenda. Blind detection of independent dynamic components. *In proc. IEEE ICASSP'2001*, 5:3197–3200, 2001.

[82] Yiu-ming Cheung and Lei Xu. Independent component ordering in ica time series analysis. *Neurocomputing*, 41(1-4):145–152, 2001.

[83] AJ Hendrikse, RNJ Veldhuis, and LJ Spreeuwers. Component ordering in independent component analysis based on data power. In *Proceedings of the 28th Symposium on Information Theory in the Benelux, Enschede, The Netherlands*, pages 211–218. Eindhoven, 2007.

[84] Edmond HaoCun Wu, LH Philip, and Wai Keung Li. An independent component ordering and selection procedure based on the mse criterion. In *International Conference on Independent Component Analysis and Signal Separation*, pages 286–294. Springer, 2006.

[85] Jørgen Arendt Jensen. Directional transverse oscillation vector flow estimation. *IEEE transactions on ultrasonics, ferroelectrics, and frequency control*, 64(8):1194–1204, 2017.

[86] Rohit Nayak, Viksit Kumar, Jeremy Webb, Adriana Gregory, Mostafa Fatemi, and Azra Alizad. Non-contrast agent based small vessel imaging of human thyroid using motion corrected power doppler imaging. *Scientific reports*, 8(1):15318, 2018.

[87] Charles Tremblay-Darveau, Avinoam Bar-Zion, Ross Williams, Paul S Sheeran, Laurent Milot, Thanasis Loupas, Dan Adam, Matthew Bruce, and Peter N Burns. Improved contrast-enhanced power doppler using a coherence-based estimator. *IEEE transactions on medical imaging*, 36(9):1901–1911, 2017.

[88] Leland Pung, Moiz Ahmad, Kerstin Mueller, Jarrett Rosenberg, Christopher Stave, Gloria L Hwang, Rajesh Shah, and Nishita Kothary. The role of cone-beam ct in transcatheter arterial chemoembolization for hepatocellular carcinoma: a systematic review and meta-analysis. *Journal of Vascular and Interventional Radiology*, 28(3):334–341, 2017.

[89] Caecilia S Reiner, Fabian Morsbach, Bert-Ram Sah, Gilbert Puippe, Niklaus Schaefer, Thomas Pfammatter, and Hatem Alkadhi. Early treatment response evaluation after yttrium-90 radioembolization of liver malignancy with ct perfusion. *Journal of Vascular and Interventional Radiology*, 25(5):747–759, 2014.

[90] Sahar Semaan, Jasnit Makkar, Sara Lewis, Manjil Chatterji, Edward Kim, and Bachir Taouli. Imaging of hepatocellular carcinoma response after 90y radioembolization. *American Journal of Roentgenology*, 209(5):W263–W276, 2017.

[91] Tae Kyoung Kim, Korosh Khalili, and Hyun-Jung Jang. Local ablation therapy with contrast-enhanced ultrasonography for hepatocellular carcinoma: a practical review. *Ultrasonography*, 34(4):235, 2015.

[92] Aidan Flynn, Qian Li, Marcello Panagia, Amr Abdelbaky, Megan MacNabb, Anthony Samir, Aaron M. Cypess, Arthur E. Weyman, Ahmed Tawakol, and Marielle Scherrer-Crosbie. Contrast-enhanced ultrasound: A novel noninvasive, nonionizing method for the detection of brown adipose tissue in humans. *Journal of the American Society of Echocardiography*, 28(10):1247 – 1254, 2015.